Leading to tomorrow

KISToday
Korea Institute of Science and Technology

Technical Reviews

Bio / Medical
Virus-Mimetic Fusogenic Exosomes for Direct Delivery of Integral Membrane Proteins to Target Cell Membranes

Materials / Systems
Intrinsic Photonic Wave Localization in a Three-Dimensional Icosahedral Quasicrystal

Energy / Environment
Metal-Organic Framework Cathodes Based on a Vanadium Hexacyanoferrate Prussian Blue Analogue for High-Performance Aqueous Rechargeable Batteries

SPINTRONICS

Particles and Waves, Skyrmion quasi-particles leading their dynamics & Spin wave bursts for unprecedented low-energy electronic

Cover image

—

Dr. Seong Hoon WOO Center for Spintronics (See "Interview" on P.60)

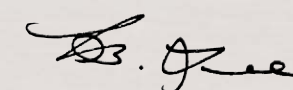# Contents

KIST Korea Institute of Science and Technology

Foreword

In the past, human needs determined the path of progress. Now science itself often dictates progress, improving people's lives in sometimes unexpected ways. The evidence for this can be seen in recent scientific discoveries, such as the detection of a gravity wave which was forecast a hundred years ago by Einstein, the identification of a new planet, Proxima B, the synthesis of a new artificial protein which does not exist in the natural world, and the development of the CRISPR genome editing technique. These discoveries may have been inspired by intellectual curiosity, but their applications have profound implications for everyday living in the future.

KIST is proud to be part of this journey of progress. Recently, our researchers were the first to observe and confirm the unique kinetic dynamic known as "skyrmion breathing", previously simply a theory, so that now we're a step closer to finding more effective ways to operate electronic devices. Other KIST scientists are producing results in the development of new materials and ways to cure dementia. We are also investigating recycling technology for carbon fiber reinforced plastics and platforms for shaping micro-clusters via thermal expansion particles. On the international front, one of our most exciting ongoing projects is supporting Vietnamese government to develop its own science and technology capability with the establishment of a research institute near Hanoi known as VKIST.

The year of 2017 is quickly drawing to a close. It's been a good year for KIST with the new year promising exciting results on many fronts. I'd like to take this opportunity to extend my deepest gratitude to all who follow our efforts and support us along the way. May you have a very happy holiday season!

Dr. Byung Gwon LEE
President of KIST

From this issue of *KISToday* you will find some refinments. Our cover design has changed, and we've adopted an infographics approach designed to help readers better understand the nature and implications of our key research. We're also working to make the magazine's content more interesting while covering key issues of scientific technique, major research results and news of KIST. We hope this new presentation will give you further insights into the dizzying pace of change in fields of science and technology.
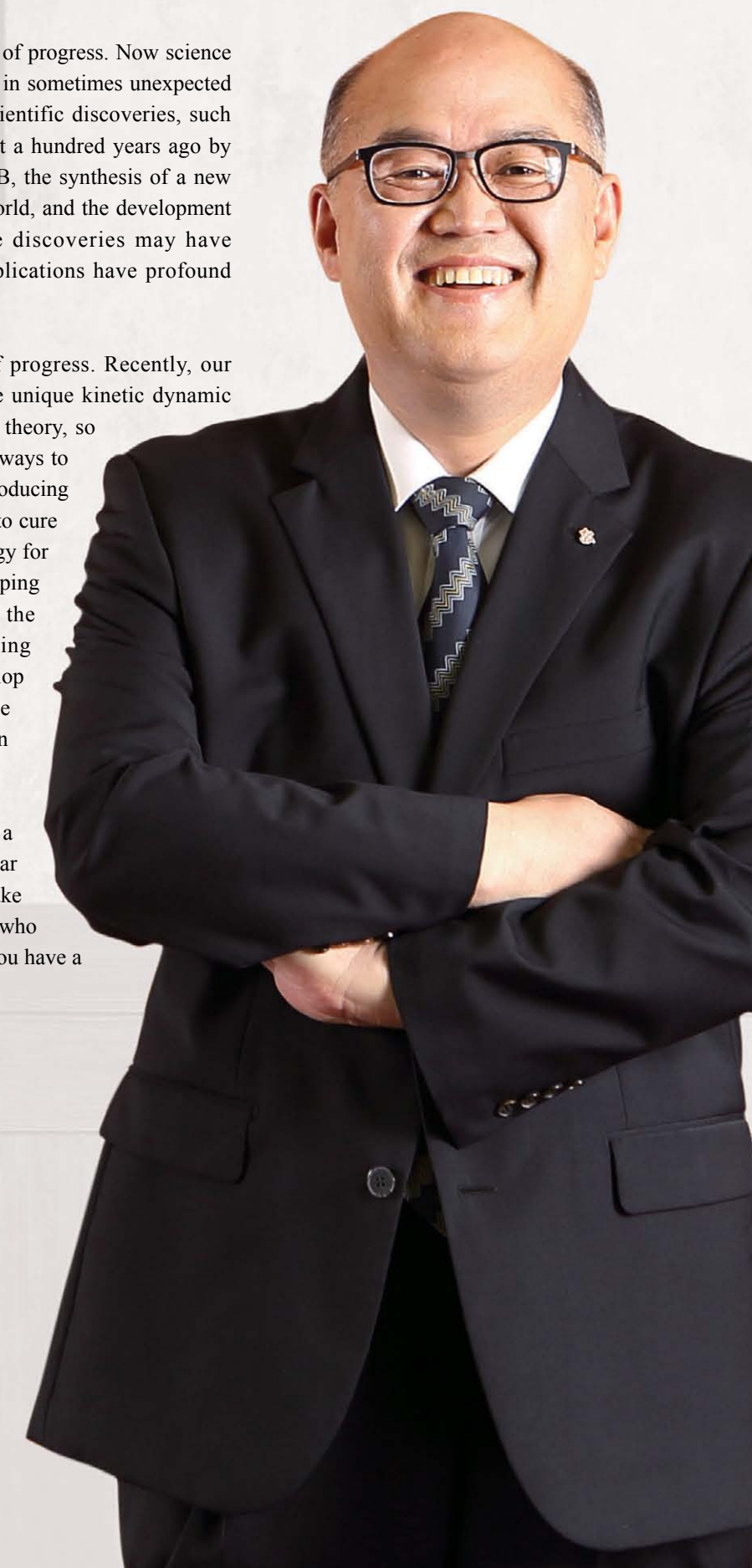
Technical Review

Virus-Mimetic Fusogenic Exosomes for Direct Delivery of Integral Membrane Proteins to Target Cell Membranes

In San KIM

Principal Researcher
Center for Theragnosis
Biomedical Research Institute

iskim14@kist.re.kr

Yoo Soo YANG

Senior Researcher
Center for Theragnosis
Biomedical Research Institute

ysyang@kist.re.kr

Introduction

The focus of this article is on KIST's efforts in investigating an unprecedented exosome-based nano-platform for delivering membrane proteins directly into recipient cell membranes.

A number of major human diseases are related to defects in membrane proteins [1-3]. Despite efforts aimed at delivering membrane proteins to the defective cell membranes [4, 5], workable approaches to treat such defects remain elusive. Here at KIST, we have investigated a new biocompatible nano-platform using an engineered exosome to transfer functional membrane proteins directly into cellular membranes. This modification of plasma membranes is herein called "membrane editing" (Figure 1a). Exosomes are small membrane vesicles, generally thought to be 30 ~ 150 nm in diameter, that are derived from the multivesicular bodies of parental cells [6-8]. Based on their capacity to deliver functional biomolecules (e.g., short interfering RNAs, micro RNAs, mRNAs, and proteins) between cells and their high versatility for engineering, the therapeutic use of naive or surface-engineered exosomes has attracted considerable attention [9-11]. Remarkably, bioactive membrane proteins can be located naturally and expressed on exosomal surfaces due to the cellular originality of exosomes. In addition, membrane protein clusters in microdomains associated with plasma membranes or endosomes are often enriched on exosomes [12].

A bona fide membrane-editing system should be able to fuse with a cell membrane, be easy to engineer, be nonvirulent, and originate from humans. Accumulating evidence from clinical applications points to the bioactivity of exosomes [13, 14], suggesting a real potential for using exosomes to develop a safe, virus-like transfer system for membrane editing. In the work discussed here, we constructed a fusogenic exosome platform capable of fusing with the cell membrane and performing membrane editing. This protein delivery technique could be applied for the transfer of membrane proteins in both medical and research fields.

Results

Preparation and characterization of fusogenic exosomes

The biologically-originating factors promoting fusion, such as viral fusion components on exosome surfaces, are valid biochemical techniques that give rise to high fusion efficiencies. We used VSV-G protein, which is routinely used to enhance the target range and transduction efficiency of retroviruses by providing wider tropism, to improve viral stability and augment resistance to complement inactivation [15]. The VSV-G protein is a low-pH-activated viral fusogen that enables highly effective membrane fusion without adverse effects [16, 17]. Based on a previous report describing pseudo-transduction with VSV-G-coated retroviral particles as a protein delivery method [18], we tested whether expression of VSV-G on the exosomal surface could mediate the delivery of therapeutic membrane proteins.

To test this hypothesis, we designed fusogenic exosomes harboring VSV-G as the fusogen and the tetraspanin CD63 fused with a green fluorescent protein (CD63-GFP) as a reporter for exosomal membrane proteins [19, 20]. A plasmid encoding CD63-GFP and VSV-G was co-transfected into HEK293T cells. After 2 days, the conditioned supernatant was harvested, filtered, serially centrifuged and concentrated by ultracentrifugation [21]. As controls, supernatants were obtained from HEK293T cells subjected to mock transfection or single transfection of the plasmids encoding VSV-G or CD63-GFP. We obtained 180 μg of total protein and 2.5×10^9 particles of exosome from 5×10^9 HEK293T cells. DLS analysis revealed that the diameter of the majority of particles was about 100 nm after ultracentrifugation (Figure 1b) and structurally intact exosomes were detected by TEM analysis (Figure 1d). In addition, flow cytometry and Western blotting confirmed the presence of VSV-G and CD63-GFP on exosomes released by transfected HEK293T cells (Figures 1c-d). Together, we noted that fusogenic exosomes presenting the two proteins on their surfaces were round in shape and had diameters of ~100 nm (Figures 1b-e).

Fusogenic exosome-mediated delivering of CD63-GFP onto recipient cell membranes

To verify that the exosomal membrane proteins were retained in the recipient cell membrane following fusion, we used confocal microscopy to monitor the location of the CD63-
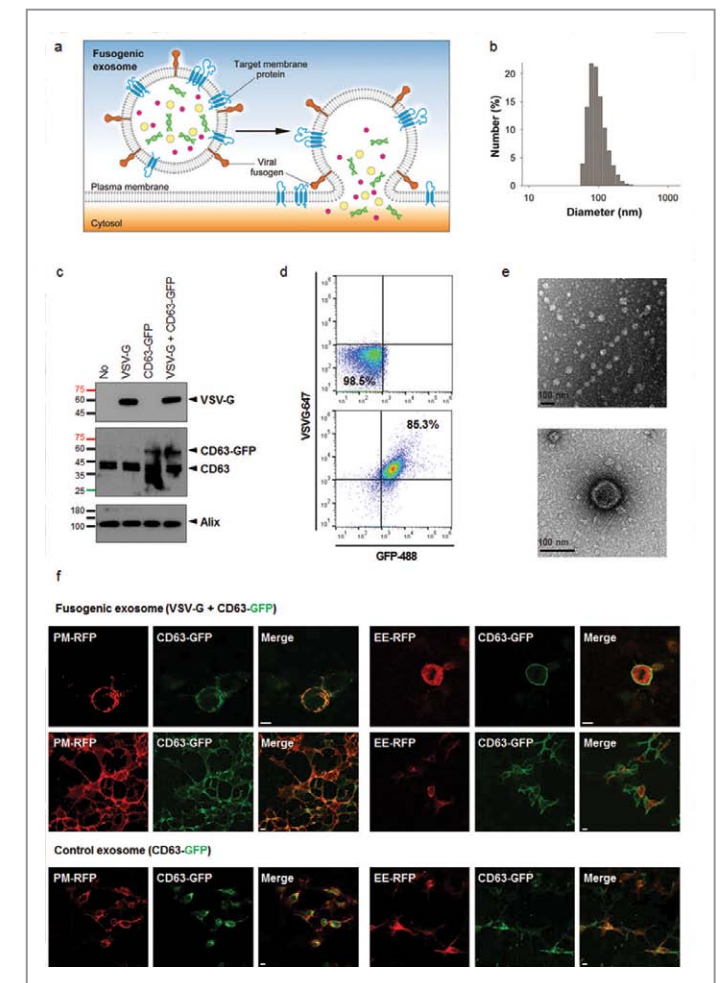

Figure 1   Generation and characterization of fusogenic exosomes. (a) Schematic representation of membrane editing by fusogenic exosomes. (b) Frequency versus size distributions obtained from DLS measurements of purified exosomes. (c) Western blot analysis of VSV-G and CD63-GFP in fusogenic exosomes. (d) Flow cytometric analysis of surface membrane proteins of fusogenic exosomes. (e) Representative TEM image of fusogenic exosomes (scale bar: 100 nm). (f) Confocal images showing the localization of the exosomal marker protein, CD63-GFP, in HEK293T cells. HEK293T cells pre-stained with RFP markers for the plasma membrane (PM-RFP) or early endosomes (EE-RFP) were incubated with exosomes containing CD63-GFP (green) for 2 h at pH 5.5 (scale bars: 10 μm).

GFP in HEK293T cells incubated with fusogenic exosomes for 2 h at acidic (pH 5.5) or neutral (pH 7.4) conditions. Our results showed that HEK293T cells incubated with fusogenic exosomes exhibited colocalization between the CD63-GFP and red-fluorescence (plasma membrane) signals at pH 5.5, whereas those incubated with control (nonfusogenic) exosomes did not (Figure 1f). This suggests that the latter exosomes were internalized into the cells by endocytosis. At neutral pH, both exosomes were co-localized with endosomal marker, indicating that fusogenic exosomes require acidic pH to induce fusion.

VSV-G-triggered membrane fusion at acidic pH

To investigate whether the delivery of membrane proteins could be attributed to the fusogenic activity of VSV-G, we developed an *in vitro* single-molecule imaging assay to monitor the fusion efficiency of single exosome particles with artificial liposomes that mimic the cellular membrane lipid composition. We performed a Förster (fluorescence) resonance energy transfer (more commonly referred to by the acronym FRET) -based fusion assay using a total internal reflection (TIR) fluorescence microscope that can provide an average for the number of fusion events between exosomes and artificial liposomes (Figure 2a) [22]. In the single-vesicle assay, vesicles were paired, one with donor fluorophore (DiI) and another with acceptor fluorophore (DiD). FRET efficiency was measured after each pair of vesicles had been equilibrated and the unpaired vesicles washed away. The data from the paired vesicles were used to distinguish between docked (low FRET) and fully lipid-mixed populations (high FRET). Based on the solid assay, we assessed VSV-G-triggered membrane fusion at acidic pH (Figure 2).

In the experiments described here, liposomes were doped with 1% Ni-NTA lipids to bind His-tagged low-density lipoprotein receptors (LDLRs; extracellular domain), which serve as the major cellular entry port of VSV. Recent studies have shown that VSV-G requires universal cell surface LDLRs and other LDL family members to enable binding of VSV and fusion with target cell membranes [23, 24]. Acceptor (DiD fluorophore-labeled) liposomes were immobilized on the polyethylene glycol (PEG) surface, donor (DiI-labeled) exosomes were added, and the formation of single exosome-liposome complexes triggered lipid mixings at pH 5.5, thereby increasing FRET efficiency. At neutral pH, few exosome-liposome complexes showed lipid mixing after 30 min incubation (Figure 2b, upper panel). At acidic pH, in contrast,
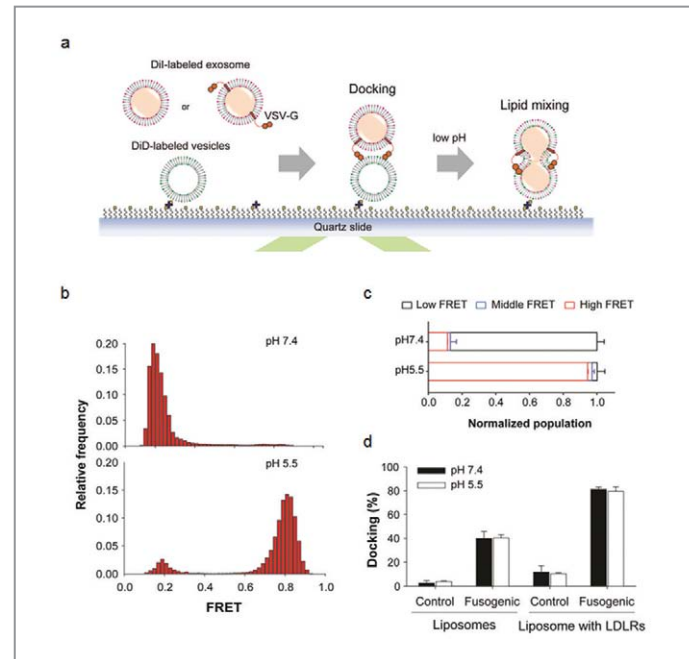
Figure 2 Single-vesicle fusion assay and detection of fusion events. (a) Schematic diagram of the single-vesicle lipid mixing assay. DiD-labeled vesicles were immobilized on the PEG-coated surface and DiI-labeled exosomes were flowed into the flow cell. Extracellular domains of recombinant human LDLR proteins with a C-terminal hexa-histidine tag were tethered onto a Ni-NTA lipid of liposomes (not shown). (b) Normalized distributions of the FRET efficiencies obtained from immobilized LDLR-vesicles and docked fusogenic exosomes, as assessed at pH 7.4 (upper) and pH 5.5 (lower). (c) Lipid-mixing efficiencies quantified based on the percentages of normalized FRET populations using the cut-off FRET efficiencies (E) of E<0.4 for low FRET, 0.4≤E<0.65 for medium FRET, and E≥0.65 for high FRET [32]. The data presented as bars were normalized with respect to the number of the docked vesicles, to account for differences in docking probabilities (Table 1). (d) Bar graph showing the fractions of the docking subpopulations.

the lipid mixing population was markedly accelerated (Figure 2b, lower panel): ~86% of the docked vesicles were lipid-mixed (Figure 2c). Moreover, we observed that LDLR could also stimulate the docking between liposomes and exosomes, which is VSV-G-dependent (Figure 2d and Table 1).

Table 1 Number of docking events and total liposomes for lipid mixing

pH	DiI channel	DiD channel	Docked exosomes	Biotinylated liposomes
7.4	Control exosome	Liposome	6.9	257
	Fusogenic exosome		84	211
5.5	Control exosome		8	202.7
	Fusogenic exosome		96	238.4
7.4	Control exosome	Liposome with LDLR	33	281
	Fusogenic exosome		169	208.4
5.5	Control exosome		28	267
	Fusogenic exosome		180	226.6

Fusogenic exosome-mediated delivery of GLUT4 *in vitro* and *in vivo*

As the exosomal marker protein, CD63, could be transferred into target cell membranes by the fusogenic exosomes, we hypothesized that an exogenous membrane protein overexpressed in producer cells could be similarly incorporated in fusogenic exosomes for delivery. To test this hypothesis, we used the model protein, GLUT4, which is found primarily in muscle and fat tissues and is responsible for the insulin-regulated transport of glucose into cells. We prepared fusogenic exosomes containing GLUT4 from HEK293T cells as described above (Figure 3). GLUT4 has seven transmembrane domains which were expressed on the exosomal membrane, indicating that multi-membrane-spanning proteins can be incorporated into an exosomal surface. We then mixed them with differentiated C2C12 cells and measured the uptake of the fluorescent 2-deoxyglucose analog, 2-[N-(7-nitrobenz-2-oxa-1,3-diaxol-4-yl)amino]-2-deoxyglucose (2-NBDG), as a means to evaluate the function of GLUT4. Our results showed that GLUT4-bearing fusogenic exosomes increased the glucose uptake of C2C12 cells to a level comparable with that seen upon insulin stimulation (Figure 4a). Similar results were obtained in HEK293T cells, where the effect was found to be fusogenic exosome concentration-dependent. Moreover, when HEK293T cells were pretreated with 100 μM of apigenin, which suppresses glucose transporter-1 expression, glucose uptake could be rescued by treatment with GLUT4-bearing fusogenic exosomes (Figure 4b). These results indicate that enhanced glucose uptake of recipient cells was caused by the fusogenic exosome-transferred GLUT4.
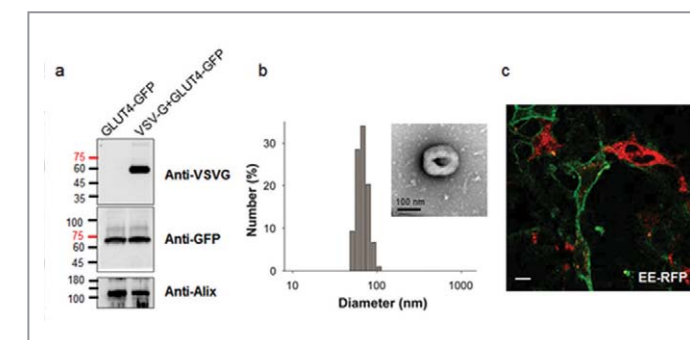
Figure 3 Characterization of fusogenic exosomes harboring GLUT4. (a) Western blot analysis of GLUT4-GFP in fusogenic exosomes using antibodies against VSV-G, GFP, and Alix. (b) Frequency versus size distribution obtained from DLS measurements of GLUT4-exosomes; inset, representative TEM image of fusogenic exosome. (c) Localization of GLUT4-exosome in recipient cells. HEK293T cells pre-stained with RFP early endosome (EE-RFP) were incubated with GLUT4-fusogenic-exosome (green) and analyzed using confocal microscopy (scale bars: 10 μm).
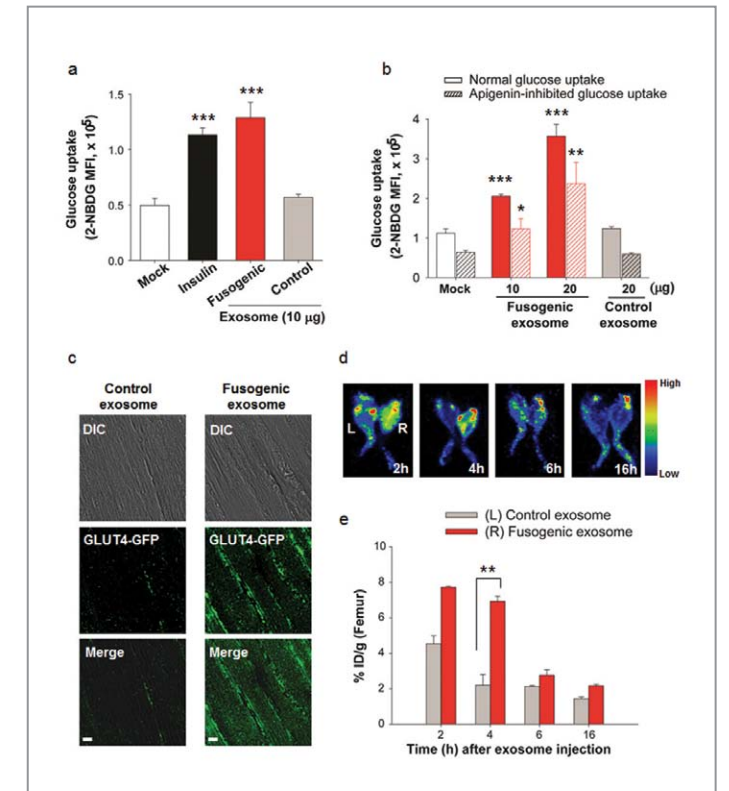
Figure 4 Functional analysis of fusogenic exosome-transferred GLUT4 transporters on the recipient cell membranes. (a) Measurement of glucose uptake in C2C12 cells treated with insulin or exosomes. Glucose uptake was measured with the fluorescent 2-deoxyglucose analog, 2-NBDG, and mean fluorescent intensity (MFI) was determined by flow cytometry. (b) Basal and apigenin-inhibited 2-NBDG uptake by HEK293T cells treated with fusogenic or control exosomes. (c) Representative confocal GLUT4-GFP immunofluorescence images of mouse skeletal TA muscle fibers at 4 h after exosome treatment. Nonpermeabilized TA fibers were isolated from control exosome-treated mice (left) and fusogenic exosome-treated mice (right), and stained with anti-GFP (green) antibody (scale bar: 10 μm). (d) Representative images of glucose uptake PET scans obtained from the femur muscles of BALB/c nude mice of each group (left, control exosomes; right, fusogenic exosomes). The color bar on the right shows the glucose uptake rate, with red and yellow colors defining the areas of highest uptake. (e) Accumulation of [18F]-FDG in skeletal femur regions. At each indicated time point, mice were sacrificed, and the percentage of the injected radioactive dose/gram (% ID/g) was determined in femur tissues. The data represent the mean ± S.D. of three different experiments (*p<0.05, **p<0.01, and ***p<0.005 versus mock, as assessed by Student's t-test).

To test whether fusogenic exosome-transferred GLUT4 could exhibit correct membrane localization , we used confocal immunofluorescence microscopy to analyze tibialis anterior (TA) muscle fibers isolated from mice following intramuscular injection of fusogenic exosomes harboring GLUT4-GFP for 4 h. Control exosome-treated muscle fibers exhibited rather weak GFP signals (Figure 4c, left), suggesting that only a small amount of GLUT4-GFP was localized at the cell surface in the absence of the fusogen. In contrast, fusogenic exosome-treated fibers showed strong GFP signals on the surface membranes of TA muscle (Figure 4c, right).

To further characterize the functionality of fusogenic exosome-transferred GLUT4 *in vivo*, we used positron emission tomography (PET) scanning and *ex vivo* gamma counting to measure [^{18}F] 2-fluoro-2deoxy-D-glucose (^{18}F-FDG) uptake in mouse femur muscles following intramuscular injection with GLUTT4-fusogenic exosomes (right femur) or control exosomes (left femur). Our results revealed that the local uptake indexes of ^{18}F-FDG in the right femur muscle were remarkably higher than those of the left femur muscle (Figure 4d). In the fusogenic-exosome-treated group, the delivered GLUT4 proteins remained on the muscle cell membranes for up to 4 h post-injection and were responsible for the transport of ^{18}F-FDG (Figures 4d and 4e). Our results demonstrate that fusogenic exosomes could facilitate *in vivo* glucose uptake by rendering GLUT4 proteins.

Conclusions

The results of our study demonstrate the rapid and efficient delivery of membrane proteins into plasma membranes using a novel exosome-based nano-platform. These fusogenic exosomes can fuse with and modify plasma membranes in a process of membrane editing. This can facilitate the transfer of exogenous proteins into target cell membranes leaving their form intact.

The ability of naturally engineered exosomes to express therapeutic proteins, exhibit a high degree of specificity, mediate cell-to-cell communications, and evade immune detection illustrates their potential value for future applications in membrane-protein therapy applications. Nevertheless, whether fusogenic exosomes represent a universally applicable membrane-editing platform remains hypothetical. Despite accumulating evidence pointing to the bioactivity of fusogenic exosomes in clinical situations, exosome-based platforms must be shown to demonstrate low immunogenicity and simple drug loading and cost-effective production. In addition, the determination of heterogeneity and molecular composition of exosomes within a physiologically relevant context is a continuing challenge. In the future, the development of targeting moieties that enable exosomes to target specific tissues following systemic administration, along with efforts to improve exosome production yield and efficiency, should improve the utility of this emerging strategy for delivering membrane proteins.

Note

References

[1] Sanders CR, Myers JK. *Annu. Rev. Biophys. Biomol. Struct.* 2004; 33: 25-51.

[2] Cobbold C et al. *Trends Cell Biol.* 2003; 13 (12): 639-47.

[3] Ng DP, Poulsen BE, Deber CM. *Biochimica et Biophysica Acta (BBA) - Biomembranes* 2012; 1818 (4): 1115-1122.

[4] de Planque MR et al. *IEE Proc. Nanobiotechnol.* 2006; 153 (2): 21-30.

[5] Pisal DS, Kosloski MP, Balu-Iyer SV. *J. Pharm. Sci.* 2010; 99 (6): 2557-75.

[6] Thery C, Zitvogel L, Amigorena S. *Nat. Rev. Immunol.* 2002; 2 (8): 569-579.

[7] Yanez-Mo M et al. *J. Extracell. Vesicles* 2015; 4: 27066.

[8] Cho YW et al. *Journal of Controlled Release* 2014; 175: 43-47.

[9] EL Andaloussi S et al. *Nat. Rev. Drug Discov.* 2013; 12 (5): 347-57.

[10] Ferguson SW, Nguyen J. *Journal of Controlled Release* 2016; 228: 179-190.

[11] Vader P et al. *Adv. Drug Deliv. Rev.* 2016; 106 (Pt A): 148-156.

[12] Raposo G, Stoorvogel W. *J. Cell Biol.* 2013; 200 (4): 373-83.

[13] Viaud S et al. *Cancer Res.* 2010; 70 (4): 1281-5.

[14] Alvarez-Erviti L et al. *Nat. Biotechnol.* 2011; 29 (4): 341-5.

[15] Cronin J, Zhang XY, Reiser J. *Curr. Gene Ther.* 2005; 5 (4): 387-98.

[16] Roberts PC, Kipperman T, Compans RW. *J. Virol.* 1999; 73 (12): 10447-57.

[17] Temchura VV et al. *Vaccine* 2008; 26 (29-30): 3662-72.

[18] Kaczmarczyk SJ et al. *Proc. Natl. Acad. Sci. USA.* 2011; 108 (41): 16998-17003.

[19] Hoffman RM. *Breast Cancer Res.* 2013; 15 (3): 310.

[20] Suetsugu A et al. *Adv. Drug Deliv. Rev.* 2013; 65 (3): 383-90.

[21] Thery C et al. *Curr. Protoc. Cell Biol.* 2006; Unit 3: 22.

[22] Diao J et al. *Nat. Protoc.* 2012; 7 (5): 921-34.

[23] Finkelshtein D et al. *Proc. Natl. Acad. Sci. USA.* 2013; 110 (18): 7306-11.

[24] Amirache F et al. *Blood* 2014; 123 (9): 1422-4.

Feature Articles

Microparticle-Based RT-qPCR for Highly Selective Rare Mutation Detection

Sang Kyung KIM

Principal Researcher
Center for Biomicrosystems
Brain Science Institutue

sangk@kist.re.kr

Introduction

During the last decade, there has been a remarkable growth in understanding the role of nucleic acids. This has led to an increased focus on quantitative and qualitative analyses of nucleic acids across a wide range of disciplines. As a result, the technique of multiplex qPCR has been consistently pursued as a means to cover the rapidly increasing number of genetic targets of interest in a single phenotype. We illustrated in a previous report that a particle-based qPCR is capable of extensively multiplexed analysis of many different genetic targets within a sample [3].

Individual qPCR occurs in a microparticle of a primer-immobilized network (PIN). To apply PIN qPCR to RNA targets, the RNA needs to be reversely transcribed to complementary DNAs (cDNA). qRT-PCR, reverse transcription and real-time PCR, allow fast and sensitive quantification of target RNAs in many clinical laboratories [1, 2]. However, it has been challenging to specifically detect rare mutants in the midst of normal genes. Thus, various approaches to enhance the selectivity of qRT-PCR have been reported. Most researchers have focused mainly on the molecular design of primers and probes to improve selectivity [9].

Our work presents a new qRT-PCR method using PIN applied for the detection of a rare mutation of Bcr-Abl fusion. PIN particles are made of polyethylene glycol-based hydrogel and specific primers. We designed a new version of PIN particle to capture, reverse transcribe and amplify a target RNA within the PIN particle. The target Bcr-Abl mRNA was selectively detected without the aid of specific probes from the total RNA of the cell mixture where 10,000:1 mutant cells were present.

RT-qPCR in a primer-immobilized network

We quantitated rare Bcr-Abl fusion transcripts among normal genes and confirmed the sequence easily. As shown in Figure 1(A), the process is as follows. i) We immobilized the
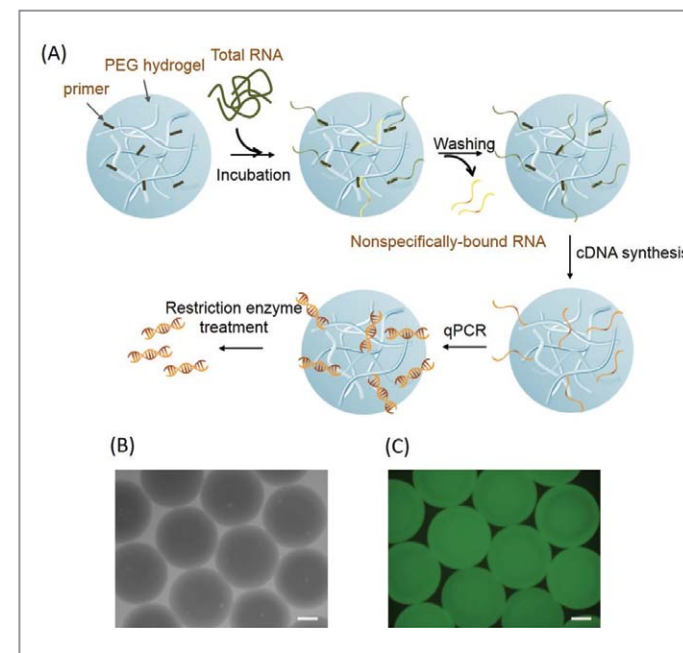

Figure 1 Principle of RT-qPCR in a primer-immobilized network (PIN) microparticle. (A) Reverse transfection was conducted in a reverse primer-immobilized PEG hydrogel microparticle. After cDNA synthesis, the surrounding solution was changed to PCR solution containing forward primer, then the PIN particle was subjected to qPCR. The amplified gene was purified by restriction enzyme digestion. (B) Optical and (C) fluorescence images of PIN particles (scale bar: 200 μm).

reverse primers for reverse transcription (RT) to PIN particles. ii) The target RNAs selectively bound to the RT primers along with non-specific adsorption of total RNA to the PIN particles. iii) The non-specifically-bound RNA was rinsed off with agitated buffer. iv) The target RNA was reverse transcribed to the cDNA template fixed in the PIN particles. v) After qPCR was conducted for quantification, the amplicons were released from the PIN particles through cutting with restriction enzyme.

For the selective PCR of Bcr-Abl fusion, a forward primer in the Bcr region and a reverse primer in the Abl region were selected. The reverse primer was utilized as the RT primer and immobilized in the PIN particles. A pre-polymer mixture with acrydite-functionalized RT primers was jetted into sessile drops and cured with UV irradiation. The uniformity in size and fluorescence of the resulting hemispheric PIN particles is illustrated in Figures 1(B) and 1(C).

When the total RNA was added to the PIN particles, the immobilized RT primers hybridized to the designated region of Abl. Since the reverse primer was annealed to the Abl part, both Bcr-Abl mRNA and normal Abl mRNA were captured on the particle and then reverse transcribed to cDNA. After RT, the PIN particles were injected into a qPCR chamber with a SYBR Green-based master mix and forward primers. Owing to the
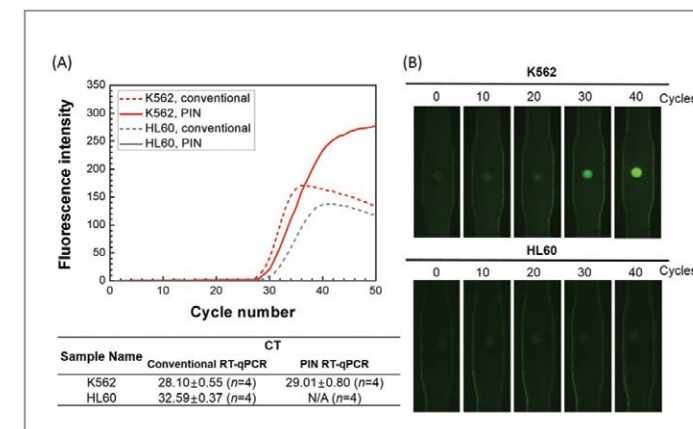
Figure 2 Comparison of the conventional RT-qPCR and PIN RT-qPCR. The Ct values of positive sample (K562) were 28.10±0.55 (n=4) and 29.01±0.80 (n=4), respectively. The Ct value in the PIN particle deteriorated slightly (less than 1) compared to the conventional RT-qPCR. A signal from the non-specific amplicons was not detected in PIN RT-qPCR while a non-specific signal was shown in the conventional RT-qPCR (Ct value: 32.59±0.37 (n=4)). (B) The fluorescence image of a PIN particle with PCR cycle progression.

confinement from the forward primers, only the Bcr-Abl gene could be amplified in the PIN particle during the qPCR process. If necessary, the amplicons could be released from the PIN particle by the restriction enzyme reaction for further analysis. As many other studies have demonstrated, the K562 cell line was adopted as Bcr-Abl (+) cells, and HL60 cells were used as Bcr-Abl (-) cells.

PIN RT-qPCR for the detection of Bcr-Abl

Total RNA was extracted from K562 and HL60 cells, and the quality of the extracted RNA was validated through agarose gel electrophoresis. The PIN particles were incubated with total RNA samples to capture target RNAs at 65°C for 5 min and the particles were rinsed with clean buffer solution to sweep off the non-specifically-bound RNA. Then, the particles went through the RT and qPCR in sequence. The quantitative performance of PIN RT-qPCR was investigated through comparison with that of conventional RT-qPCR. Thus, the conventional RT-qPCR was conducted in parallel with PIN RT-qPCR under the same protocols and primers. Figures 2(A) and 2(B) show real-time PCR results for the two methods for the target gene and negative control. For the target-positive sample, the threshold cycle (Ct) of the conventional RT-qPCR and PIN RT-qPCR were 28.10±0.55 (mean ± SD) and 29.01±0.80, respectively, exhibiting a variance of less than 1. The PIN RT-qPCR showed a distinct difference for the negative sample, where no fluorescence increases were detected until the 50th cycle. In contrast, the conventional RT-qPCR showed

Bio / Medical

Materials / Systems

Energy / Environment

Research Highlights

KIST News

VKIST

Up Close

Interview

a fluorescence increase around 32 cycles, which is ascribed to various non-specific amplifications. The amount of RT primer in the PIN particles was tested as a candidate cause of the divergent results. However, the superior selectivity of the PIN RT-qPCR was conserved regardless of the RT primer's concentration in the range of 5 to 50 μM (data not shown). The 20 μM of RT primer used in the pre-polymer mixture was retained for the PIN particle production in the following experiments.

Selective capture of Bcr-Abl transcript

In regard to the selective amplification of the target RNA in the PIN RT-qPCR, the major advantage of the PIN RT-qPCR is believed to be the selective reservation of target genes before the RT step. We verified this assumption by controlling the agitation with TE buffer containing 0.15% Tween-20 after the incubation of PIN particles with total RNA solution. When the PIN particles went through RT directly from the total RNA mixture, the ensuing qPCR result became fairly non-specific. The Ct value of the target positive sample was 27.66±1.04, and the signal of a negative sample also increased around 32 cycles. As Figure 3(A) shows, the use of the agitation with buffer dramatically reduced the non-specific signal from negative samples while stably sustaining the target-specific signal. The simple washing step seemed very effective in sweeping out the non-specific RNAs from the PIN particles and selectively reserving the target RNA. Figure 3(B) shows the fluorescence images of each PIN particle after the qPCR was completed. One of the common problems in qPCR with SYBR Green is the background fluorescence induced from primer-dimer formation. We examined the background signals from a no-template control (NTC) in both conventional and PIN qPCR systems using the primers of the Bcr-Abl fusion gene. The fluorescence sharply increased in the conventional qPCR at around 32 cycles. However, the PIN qPCR was not accompanied by background fluorescence in the NTC. It is considered that primer-dimer formation was reduced by virtue of the immobilized primer, which lowered the chance of the random binding of primers during the annealing process[4, 5] The disadvantage of the SYBR Green-based assay was circumvented with PIN qPCR.

Thus, we tested whether the PIN particle-based qPCR itself accomplished the selective amplification of cDNA templates from the target RNA. The cDNA was synthesized using RT primer according to the conventional RT method. Then, the cDNA was amplified with conventional qPCR and PIN qPCR side by side. In these comparative experiments, the background fluorescence increased in both assays for

negative control samples; overall, PIN qPCR did not have a noticeable advantage over the conventional method (data not shown). In the specific case of Bcr-Abl, a fair amount of false cDNA templates stemmed from partial hybridization in the RT step, which led to irrelevant amplification in the qPCR step. Therefore, the removal of nonspecific RNAs before RT is essential for the selectivity of PIN RT-qPCR. We also tested functional advantage of PIN as a qPCR reactor. Although some researchers reported bead-based RNA capture and amplification, the beads only worked for preparation of the target gene not for the qPCR e reactor [7, 8]. In that research, the qPCR was separately conducted using both forward and reverse primers which could generate primer-dimer formation. When we conducted qPCR using PIN-carrying cDNA with both primers, inevitably, the primer-dimer form was detected in gel analysis. Because the reverse primer-immobilized particle works both as capture substrate and qPCR reactor, highly selective target detection is possible.
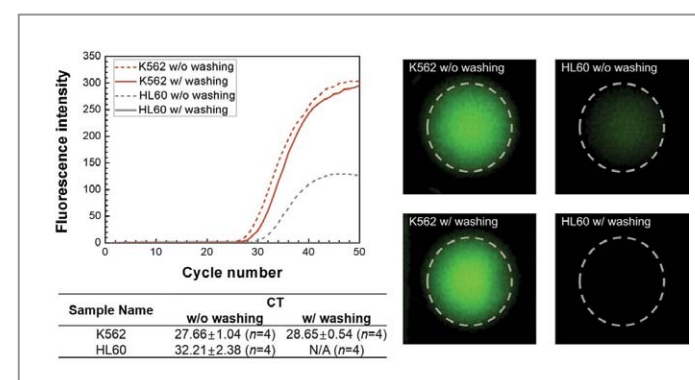
Figure 3 Effect of washing step after the incubation of PIN particles with total RNA. (A) In the case of unwashed PIN particles, the Ct values of positive and negative controls were 27.66±1.04 (n=4) and 32.21±2.38 (n=4), respectively. This result shows that there is non-specific amplification. However, the addition of a washing step after incubation, non-specific amplicons were not detected in the qPCR result. The Ct value of the positive sample was 28.65±0.54 (n=4). (B) Fluorescence image of each PIN particle after qPCR.

The sensitivity of the present platform could be investigated with a cell mixture of CML cell lines. We mixed increasing numbers of K562 cells (10^2 to 10^6 cells) with a fixed number of HL60 cells (1×10^6 cells) and extracted the total RNA from each cell mixture. The total RNAs were used in the PIN RT-qPCR system. Four different PINs were tested at each concentration. As a result, the amplification curve gradually decreased as the number of K562 cells increased, as seen in Figure 4(A), showing a linear correlation between the Ct value and the number of cells on a log scale, as illustrated in Figures

4(B) and 4(C). When the total RNA extracted from 10 K562 cells was used in the PIN RT-qPCR, the fluorescence did not increase. Thus, the detection limit was 10^2 K562 cell/1×10^6 HL60 cells in this system.
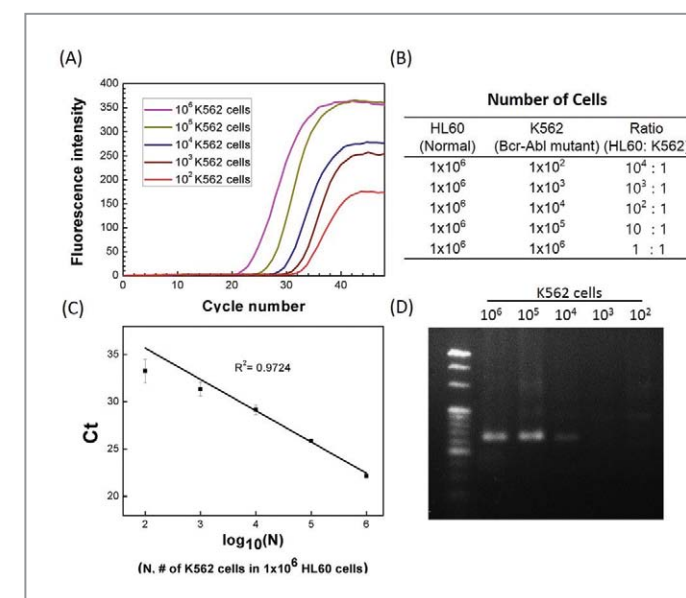
Figure 4 Sensitivity test of PIN RT-qPCR. A serially increasing number of K562 cells (from 10^2 to 10^6 cells) were mixed with 106 HL60 cells. The total RNA was extracted from each cell mixture and subjected to the PIN RT-qPCR. (A) qPCR graphs of each sample. (B) Ct values (n=4). (C) Log linearity according to the number of K562 cells. (D) Detection of the purified target amplicons on agarose gel.

Conclusion and outlook

We first developed a microparticle-based RT-qPCR system for mRNA quantification using PIN particles and demonstrated its superior selectivity for the Bcr-Abl fusion transcript. The Bcr-Abl mRNA was selectively detected from the total RNA of cell mixtures where 10,000:1 mutant cells were present. As demonstrated in the Bcr-Abl detection, PIN RT-qPCR for diagnosis has multiple merits over conventional methods. First, PIN particles play the role of substrate for target capture and purification through a simple work flow. Thus, this system reduces the mismatched reverse transcription of irrelevant RNAs, improving the specificity of the assay. Second, the PIN particles with cDNA templates become the reactors for the qPCR and complete the concise workflow. This reduces the probability of sample contamination, which often occurs between separated experimental steps. Third, amplicons and fluorescent signals accumulate in the volume of PIN particles, leading to a high signal to noise ratio. This

makes the assay more sensitive and reliable from the viewpoint of data acquisition and interpretation. Finally, the PIN particle becomes a reservoir of amplicons after the PCR. The amplified target genes can be stored or collected at high purity for further analysis.

These advantages of PIN RT-qPCR are distinct in the field of diagnosis requiring accuracy from complicated patient samples. Furthermore, PIN RT-qPCR is a versatile platform and can be synergistically combined with molecular probes of high selectivity. It would be even more powerful for the diagnosis of rare mutants from various clinical specimens.

Note

References

[1] Bernard PS, Wittwer CT. *Clinical Chemistry* 2002; 48 (8): 1178-1185.

[2] Bustin SA, Mueller R. *Clinical Science* 2005; 109: 365-379.

[3] Jung S, Kim J, Lee DJ, Oh EH, Lim H, Kim KP, Choi N, Kim TS, Kim SK. *Scientific Reports* 2016; 6: 22975.

[4] Khan Z, Poetter K, Park DJ. *Analytical Biochemistry* 2008; 375 (2): 391-393.

[5] Palanisamy R, Connolly AR, Trau M. *Bioconjugate Chemistry* 2010; 21 (4): 690-695.

[6] Postollec F, Falentin H, Pavan S, Combrisson J, Sohier D. *Food Microbiology* 2011; 28 (5): 848-861.

[7] Sun H, Olsen T, Zhu J, Tao J, Ponnaiya B, Amundson SA, Brenner DJ, Lin Q. *RSC Advances* 2015; 5 (7): 4886-4893.

[8] Taniguchi K, Kajiyama T, Kambara H. *Nature Methods* 2009; 6 (7): 503.
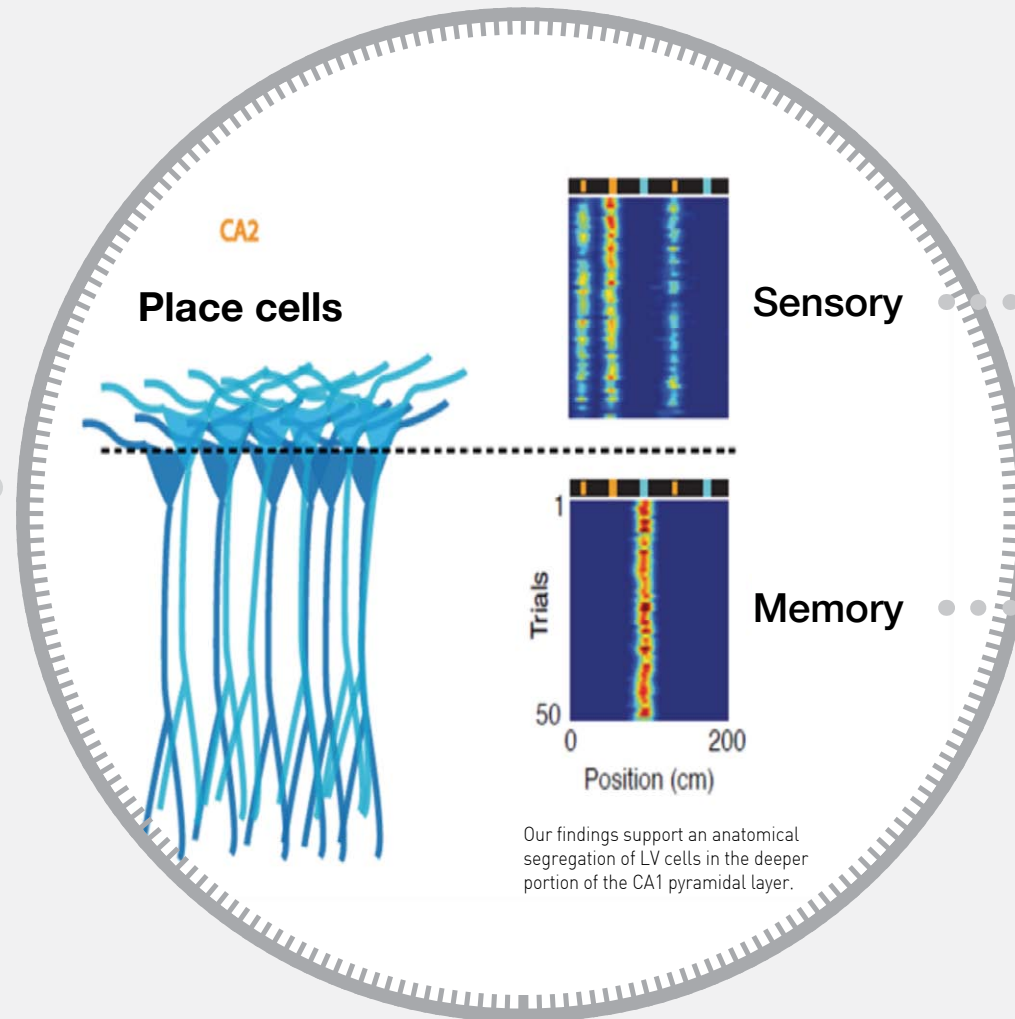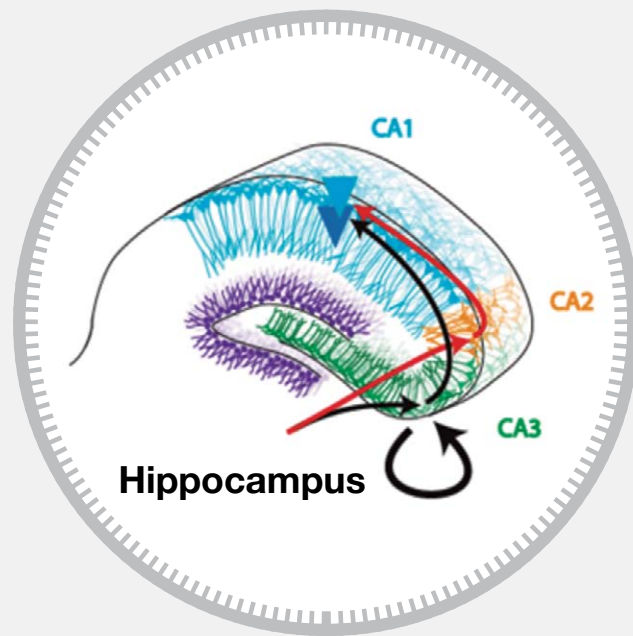
[9] Wong ML, Medrano JF. *Biotechniques* 2005; 39 (1): 75.

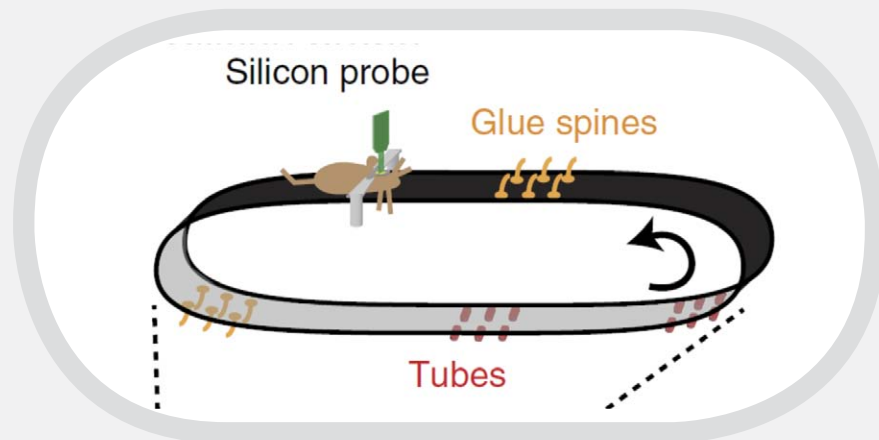# Place cells are more strongly tied to landmarks in deep than in superficial CA1
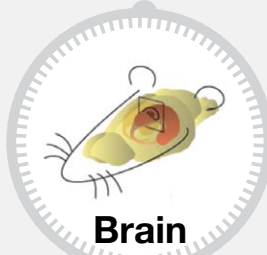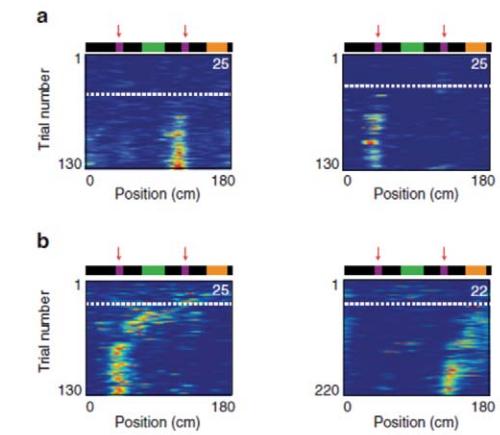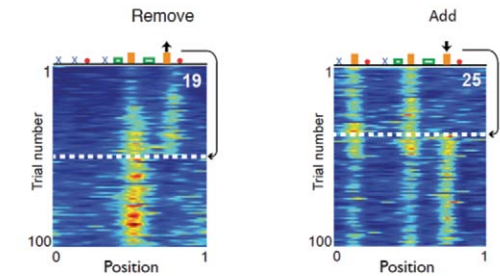
Sebastien ROYER

Principal Researcher
Center for Functional Connectomics
Brain Science Institute

royers@kist.re.kr

Brain

Hippocampus

CA1
CA2
CA3

Place cells

CA2

Sensory

Memory

Trials

Position (cm)

Our findings support an anatomical segregation of LV cells in the deeper portion of the CA1 pyramidal layer.

Evidence

Remove   Add

Instant dynamics of LV cells.
(a) The fields disappeared instantly when the landmark was removed.
(b) When an extra spine landmark was added to the belt, new fields were created instantly.

a

b

CM field dynamics following landmark manipulations.
The addition of landmarks triggered field reconfiguration in a large number of cells.
(a) Example of 'switching' and (b) 'drifting' cells in CA1.

Tread Mill

Silicon probe
Glue spines
Tubes

Abstract

Environmental cues affect place cells responses, but whether this information is integrated versus segregated in distinct hippocampal cell populations is unclear. Here, we show that, in mice running on a treadmill enriched with visual-tactile landmarks, place cells are more strongly controlled by landmark-associated sensory inputs in deeper regions of CA1 pyramidal layer (CA1d). Many cells in CA1d display several firing fields correlated with landmarks, mapping positions slightly before or within the landmarks. Supporting direct involvement of sensory inputs, their firing fields show instantaneous responses to landmark manipulations, persist through change of context, and encode landmark identity and saliency. In contrast, cells located superficially in the pyramidal layer have single firing fields, are context specific and respond with slow dynamics to landmark manipulations. These findings suggest parallel and anatomically segregated circuits within CA1 pyramidal layer, with variable ties to landmarks, allowing flexible representation of spatial and non-spatial information.

Technical Review

Intrinsic Photonic Wave Localization in a Three-Dimensional Icosahedral Quasicrystal

Ka Hyun HUR

Senior Researcher
Center for Computational Science
Materials and Life Science Research
Division

khur@kist.re.kr

Introduction

The first discovery of a quasicrystal disproved the longstanding conjecture in condensed matter physics that only crystalline materials with translational symmetry could be densely packed and highly ordered [1]. The quasicrystal structures exhibit long-range order but lack translational symmetry. One of the most interesting scientific topics about quasicrystals is wave transport because the translational symmetry of materials strongly governs the transport properties of every form of wave. It is known that in crystalline materials the waves with wavelengths commensurate with the crystal's periodicity travel without scattering loss. Meanwhile, because of frequent scattering, in disordered materials waves transmit via random walks leading to diffusive transmission (note that diffusive transmission is the origin of Ohm's law) [2]. In light of the wave nature of electrons, Anderson predicted that sufficiently large structural randomness will lead to complete halting of electrons, the so-called Anderson localization [3], and the electron conductivity will decrease exponentially with increasing sample thickness [4]. Owing to the mixed structural characteristics, a critical question has been raised about wave transport in quasicrystals, including localization [5].

Results and discussion

Quasicrystal structure building

The first step is the preparation of a 3D quasicrystal structure. We chose an icosahedral quasicrystal structure for the present study. The icosahedral quasicrystal structure can be built following the substitution rules shown in Figures 1a-i [6]. The rhombic triacontahedron (purple in Figure 1a) constitutes a large proportion of an icosahedral quasicrystal. The rhombic triacontahedron structure can be derived from the intersection of five cubes (Figure 2a) [7].
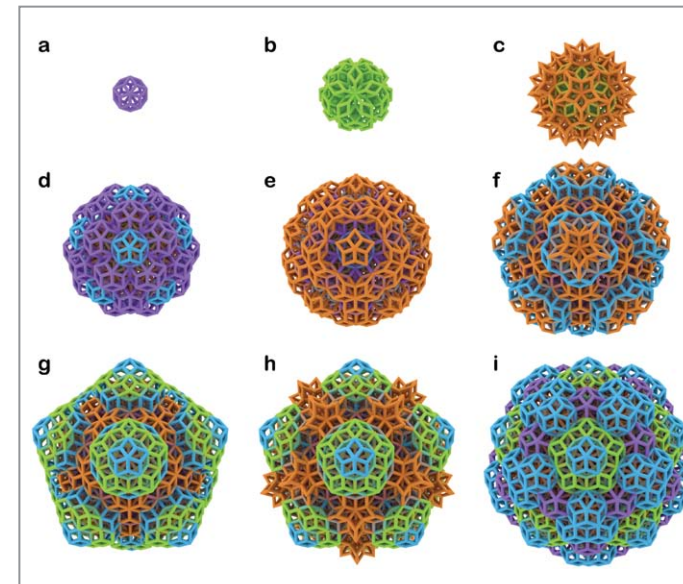

Figure 1   Schematic of the construction of 3D icosahedral quasicrystals. (a-i) Substitution rules for constructing a 3D icosahedral quasicrystal [6]: (a) A triacontahedron represented in purple is located at the center of the icosahedral quasicrystal. (b) Thirty rhombic dodecahedra represented in green are placed on the 2-fold axes. (c) Twenty rhombohedra represented in orange are placed on the 3-fold axes, and twelve clusters of ten rhombohedra are placed on the 5-fold axes. (d) Thirty triacontahedra are placed on the 2-fold axes, and twelve rhombic icosahedra represented in blue are placed on the 5-fold axes. (e) Twenty clusters of ten rhombohedra on the 3-fold axes. (f) Twelve clusters of five rhombic icosahedra on the 5-fold axes are capped by twelve clusters of ten rhombohedra. (g) Twelve clusters of five rhombic dodecahedra are placed on the 5-fold axes, and twelve rhombic icosahedra are placed in the middle of each edge of the inflated cell. (h) Twenty clusters of ten rhombohedra are placed on the 3-fold axes. (i) Finally, twenty clusters of three rhombic icosahedra are placed on the 3-fold axes, and thirty triacontahedra are placed on the 2-fold axes.

Therefore, the parallelogram shape planes of the rhombic triacontahedrons locate on the three faces of the five cubes. We predict that the planes derived from the parallelograms form effective Brillouin zone faces giving rise to Bragg scattering.

Rotation-dependent photonic wave transmission spectra

We obtained transmission spectra of the icosahedral quasicrystal using a finite-difference time-domain (FDTD) code [8]. A diamond structure was further compared as a reference. As shown in Figure 3e, the photonic bandgap of the diamond on the first Brillouin zone boundary matches nicely with the low-intensity spectral regime. Therefore, the low-transmission regime can be interpreted as footprints of the photonic bandgap [9]. A similar low-transmission regime is observed in the quasicrystal. The result also exhibits good agreement with the Bragg scattering from the effective Brillouin zone faces with a plane distance of *0.85d*, where d is the rod length of the rhombic triacontahedron (Figure 2b). In the present work, *d* is set to *1* cm
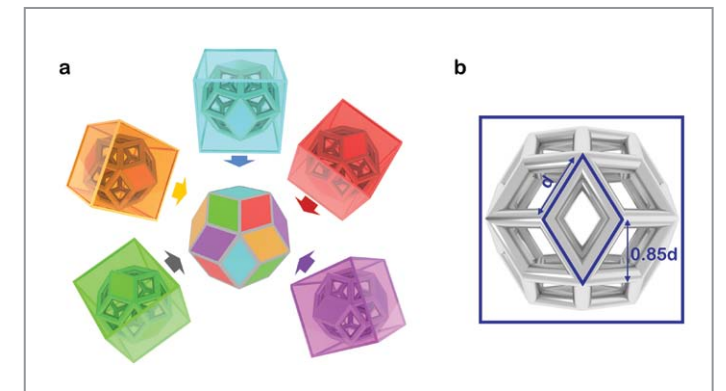
Figure 2   Expected planes giving rise to multiple Bragg scattering. (a) The rhombic triacontahedron, the most populated polyhedron, can be derived from the intersection of five cubes whose faces have indices: $\{100\}, \{\tau 1 1/\tau\}, \{\tau \bar{1} 1/\tau\}, \{1 1/\tau \tau\}, \{1 \bar{1}/\tau \tau\}$, where $\tau = (\sqrt{5} - 1)/2$ is the golden mean [7]. (b) A plane that leads to multiple Bragg scattering is shown, where d is the rod length of 1 cm.
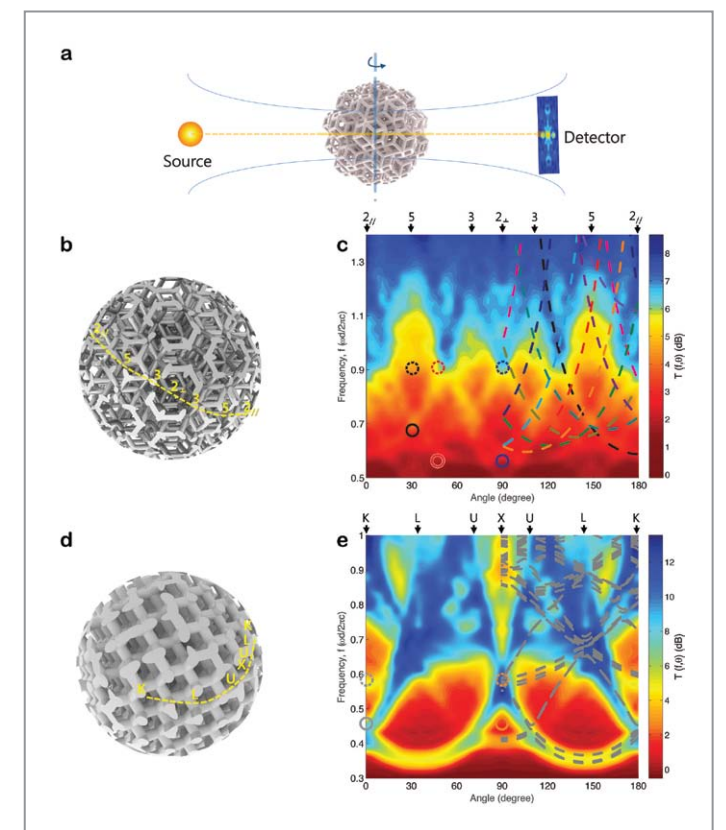
Figure 3   Calculated transmission spectra of a 3D icosahedral quasicrystal and a diamond structure. (a) Schematic of the incident beam and detector arrangement for the transmission spectra calculations. (b) The quasicrystal structure for the transmission calculation. (c) Transmission intensity as a function of the rotation angle about a two-fold rotation axis of the quasicrystal and the scaled frequency, $\omega d/2\pi c$, where c is the speed of light. The dashed curves in (c) are Bragg scattering lines from the effective Brillouin zone faces with plane distance *0.85d* in the quasicrystal. Colors indicate the zone faces of the five cubes constituting a rhombic triacontahedron (Figure 2a). (d) The diamond structure for the transmission calculation. (e) Transmission intensity as a function of the rotation angle and the scaled frequency $\omega d/2\pi c$. The diamond structure is rotated to coincide with the high-symmetry points on the first Brillouin zone boundary represented as yellow in d. The gray dashed lines in d are the calculated photonic bands on the first Brillouin zone boundary.

and the optical responses are obtained at around *15* GHz. In light of interpretation of the diamond structure, photonic bandgaps are formed on the effective Brillouin zone faces. However, the bandgap looks very narrow and loosely defined. Such behavior is similar to that of pseudogaps [4]. Indeed, a previous study by Levi et al. shows that a quasicrystal has pseudogaps [10]. We expect that localized states exist in the pseudogap regime [4], and the wave localization occurs in the low-intensity spectral regime of the quasicrystal.
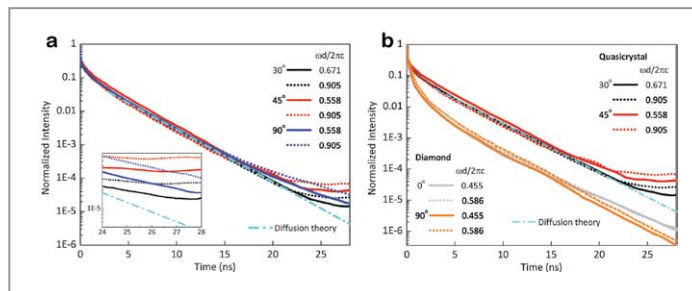
Figure 4 Time-dependent transmission intensities. (a-b) Time-dependent transmitted intensity for the quasicrystal (f) and the diamond structure (g). Photonic waves with three different scaled frequencies of *0.558, 0.671* and *0.906* transmitted for the 30°, 45° and 90° rotations of the quasicrystal. The waves at the frequencies *0.455* and *0.586* transmit for the 0° and 90° rotations of the diamond. All of the points are marked on the transmission spectra. As reference, the dashed line in cyan shows the long-term behavior predicted by the diffusion theory, $e^{-(\pi^2 Dt/L^2)t}$, where *D* is the diffusion coefficient, *L* is the sample thickness, and t is the time [11]. The fit to the theory gives *D=0.01034* cm²/ps, where *L=17.5* cm.

Time-dependent photonic wave transmission spectra

In order to investigate localized states in the quasicrystal, time-dependent transmission profiles in the low-transmission regime were obtained. In the case of the quasicrystal for 30° rotation (5-fold symmetry axis), the average transmitted intensity follows the exponential decay during longer periods of time than found in 45° and 90° rotation cases (Figure 4a). 45° and 90° rotation cases exhibit more noticeable deviation from the exponential decay. This deviation originates from wave localization because localized waves have longer lifetimes in the structure [11]. This result implies that wave propagation along a lower symmetry axis experiences significant delay in time-dependent transmission. Therefore, the wave localization depends on the wave-propagation direction in the quasicrystal, and lower-symmetry directions more strongly favor wave localization. Compared to the quasicrystal, the transmission intensities in the diamond decrease much more quickly than those in the quasicrystal owing to ballistic
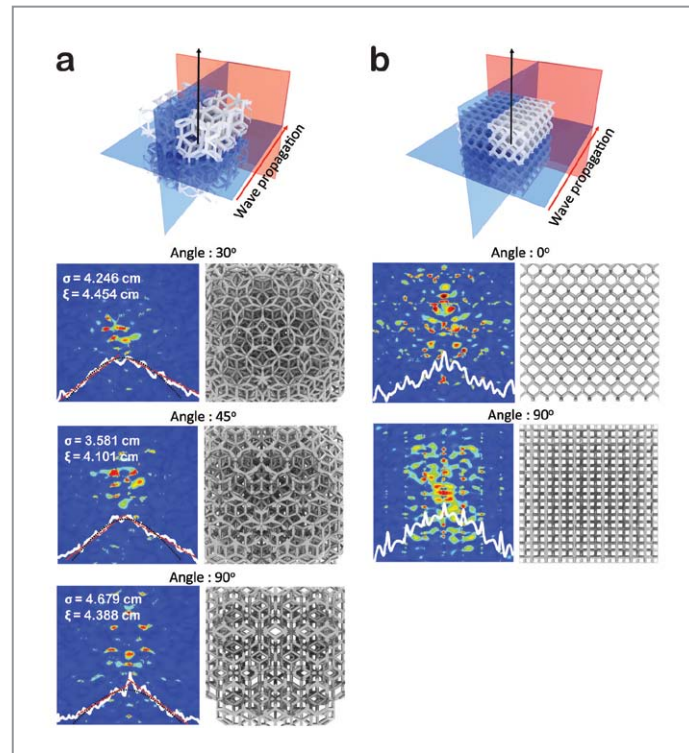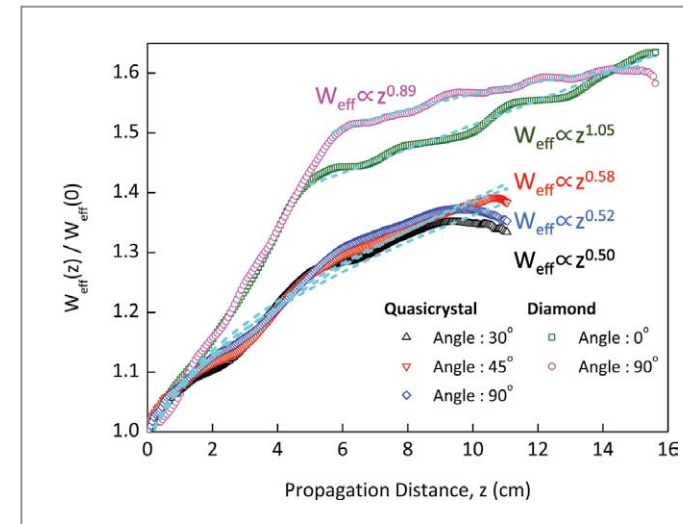

Figure 5 Photonic wave intensity distribution of the quasicrystal and the diamond. (a-b) Intensity distribution at the output face of the icosahedral (a) and diamond structures (b) for photonic waves at 0.905 $\omega d/2\pi c$ for 30°, 45°, and 90° rotations, where the initial beam width is 2.0 cm. The white lines show the average logarithmic intensities of the cross-section. The dashed black lines correspond to the diffusive contribution, $I \propto \exp(-2r^2/\sigma^2)$, and the dashed red lines represent the localization contribution, $I \propto \exp(-2r/\xi)$, where r is the distance from the center of the beam, σ is the Gaussian beam width, and ξ is the localization length. The shortest ξ is obtained for the 45° rotation, indicating the strongest localization [13]. The effective beam widths, W_{eff}, are also included.

propagation (Figure 4b) [12].

Photonic wave intensity distributions

We further obtained the average intensity distributions with a plane-wave beam source (Figures 5a and 5b). The intensity distribution of the quasicrystal exhibits its lattice structure and the diffraction peaks that are irrelevant to the lattice structure (Figure 5a). The logarithm of the intensity cross-section shows two different aspects of transport characteristics in the quasicrystal. It is known that an average intensity profile close to the Gaussian shape corresponds to diffusive transport [13], while an exponential curve indicates the localization. The average intensity profile for the 30° rotation is very similar to the Gaussian shape. Thus, the 30° rotation case indicates a diffusive-like transport. In both the 90° and 45° rotation cases, the lower-symmetry axes deviate more from the Gaussian shape, exhibiting sharper linear curves. This result implies stronger localization. Furthermore, the fit to the exponential function

yields shorter localization lengths (Figure 5a) [13]. The intensity profile for the diamond structure is quite distinct (Figure 5b). A wide range of the profile for the diamond case exhibits periodic spike patterns reflecting the lattice structure because of its ballistic transport.

Beam width evolution in 3D quasicrystals

We further obtained the effective beam width $W_{eff}(L) = \langle P(L) \rangle^{-1/2}$, where $P(L) = \left[\int I(x,y,L)^2 \, dx \, dy \right] / \left[\int I(x,y,L) \, dx \, dy \right]^2$ is the inverse participation ratio. *I* is the intensity, and *L* is the propagation distance [13, 14]. The beam width changes as a
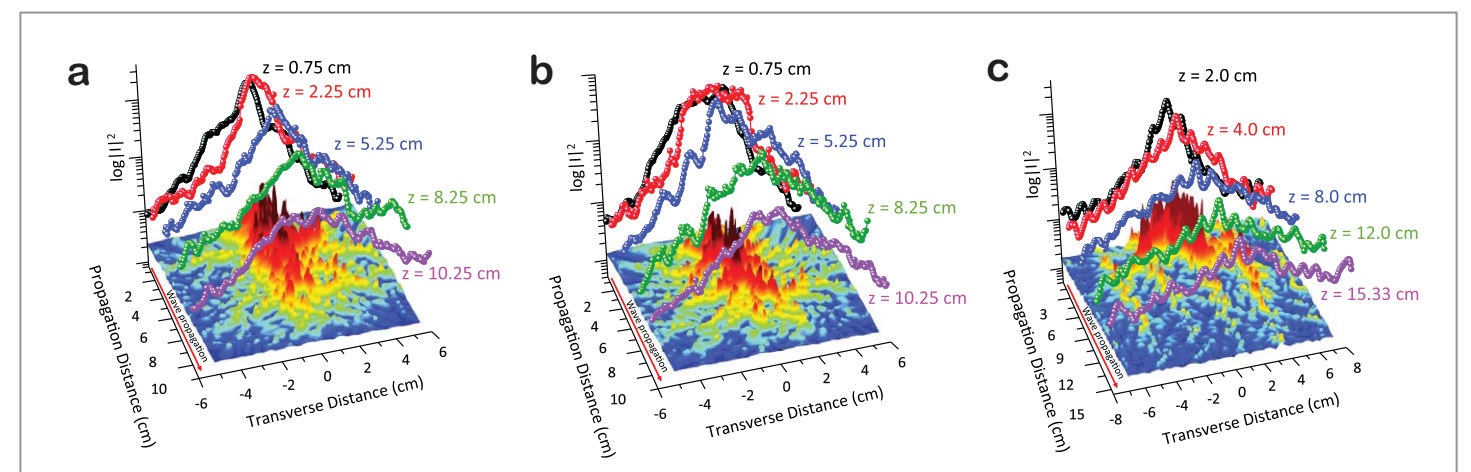

Figure 6 The beam width changes as a function of the propagation distance in the quasicrystal and the diamond. The cyan dashed lines are the fit curves for the exponent, *p*, of the expanding beam given by $W_{eff} \sim z^p$.

function of propagation distance quantitatively exhibit the wave confinement (Figure 6). In the diamond structure the beam width grows rapidly up to approximately *L=4* cm owing to the radiation from the beam center. We expect that the propagating eigenstates exclusively allow electromagnetic waves to travel through the diamond [15]. Therefore, the speckle pattern of Figure 7c appears for the eigenstates. We investigated the exponents of the width variation. The exponents are approximately *1.05* for 0° rotation and *0.89* for 90° rotation. It is known that a value close to *1.0* indicates ballistic transport [13, 14]. Figure 5 shows that the beam width change of the quasicrystal is substantially different from that of the diamond. For the quasicrystal cases, the beam width increases slowly implying stronger confinement, and the curve slope changes smoothly. The calculated exponents for 30°, 45° and 90° are very close to 0.5. This result indicates that wave propagation in the quasicrystal is diffusive-like [13, 14].

We observed similar behavior in the azimuthally averaged intensities as a function of the propagation distance (Figures 7a-c). The intensity profile for the quasicrystal is close to the Gaussian distribution in the early stage, but in the middle of the propagation a pronounced peak near the beam center position appears. We speculate that the peak comes from localized waves in the quasicrystal. Figures 3d and 3e show that the final intensity profile for the 30° rotation is more similar to the Gaussian profile than that of the 45° rotation. Therefore, the 30° rotation case is more diffusive, and propagation along the low-symmetry axis exhibits a more localized distribution and larger deviations from the Gaussian profile. These results show good agreement with the time-dependent profile results. Meanwhile, the diamond case exhibits periodic spike patterns (Figure 7c).
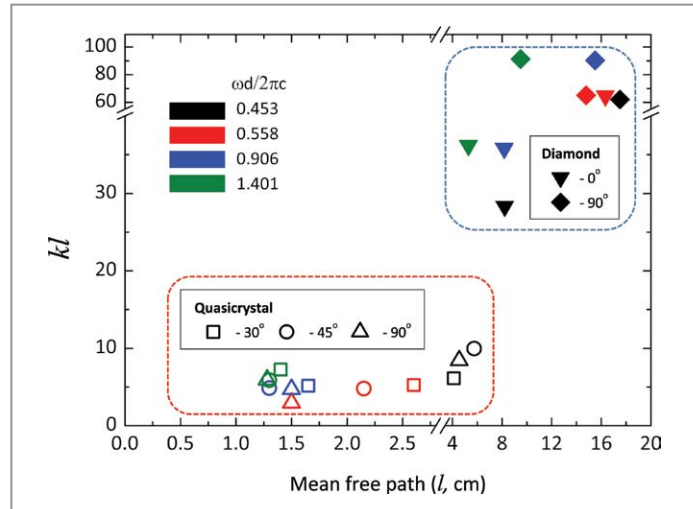

Figure 7 Logarithm of the azimuthally averaged intensity, $\log I/I_2$, as a function of *z*. 30° (a) and 45° (b) rotations of the quasicrystal and at the 0° rotation of the diamond (c). The speckle patterns, $\log I/(x,y)^2/\langle \log I/I^2 \rangle$, are superimposed at the bottom for all cases.

Figure 8   Mean free path of a 3D icosahedra quasicrystal. Plots of the mean free path versus *kl* for the quasicrystal and the diamond at three different frequencies. The transport mean free path, *l**, of the quasicrystal and the scattering mean free path, l_s, of the diamond are used.

Ioffe-Regel condition

A well-known criterion to figure out Anderson localization in disordered materials is the Ioffe-Regel condition [16], $kl^* \le 1$, where k is a wave vector, and *l** is the transport mean free path. We found that the calculated mean free paths in the quasicrystal are quite small, and *kl** is close to *5* at frequencies of *0.558* and 0.906, where the localization occurs (Figure 8). The low *kl** for the 45° rotation implies a higher chance of localization. Indeed, a recent experimental study demonstrated 3D Anderson localization under a similar condition (*kl*<5*) [17]. However, at the low frequency, *0.453*, the *kl** values exceed *5* and photonic wave localization is significantly weakened. In particular, the mean free path shortens as the frequency increases, and localization is favored at higher frequencies. Therefore, we speculate that the main driving force of localization in the quasicrystal is the short mean free path.

Conclusions

We found diffusive-like transport and a transition to localization in 3D quasicrystals without additional disorder using finite difference methods. The mean free path in the quasicrystal is short, enabling photonic wave localization. Our results indicate the universal features of wave transport in 3D quasicrystals, including electron, phonon, and acoustic waves, and should stimulate future research on the transport properties of quasicrystalline materials. In contrast to disordered materials, quasicrystalline structures can be precisely engineered to enable the control of wave localization for future photonic applications, such as lasers.

Note

This article and images are drawn from "Intrinsic photonic wave localization in a three-dimensional icosahedral quasicrystal" in *Nature Phys.* Vol.13, pp. 363~368.

References

[1] Shechtman D, Blech I, Gratias D, Cahn JW. *Phys. Rev. Lett.* 1984; 53: 1951-1953.

[2] Datta S. *Electronic Transport in Mesoscopic Systems* (Cambridge University Press, 1997).

[3] Anderson PW. *Physical Review* 1958; 109: 1492-1505.

[4] John S. *Phys. Rev. Lett.* 1987; 58: 2486-2489.

[5] Segev M, Silberberg Y, Christodoulides DN. *Nat. Photonics* 2013; 7: 197-204.

[6] Madison AE. *RSC Adv.* 2015; 5: 79279-79297.

[7] Holden A. *Shapes, Space, and Symmetry.* (Courier Corporation, 1971).

[8] Oskooi AF et al. *Comput. Phys. Commun.* 2010; 181: 687-702.

[9] Man W, Megens M, Steinhardt PJ, Chaikin PM. *Nature* 2005; 436: 993-996.

[10] Roati G et al. *Nature* 2008; 453: 895-898.

[11] Störzer M, Gross P, Aegerter CM, Maret G. *Phys. Rev. Lett.* 2006; 96: 063904.

[12] Zhang ZQ et al. *Phys. Rev. E* 1999; 60: 4843-4850.

[13] Schwartz T, Bartal G, Fishman S, Segev M. *Nature* 2007; 446: 52-55.

[14] Levi L et al. *Science* 2011; 332: 1541-1544.

[15] Joannopoulos JD, Johnson SG, Winn JN, Meade RD. *Photonic Crystals: Molding the Flow of Light.* Princeton University Press (2011).

[16] Ioffe A, Regel A. *Prog. Semicond.* 1960; 4: 89.

[17] Sperling T, Bührer W, Aegerter CM, Maret G. *Nat. Photonics* 2013; 7: 48-52.

Multi-Functional Nitrogen Self-Doped Graphene Quantum Dots for Boosting the Photovoltaic Performance of BHJ Solar Cells

Su Kang BAE

Senior Researcher
Applied Quantum Composites
Research Center
KIST Jeonbuk Institute of Advanced
Composite Materials

sbae@kist.re.kr

Introduction

Recently, carbon-based fluorescent nanomaterials, especially carbon dots (CDs), graphene quantum dots (GQDs) and graphitic carbon dots (GCDs), have attracted significant attention for their promising applications in the fields of opto-electronics, metal ion detection and biological research. Their beneficial characteristics include low toxicity, unique spin property, high photostability, excellent biocompatibility, highly tunable photoluminescence (PL) and low production cost [1, 2]. Over the last decade, various preparation methods have been identified for carbon based QDs, including acidic oxidation, hydrothermal methods, microwave synthesis, electrochemical approaches, oxygen plasma etching, catalyzed cage-opening, pyrolysis and exfoliation methods.

Among all these synthesis methods, the oxidative-cutting method as reported by Hummers [3, 4] is the one typically applied to acquire highly crystalline GQDs with a variety of O-containing functional groups (i.e., hydroxyl (-OH), carboxyl (-COOH) and epoxy groups (C-O-C)), as well as to modulate their band structural, electronic, magnetic, optical and electrochemical properties caused by quantum confinement and edge effects.

In addition to geometrical engineering, the heteroatom-doping process in GQDs is an effective strategy to regulate their inherent properties for applications in optical and electronic devices. For instance, there has been extensive research on heteroatom-doped GQDs for the incorporation of nitrogen (N)-containing groups into a graphitic carbon structure via electrochemical and post-chemical approaches [5, 6].

Unfortunately, despite the development of many different approaches to synthesis, the introduction of N-containing groups in the π-conjugated framework (graphitic structure) has yet to be achieved with respect to the control of their distributions (doping uniformity or concentration) and bonding configurations (chemical bonding structure). An additional complication has been that this incorporation of N atoms in the graphene lattice via the post-treatment process potentially disrupts the sp^2 hybridization of C atoms and even induces

structural defects in GQDs, possibly hampering their chemical stability as well as their electrical (or optical) properties. As a result, substitutional N-doped GQDs with high crystallinity and outstanding intrinsic properties still have not been obtained.

In this work, we report for the first time a simple route for synthesis of substitutional N-doped GQDs (nGQDs) from poly-acrylonitrile (PAN)-based carbon fibers (CFs) (Figure 1a). Unlike pitch-based CFs, PAN-based CFs have N-oxides (N_{ox}), pyridinic-N (N_{pyri}), pyridonic-N (N_{pydo}) and a relatively high content of quaternary-N (N_q) that is widely known to improve the electrical conductivity of carbon-based nano-materials (CNMs) without destroying sp^2-hybridized graphitic structures [7]. A less dense structure of PAN-based CFs ($\rho_{PAN} \approx 1.8$ g cm-3 and $\rho_{pitch} \approx 2.1$ g cm^{-3}) also has beneficial effects on reaction solvent diffusion and penetration into CFs [8]. Additionally, we performed an in-depth study on the optical properties of nGQDs according to the variation of N atom density via both experimental and computational analyses. Finally, nGQD-incorporated PEDOT:PSS layers were introduced into polymer solar cells (PSCs) as an efficient hole transport and photo-response layer, resulting in a 14.5% enhancement in PCE compared to devices with a pristine PEDOT:PSS layer.

Results and discussion

Structural characterization

High-resolution transmission electron microscopy (HR-TEM) images of nGQDs (Figure 1b) show that they have a narrow size distribution and mean sizes from 3 to 5 nm, regardless of the graphitization temperature of PAN-based CFs. The inset in the figure displays lattice parameters of 0.34 nm, representing the (002) lattice fringe of graphene, consistent with the reported values of carbon-based QDs prepared by different methods [9]. Atomic force microscopic (AFM) images of nGQDs in Figure 1c reveal that their heights are mostly less than 2.0 nm, suggesting that our as-prepared nGQDs typically are composed of only a few layers of graphene (less than 4 layers).

X-ray photoelectron spectroscopy (XPS) was used to characterize the elemental composition of nGQDs. As shown in Figures 2a and 2b, the elemental composition (N/C and N/O ratio) and N-bonding configuration (N_q, N_{pydi} and N_{pydo}) of nGQDs are significantly modulated by changing the heat treatment temperature of the CFs. These phenomena are related
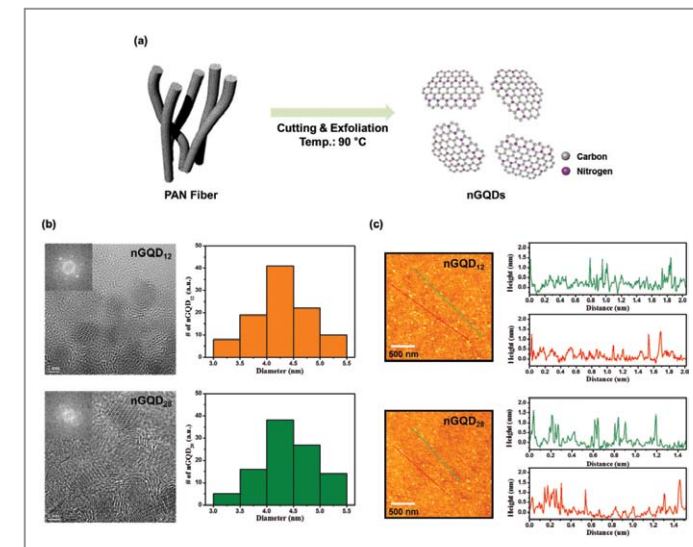
Figure 1 (a) A representative scheme for the preparation of nGQDs from PAN-based CFs by chemical cutting and exfoliation process. (b) TEM images (left, inset: FFT image) of nGQDs and their size distribution (right). (c) AFM height images of nGQDs (left) and their height profile (right).

to the heat treatment of intermediate fibers. Specifically, during a thermal treatment of PAN fibers at below 700°C, considerable amounts of various gases, such as H_2O, CO_2, CO, HCN, and NH3, are produced. Also, the evolution of N_2 begins at a high heat treatment temperature (> 700°C).

The Raman spectra in Figure 2c present the intrinsic characteristics of sp^2 carbon with a disordered structure. One can see two major Raman peaks that correspond to the D and
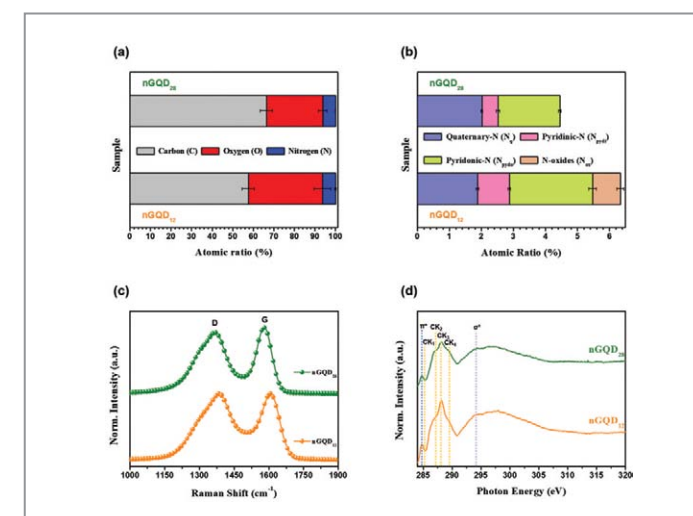
Figure 2 (a) Elemental compositions of nGQDs prepared from PAN-based CFs under the same experimental condition. (b) Chemical compositions of N-containing groups in two types of nGQDs obtained from N 1s XPS spectra. (c) Raman and (d) NEXAFS spectra of two different types of nGQDs.

G bands at ~1390 and ~1610 cm-1, respectively. By increasing the heat treatment temperature of PAN-based scrap CFs, the intensity ratio of the D and G bands (I_D/I_G) decreases and the positions of D and G bands shift to a lower wave number. On top of that, the G-band full-width at half-maximum (FWHM) of $nGQD_{12}$ is relatively larger than that of $nGQD_{28}$. These phenomena indicate that the substitution of N atoms and vacancy defects in nGQDs, which can be initially modulated by controlling the graphitization temperatures of CFs, would cause distortion of the lattice and defect pining [10]. Additionally, according to the empirical Tuinstra-Koenig relationship [11], the existence of those defects in nGQDs unavoidably affects the sp^2 cluster size (L_a), which increases by about 10% ($nGQD_{12}$: 4.3 → $nGQD_{28}$: 4.8 nm) owing to the reduction of the 0D point-like defects and thermal de-oxidation in CFs.

In order to further investigate the degree of bond hybridization in mixed sp^2/sp^3 bonded carbon, including the specific bonding configurations of neighboring functional atoms and the graphitization level of nGQDs, high-resolution *in situ* synchrotron near-edge X-ray absorption fine structure (NEXAFS) analysis (Figure 2d) was carried out. Both spectra were collected at an incidence angle of 54.7° relative to the sample to eliminate any polarization dependence. The lowest energy resonance, at approximately 284.8 eV, corresponds to the transition of C 1s core-level electrons into states of π^* symmetry around the M and L points of the graphene Brillouin zone above the Fermi level, whereas the higher energy peak at approximately 294.4 eV can be ascribed to the excitation of C 1s core electrons into dispersionless states of σ^* symmetry.

The π^* resonance is representative of the unsaturated C=C or graphitic (sp^2) bond above and below the plane, including the C-N transitions (CK_1, 285.4 eV), while the in-plane σ^* feature is typical of a C-C bond [12]. Furthermore, the three resonances in the intermediate region between the π^* and σ^* features are observed at ~286.9 eV (CK_2), ~288.1 eV (CK_3), ~289.3 eV (CK_4) and are assigned to functional groups (CK_2: C-O, CK_3: C=O and CK_4: O-C=O) that decorate the basal planes and the edge sites of nGQDs.

From these spectra, we can reconfirm that the oxidation degree of nGQDs can be effectively controlled by the heat treatment temperature of CFs. Additionally, the relative intensities of σ^* resonances indirectly offer an estimate of the relative concentration of sp^2 domain configurations in an sp^3 matrix consisting of C atoms conjugated to heteroatom-containing groups. Consequently, compared with $nGQD_{12}$, $nGQD_{28}$ can be composed of more sp^2-hybridized C atoms and even tinier amounts of non-graphitic components (i.e., structural

defects, vacancies and C atoms connected to O-including functional groups).

Optical characterization

The UV-vis absorption spectra were obtained as shown in Figure 3a. In the spectra of each nGQD, there are three absorption features: an absorption region at approximately 230 nm owing to the $\pi \rightarrow \pi^*$ transition of aromatic sp^2 domains and two peaks at about 265 and 285 nm, corresponding to the n1 and n2 → π^* electronic transition caused by heteroatom-containing bonds.

Moreover, compared with $nGQD_{28}$, $nGQD_{12}$ exhibits a larger absorption coefficient in the mid-UV and visible region (approximately 200 ~ 700 nm) caused by its higher content of substitutional N atoms as well as N- and O-rich functional groups. Similarly, the photoluminescence excitation (PLE) spectra in Figure 3b show that two electronic transitions from
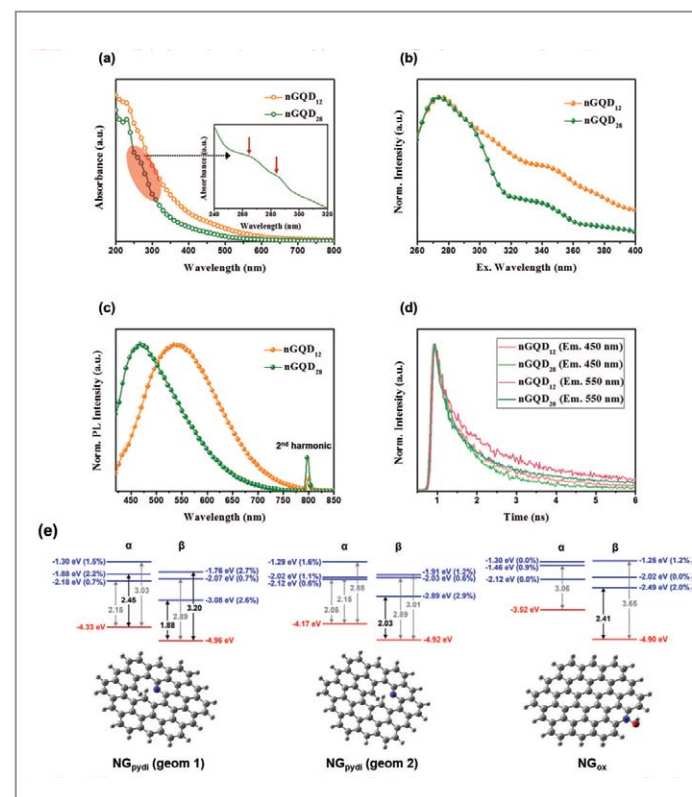
Figure 3 (a) UV-Vis absorption and (b) PLE spectra of nGQDs. (c) Normalized PL spectra of nGQDs (λ_{ex}: 400 nm). (d) TRPL spectra of nGQDs monitored at different emission wavelengths (λ_{em}: 450 nm and 550 nm, λ_{ex}: 375 nm). (e) Energy level diagram of the selected N-doped graphene QDs showing the PL transition possibility from the DFT calculations. The calculated LUMO + 2, LUMO + 1 and LUMO levels (blue) and the HOMO level (red) are displayed with the s-orbital contribution percentage. The energy gaps between the unoccupied level having s-orbital characteristics higher than 2% and the HOMO level are shown in bold type.

273 ~ 275 nm and from 330 ~ 350 nm can be considered as two transitions triggered by the $\pi \rightarrow \pi^*$ excitation and n → π^* excitation, respectively [13].

The corresponding PL spectra of nGQDs as presented in Figure 3c reveal that the emission spectra of each nGQD solution are independent of the excitation wavelength (λ_{ex}). There is a possibility that narrow size distribution as well as highly crystallinity of the nGQDs are responsible for λ_{ex}-independent PL emission. Another remarkable finding is that the PL spectrum of $nGQD_{12}$ is substantially red-shifted as well as having a broader full-width at half maximum (FWHM) compared with that of $nGQD_{28}$. Based on previous reports, these observations are caused by changes in the band edge or surface states by functional groups and substitutional N atoms (N_{pyri}, N_q and N_{ox}) [14].

In order to further explore the features of the nGQDs, we conducted PL decay experiments at room temperature with pulsed laser excitation at 375 nm (Figure 3d), and the results were fitted using a tri-exponential function to calculate the lifetime of nGQDs. The average PL decay times ($\tau_{av,nGCDs}$) for each nGCD were calculated by using the formula $\tau_{av} = (A_1\tau_1^2+A_2\tau_2^2+A_3\tau_3^2)/(A_1\tau_1+A_2\tau_2+A_3\tau_3)$, where τ_1 (fast relaxation time), τ_2 (mid-relaxation time) and τ_3 (slow relaxation time) are lifetimes, and these lifetimes are quite different (i.e., $nGQD_{12}$: 2.80 ns ↔ $nGQD_{28}$: 2.19 ns, monitored at λ_{em} = 550 nm). On top of that, the PL lifetimes for each sample are longer at the 550 nm wavelength compared with those at the 450 nm wavelength, indicating that the two emission regions have different electronic origins [15]. Based on previous reports, the heterogeneous electronic structures resulting from different dynamic behaviors of chemical states considerably impact the luminescence properties of poly-cyclic aromatic hydrocarbons. Therefore, we can say confidently that the variation of PL lifetime in nGQDs strongly reflects the chemical nature of each nGQD originating from substitutional N atoms as well as heteroatom-containing edge functional groups.

The density of states (DOS) was also estimated with simple models (the local structure of pristine (PG) and N-doped graphene QDs) using DFT calculations to conduct an investigation on the origin of PL in nGQDs. From these calculations, we can confirm that the newly formed localized states with the s-orbital characteristic, which are induced by structural distortion due to the presence of N_{pydi} and N_{ox}, permits nGQDs to bring about the additional electron transitions (Figure 3e).

Device characterization
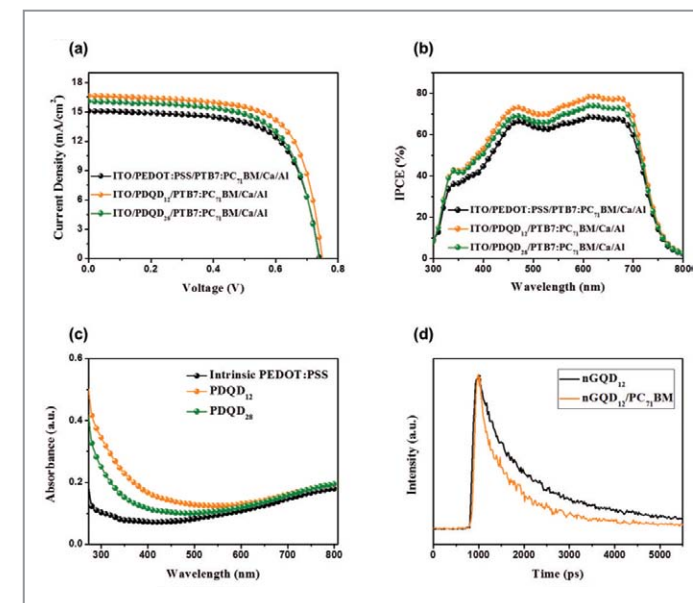
Figure 4 (a) *J-V* characteristics of the conventional $PTB7:PC_{71}BM$ solar cells under AM 1.5 G filtered illumination at an incident intensity of 100 mW/cm². (b) EQE spectra of the cPSCs with various HTLs. (c) UV-Vis absorption spectra of the pristine PEDOT:PSS, $PDQD_{12}$ and $PDQD_{28}$ films on ITO substrates. (d) Time-resolved decay curves of $nGQD_{12}$ and $nGQD_{12}/PC_{71}BM$ on ITO substrates.

In order to confirm the possibility of opto-electronic applications using the outstanding optical and electrical properties of nGQDs, we fabricated conventional bulk heterojunction polymer solar cells (cPSCs) with a configuration of $ITO/HTLs/PTB7:PC_{71}BM/MoO_3/Ag$. The control device (HTL: pristine PEDOT:PSS layer with a thickness of about 40 nm) shows a short circuit current density (J_{SC}) of 15.1 mA/cm2, an open-circuit voltage (V_{OC}) of 0.74 V, a fill factor (FF) of 0.67 and a power conversion efficiency (PCE) of 7.3% (Figure 4a). The addition of nGQDs (0.5 wt%) into the PEDOT:PSS layer results in significant enhancements in J_{SC} (15.1 mA/cm² → 16.6 mA/cm² (PEDOT:PSS with 0.5 wt% $nGQD_{12}$, denoted as $PDQD_{12}$), 16.0 mA/cm2 (PEDOT:PSS with 0.5 wt% $nGQD_{28}$, denoted as $PDQD_{28}$)).

Before determining the specific mechanism for the enhancement of J_{SC}, we acquired the external quantum efficiency (EQE) spectra of devices with different HTL films. As shown in Figure 4b, the incorporation of nGQDs into the PEDOT:PSS layer results in significant EQE improvements in the wavelength range from 340 to 700 nm. Based on previous reports, these enhancements are attributed to an increase in photogenerated charge carriers as well as an enhanced electron transport property owing to the presence of the nGQDs.
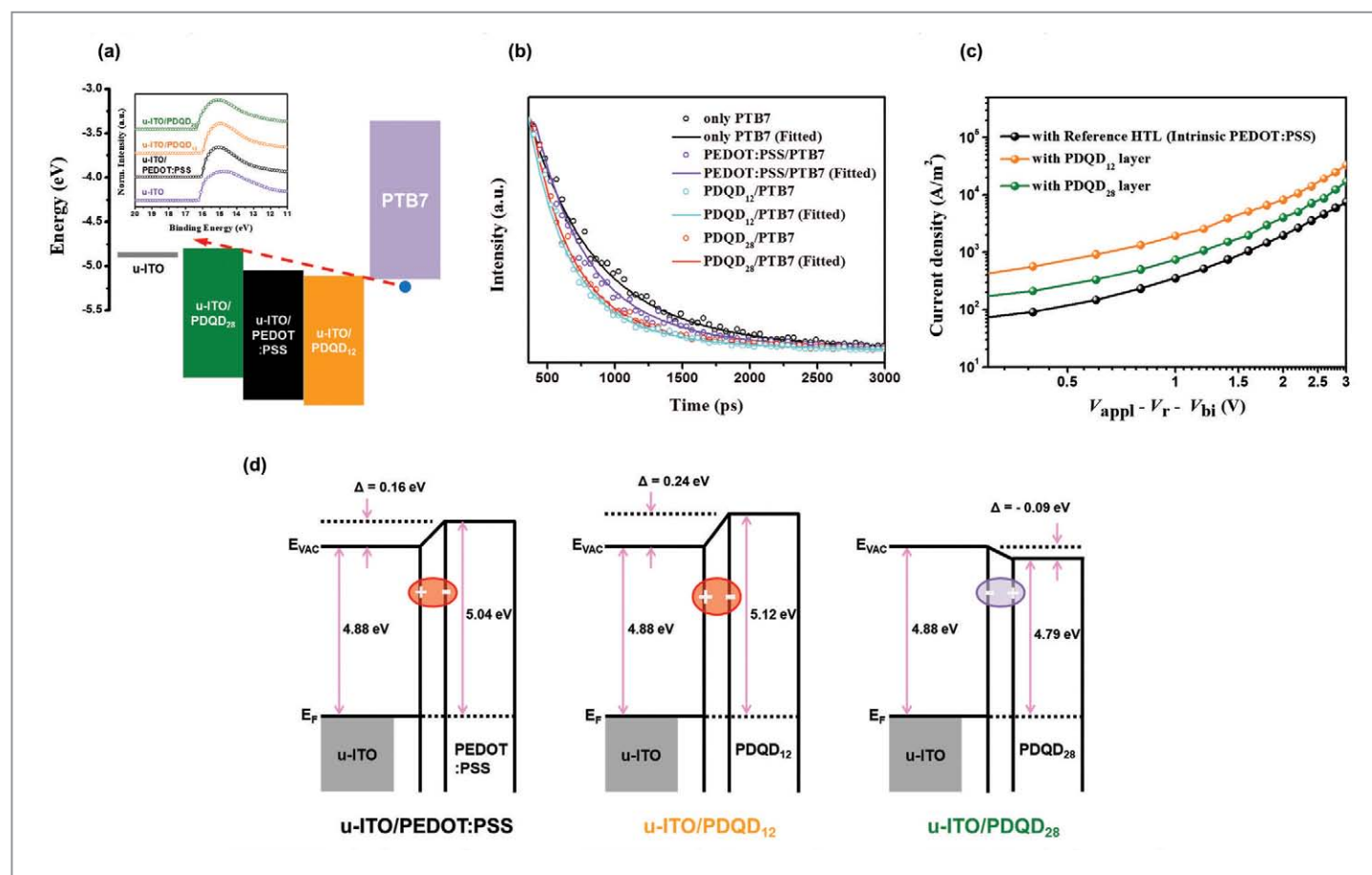
To verify the phenomenon of increasing photogenerated charge carriers, we first measured the light absorption spectra

of each HTL. As shown in Figure 4c, nGQD-incorporated HTL films exhibit additional spectral responses between 300 and 500 nm in comparison to the pristine PEDOT:PSS layer. $PDQD_{12}$ in particular possesses higher light-absorption in the visible region than $PDQD_{28}$ due to its many substitutional N atoms as well as N- and O-rich edge-functional groups. Additionally, PL decay lifetimes of nGQDs/$PC_{71}BM$ samples monitored at 500 nm are much shorter than that for pristine nGQD samples, implying that the photo-induced excitons generated in HTLs are well-dissociated at nGQDs/$PC_{71}BM$ interfaces and efficient electron (or energy) transfers from nGQDs to $PC_{71}BM$ arise in these systems (Figure 4d). From these findings, we can expect that nGQDs will play an important role as efficient sub-light harvesters and down-energy converters for the next generation of free charge carriers in cPSCs.

In order to explore the charge transfer dynamics in cPSCs with PEDOT:PSS-based HTLs, the ultraviolet photoelectron spectroscopy (UPS) spectra were first acquired under ultra-high vacuum conditions ($\sim 10^{-8}$ torr). As shown in Figure 5a, the work-function of PDQD12 (5.12 eV) is closer to the HOMO energy level of PTB7 (5.15 eV) than that of $PDQD_{28}$ (4.79 eV). The good energy level matching between $PDQD_{12}$ and PTB7 can enhance the charge extraction and transport efficiency, resulting in the improvement of photovoltaic performance. Additionally, incorporation of $nGQD_{12}$ into the PEDOT:PSS layer leads to a vacuum level shift of +0.24 eV, whereas introduction of $nGQD_{28}$ results in a shift toward higher energy (-0.09 eV) (Figure 5d). In accordance with UPS results, TRPL measurements of the PTB7 show a decrease in the PL lifetime of the photo-active layer from 688 ps (w/o PEDOT:PSS layer) to 441 ps in the presence of $PDQD_{12}$ (Figure 5b). Also, the hole mobility (μh) increases from 1.05×10^{-4} cm2 V^{-1} S^{-1} (intrinsic PEDOT:PSS layer) to 5.42×10^{-4} cm2 V^{-1} S^{-1} ($PDQD_{12}$) as shown in Figure 5c. Therefore, we can expect that $nGQD_{12}$ can act as sub-efficient hole extraction sites in HTL films.

Conclusion

We report a facile method to prepare nGQDs from PAN-based CFs that can readily modulate the N/C and O/C atomic ratios and N-bonding configurations by altering the post-heat treatment temperature of CFs. Owing to the chemical nature of each CF, as-prepared nGQDs possess not only a high degree of optical tunability but also have prominent crystallinity leading to λ_{ex}-independent PL emission. Finally, in order to verify the possibility of opto-electronic applications using the remarkable optical and electrical properties of nGQDs, we fabricated cPSCs with the nGQD-incorporated PEDOT:PSS interlayer as a multifunctional interfacial layer, resulting in a 14.5% improvement in PCE compared to a device with a pristine PEDOT:PSS layer. Therefore, we anticipate that with further study our nGQDs will soon provide significant improvements to photocatalyst, energy storage and biological labeling applications.

Note

This article and images are cited from "Multi-functional nitrogen self-doped graphene quantum dots for boosting the photovoltaic performance of BHJ solar cells" in *Nano Energy*, 2017, Vol.34, pp. 36 ~ 46.
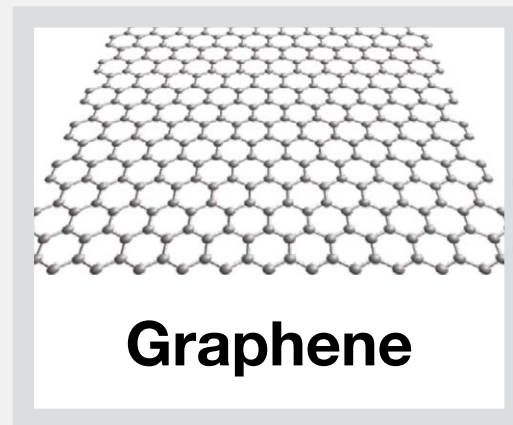
References

[1] Ding Z, Quinn BM, Haram SK, Pell LE, Korgel BA, Bard AJ. *Science* 2002; 296: 1293-1297.

[2] Gao XH, Cui YY, Levenson RM, Chung LWK, Nie SM. *Nat. Biotechnol*. 2004; 22: 969-976.

[3] Pan D, Zhang J, Li Z, Wu M. *Adv. Mater*. 2010; 22: 734-738.

[4] Pan D, Guo L, Zhang J, Xi C, Xue Q, Huang H, Li J, Zhang Z, Yu W, Chen Z, Li Z, Wu M. *J. Mater. Chem*. 2012; 22: 3314-3318.

[5] Liu Q, Guo B, Rao Z, Zhang B, Gong JR. *Nano Lett*. 2013; 13: 2436-2441.

[6] Yeh T-F, Teng C-Y, Chen S-J, Teng H. *Adv. Mater*. 2014; 26: 3297-3303.

[7] Huan TN, Khai TV, Kang Y, Shim KB, Chung H. *J. Mater. Chem*. 2012; 22: 14756-14762.

[8] Frank E, Steudle LM, Ingildeev D, Spçrl JM, Buchmeiser MR. *Angew. Chem. Int. Ed*. 2014; 53: 5262-5298.

[9] Wang G, Shen X, Yao J, Park J. *Carbon*. 2009; 47: 2049-2053.

[10] Kim M-A, Jang D, Tejima S, Cruz-Silva R, Joh H-I, Kim HC, Lee S, Endo M. *Sci. Rep*. 2016; 6: 22988-7.

[11] Tuinstra F, Koenig JL. *J. Chem. Phys*. 1970; 53: 1126-1130.

[12] Dubin S, Gilje S, Wang K, Tung VC, Cha K, Hall AS, Farrar J, Varshneya R, Yang Y, Kaner RB. *ACS Nano*. 2010; 4: 3845-3852.

[13] Li L-L, Ji J, Fei R, Wang C-Z, Liu Q, Zhang J-R, Jiang L-P, Zhu J-J. *Adv. Funct. Mater*. 2012; 22: 2971-2979

[14] Shen J, Zhu Y, Chen C, Yang X, Li C. *Chem. Commun*. 2011; 47: 2580-2582.

[15] Bao L, Zhang Z-L, Tian Z-Q, Zhang L, Liu C, Lin Y, Qi B, Pang D-W. *Adv. Mater*. 2011; 23: 5801-5806.

Figure 5 (a) Simplified energy diagram at the anode side of the cPSCs with various HTLs. (inset: UPS spectra of UV-treated ITO (u-ITO) and u-ITO/PEDOT:PSS with/without nGQDs.) (b) Time-resolved decay curves of only PTB7, PEDOT:PSS/PTB7, $PDQD_{12}$/PTB7 and $PDQD_{28}$/PTB7 layers on ITO substrates. (c) Dark *J-V* curves for hole-only devices incorporating PTB7:PC71BM (1:1.5 w/w). (d) Energy level diagrams near the ITO/HTLs in the presence of an interfacial dipole with negative or positive magnitude.

Bio / Medical

Materials / Systems

Energy / Environment

Research Highlights

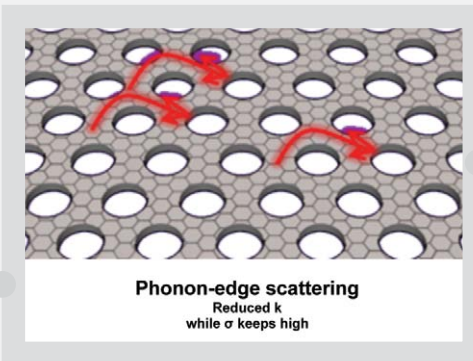KIST News

VKIST

Up Close

Interview

Significantly reduced thermal conductivity and enhanced thermoelectric properties of single- and bi-layer graphene nanomeshes with sub-10 nm neck-width

Jeong Gon SON

Senior Researcher
Photoelectronic Hybrid Research Center
National Agenda Research Division

jgson@kist.re.kr

Jin Woo OH

Photoelectronic Hybrid Research Center
National Agenda Research Division

jwoh@kist.re.kr

Graphene
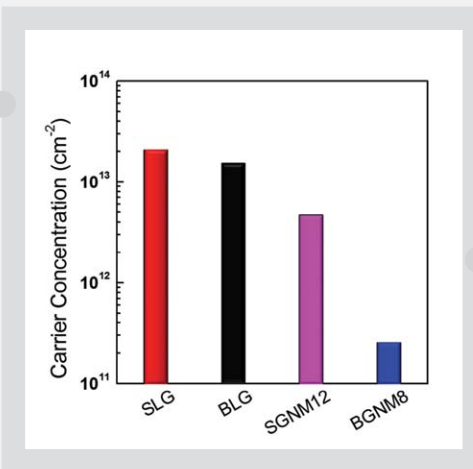
- **High electrical conductivity** (σ)
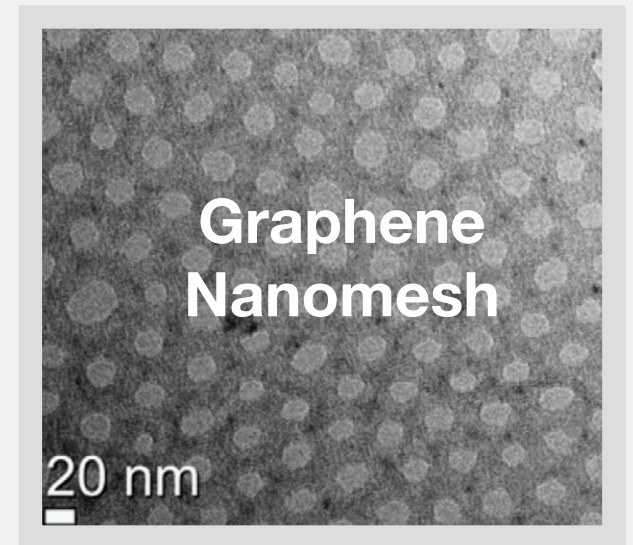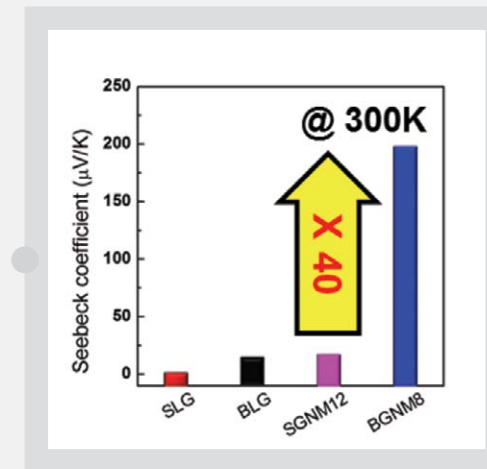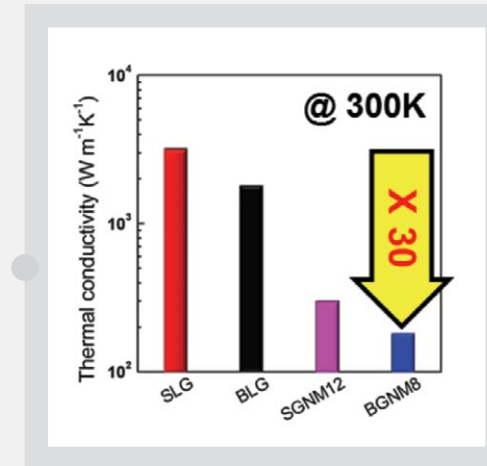- **Zero-bandgap material** (~n)
- **High thermal conductivity** (k)

Phonon-edge scattering

Reduced k
while σ stays high

Quantum confinement

Enhance thermopower(S) by
opening electronic bandgap

Graphene Nanomesh

20 nm

- Keep **σ** high
- **n control** for higher S
- Lower **k**

Abstract

When graphene is shrunk into ~10 nm scale graphene nanoribbons or nanomesh structures, it is expected that not only electrical properties but also thermal conductivity and thermoelectric property are significantly altered due to the quantum confinement effect and extrinsic phonon-edge scattering. Here, we fabricate large-area, sub-10 nm single- and bilayer graphene nanomeshes from block copolymer self-assembly and measure the thermal conductivity, thermoelectric and electrical transport properties to experimentally verify the effect of sub-10 nm quantum confinement, phonon-edge scattering and cross-plane coupling. Among the large variety of samples, bilayer graphene nanomesh having 8 nm-neck width showed significantly low thermal conductivity down to ~78 W m-1 K-1, which is the lowest thermal conductivity for suspended graphene nanostructures, and a high thermopower value of -520 µV K-1, while still showing comparably high carrier mobility. Classical and quantum mechanical calculations successfully supported our nanomesh approach, which can achieve high thermoelectric properties based on significantly reduced thermal conductivity and higher thermopower due to the confined geometry.

Bio / Medical Materials / Systems Energy / Environment Research Highlights KIST News VKIST Up Close Interview

Technical Review

Metal-Organic Framework Cathodes Based on a Vanadium Hexacyanoferrate Prussian Blue Analogue for High-Performance Aqueous Rechargeable Batteries

Kyung Yoon CHUNG

Principal Researcher
Center for Energy Convergence
Green City Technology Institute

kychung@kist.re.kr

Introduction

Rechargeable batteries represent the most promising storage devices for energy storage systems (ESSs) because of their many desirable traits, including environmentally friendly operation, low-cost maintenance, high storage efficiency, high cycling stability, and satisfactory energy and power performance [1, 2]. To date, Li ion batteries (LIBs) have been successfully demonstrated as feasible power sources, especially for portable devices, but their application into large-scale stationary ESSs is less than ideal due to the limited sources and ever-increasing cost of raw lithium as well as the high flammability and expense of organic electrolytes which make up a large portion of commercial LIBs [3, 4]. Consequently, aqueous rechargeable batteries (ARBs) with readily accessible electroactive guest ions, e.g., H^+ (or H_3O^+), Na^+, Mg^{2+}, K^+, or Zn^{2+}, currently represent the most suitable energy devices for ESSs.

ARBs have a number of advantages over conventional LIBs because of their outstanding ionic conductivity (two-fold higher than that of organic electrolytes), durability, use of a less costly separator, superior safety, and more flexible manufacturing conditions [5-7]. Although the energy density of ARBs is somewhat lower than that of organic systems, this is less important for large-scale ESSs than the cost effectiveness, low maintenance, and safe performance found in ARBs.

Developing new kinds of electrode materials that are compatible with aqueous systems is also key to the production of high-performance ESSs. Characteristics of active materials that meet the requirements of large-scale stationary ESSs include: 1) reasonably large lattice parameters to enable a high concentration of interstitial sites and facile diffusion paths for guest ions; 2) a well-preserved crystal structure upon ion insertion/extraction; 3) a multiple electron-involved redox reaction; and 4) a synthesis method with simple, bulk, and low temperature processes.

Very recently, promising results have been obtained from using metal-organic frameworks based on Prussian blue analogues (PBAs) as electrode materials for rechargeable

batteries [8-12]. PBAs typically have a formula of $A_xM'_h[M''(CN)_6]_k\square_l \cdot zH_2O$, simply denoted as M'/M'' PBA, where A, M'(M''), and $\square$ represent the mobile ions, transition metal ions, and vacancy of $[M''(CN)_6]^{n-}$, respectively. In the PBA structure, high spin M' and low spin M'' ions are octahedrally coordinated with N and C atoms, respectively. Due to the cyanide ($-C\equiv N-$) group linking the octahedrals of M' and M'', PBAs possess unique crystallographic and chemical characteristics. First, PBAs typically have large lattice parameters greater than 10 Å [8], which is beneficial for the facile diffusion of electroactive mobile ions and high structural stability against repeated ion insertion and extraction. In addition, the activation energy required to transfer the guest ions is effectively relieved by the weakened bond strength between the frameworks and the ions [9]. In spite of these outstanding advantages, the specific capacity of most PBAs obtained with aqueous electrolytes is limited to less than ~ 60 mAhg^{-1} [10–12]. This limitation is indicative of the optimal combination of transition metal ions, i.e., M' and M'', which is the most crucial factor in improving their electrochemical performance, including their specific capacity, rate capability, and operating potential, because the electrochemical process of PBAs is mostly governed by the electrochemical process of the metal ions upon insertion/extraction of guest ions.

In this article we discuss a new kind of PBA constituted with vanadium and iron ions (V/Fe PBA) which was fabricated using a simple co-precipitation method. Its electrochemical performance as well as related mechanisms of energy storage were investigated using aqueous electrolytes. To the best of our knowledge, this is the first report to investigate vanadium hexacyanoferrate as an electrode material for rechargeable batteries. Until now, only single transition metal ions, Fe ions in most cases, were believed to be electrochemically activated under aqueous electrolyte systems; previous studies have focused on Cu/Fe [10, 13] and Ni/Fe PBAs [12, 14]. However, since vanadium ions exhibit various oxidation states ranging from +2 ~ +5 and a facile electrochemical availability within the potential window of the aqueous electrolyte in which the aqueous electrolyte remains stable, it was reasonable to assume that using both V and Fe ions would effectively contribute to the multiple-electron energy storage process, i.e., an enhancement in the specific capacity. Furthermore, vanadium has the lightest atomic weight among the transition metal ions constituting the PBA structure, a distinct advantage in terms of improved gravimetric energy and power density.

Results and discussion

Electrochemical behavior of V/Fe PBAs and related energy storage mechanism

The electrochemical performance of the V/Fe PBA-based cathodes was investigated using an aqueous electrolyte of 0.5 M Na_2SO_4 + 5 M H_2SO_4 because V/Fe PBA becomes electrochemically and chemically stable under acidic conditions. Galvanostatic charging/discharging was performed under a current density of 110 mAg-1 (~ 1.2 C) within a potential range of 0.45 to 1.15 V vs. Ag/AgCl, as shown in Figure 1A. The synthesis procedure directly affected the electrochemical performance. Capacity and retention were improved in the following order: co-precipitation with HCl > co-precipitation without HCl > simple mixing, implying that a high crystallinity induces a high degree of electrochemical utilization and cycling stability. Surprisingly, the V/Fe PBA cathodes synthesized by co-precipitation with the addition of HCl showed a high discharge capacity of 91 mAhg-1, which was a significant improvement compared to previous studies on PBAs used in aqueous systems: ~ 55 mAhg-1 for Cu/Fe PBA under 1 C [10]; ~ 50 mAhg^{-1} for Ni/Fe PBA under 0.2 C [11]; ~ 60 mAh-1 for Ni/Fe PBA under 0.83 C [12]; and 50 ~ 65 mAhg^{-1} for Cu/Ni/Fe PBA under 50 mAg^{-1} [15]. Additionally, the V/Fe PBA exhibited a superior energy storage ability compared to oxide and
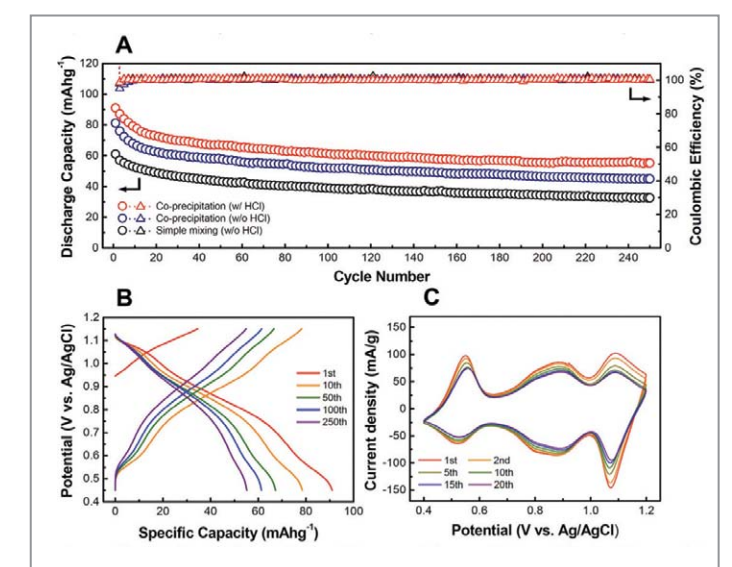
**Figure 1**   (A) Discharge capacity and coulombic efficiency depending on the synthetic procedures. (B) Potential profiles of the cathodes synthesized by co-precipitation (with HCl), evolving over 250 cycles (potential range: 0.45 – 1.15 V vs. Ag/AgCl, charge/discharge current density: 110 mAg^{-1}). (C) CVs within a potential range of 0.4 to 1.2 V vs. Ag/AgCl for the initial 20 cycles (scan rate: 0.1 mVs^{-1}).

phosphate electrodes: 73 mAgh^{-1} for submicron-sized LiMn$_2$O$_4$ under 1.5 C [16]; 60 ~ 80 mAgh^{-1} for K$_{0.27}$MnO$_2$ under 200 mAg^{-1} [17]; and 75 mAgh^{-1} for LiMnPO$_4$ under 0.25 mAcm-2 [18]. Based on the experimentally determined composition of the synthesized V/Fe PBA cathodes, a capacity of ~ 43 mAhg^{-1} was achieved for the single-electron process, indicating that the electrochemical processes of the V/Fe PBA cathodes involved multiple-electron redox reactions. In the discussion which follows, only the results associated with the cathodes synthesized by co-precipitation with HCl are presented. Specific capacity steeply decreased during the early stage of cycling; however, a stable delivery capacity was observed after ~ 150 cycles with a greatly mitigated decreasing rate. The V/Fe PBA cathode exhibited a capacity of ~ 55 mAhg^{-1} at the end of the cycling (250th cycle), which was still higher than or comparable with the values in the previous reports on PBAs listed above.

The changes in potential (Figure 1B) during charging/discharging showed a sloping tendency, and three regions with gentle slopes were distinguished. The three distinguishable segments of the potential regions implied that the electrochemical process of the V/Fe PBA cathode proceeded via three types of redox reactions based on a solid-solution behavior. The overall shape of the profile was not altered by the cycling, although the charge/discharge capacity slightly decreased. Figure 1C depicts the cyclic voltammograms (CV) of the V/Fe PBA cathodes within a potential range of 0.4 – 1.2 V vs. Ag/AgCl for the initial 20 cycles. As noted in the potential profile, the CVs confirmed that the V/Fe PBA-based cathodes electrochemically reacted through three redox processes, with middle reaction potentials (Emid), defined as (E$_{oxidation}$+E$_{reduction}$)/2, of 0.54, 0.90, and 1.08 V vs. Ag/AgCl from the CVs. The clearly distinguishable three pairs of redox reactions continuously occurred and were reversible during the cycles investigated. According to a previous study on electrochemically deposited V/Fe PBA thin films [19], the first, second, and third pairs of anodic and cathodic peaks are assumed to be related to the reversible electrochemical reactions of V(III) + H$_2$O ↔ [V(IV) O]$^{2+}$ + 2H++ e–, Fe(II) ↔ Fe(III) + e–, and [V(IV)O$_2$H]+ ↔ [V(V)O$_2$]++ e– + H+, respectively, although the corresponding half reaction potentials are slightly different, especially for the first pair of redox reactions. This difference may have been caused by the dissimilarity in stoichiometry of the synthesized materials and resulting local crystallographic structure. The small polarization observed in the CVs, indicating fast ion diffusion kinetics, was attributed to the structural features of the PBA framework. First, the zeolitic and ligand water molecules constituting the framework formed a three-dimensional
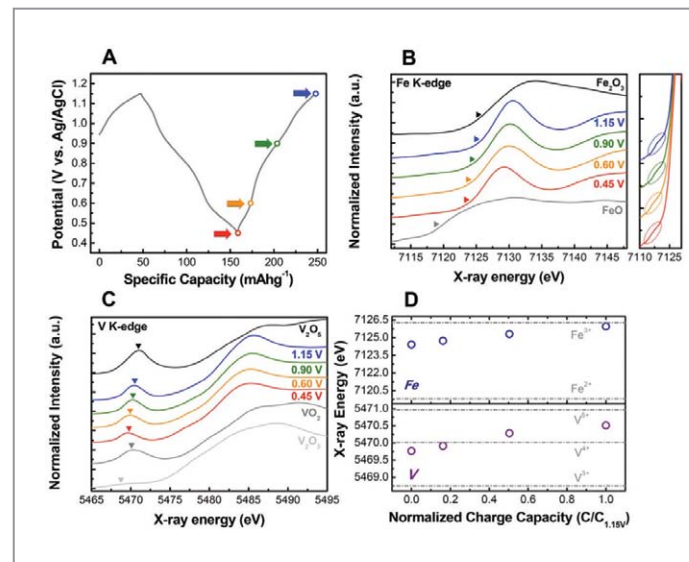
Figure 2 (A) Potential profile of the V/Fe PBA cathodes under a current density of 11 mAhg^{-1}; the open circles indicate the potentials at which the *ex-situ* XANES spectra were acquired (the spectra were measured after the formation cycle). K-edge XANES spectra of iron (B) and vanadium (C) ions with reference spectra of FeO$_x$ and VO$_x$ (right of Figure B are the magnified graphs for the pre-edge peaks of iron indicated by dotted circles). (D) K-edge energy position at a normalized intensity of 0.5 for Fe and at a pre-edge peak for V (indicated by the triangles in Figures B and C, respectively) as a function of the normalized charge capacity (C/C$_{1.15V}$), defined as the charge capacity at a certain potential divided by that at 1.15 V, shown in Figure A. Dashed lines are energy position from the reference spectra.

hydrogen-bonding network inside the PBA structure that allowed rapid proton kinetics [20], which is known as the "Grotthuss mechanism." Second, because of the large lattice parameter of PBA, it is possible that the guest ions were inserted into the structure without or with only partial dehydration and that the solvation shell surrounding the ion acted as a shield layer to mitigate the electrostatic repulsion among the guest ions, thereby lowering the activation energy for ion diffusion.

An analysis based on *ex-situ* X-ray absorption near-edge spectroscopy (XANES) was performed to monitor the changes in the electronic structures of vanadium and iron ions during cycling. The open circles and arrows shown in Figure 2A indicate the potentials at which the *ex-situ* XANES measurements were performed. Prior to XANES analysis, a single cycle of charging followed by discharging with a current density of 11 mAg^{-1} proceeded as a formation cycle; then, all the cathodes were recharged to certain potentials and held at the corresponding potentials for 30 min to induce a complete electrochemical reaction. Figures 3B and 3C show the typical Fe and V K-edge spectra observed from V/Fe PBAs depending on the electrode potential during charging, respectively. The reference spectra of FeO, Fe$_2$O$_3$, V$_2$O$_3$, VO$_2$, and V$_2$O$_5$ were also included in the figure. As shown in both XANES results, two
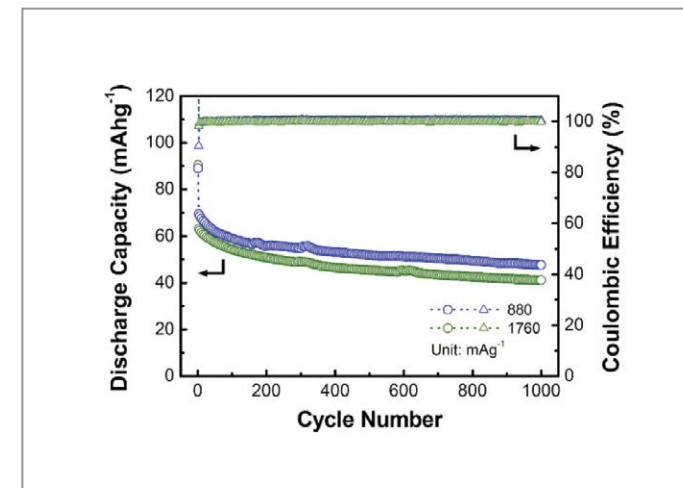
Figure 3 Discharge capacity and coulombic efficiency as a function of the cycle number with a charge/discharge current density of 880 and 1760 mAg^{-1}, respectively.

intensity peaks, a so-called main absorption peak and a pre-edge peak, located at 10 – 20 eV lower energy relative to that of the main peak, were observed. The intensity of the pre-edge peak of the Fe K-edge was relatively weaker compared to that of the V K-edge (right of Figure 2B). Theoretically, the main absorption peak originated from the electron transition to the 4p continuum state with 1s–4p electronic transition and the shape resonance of the transition metal ions [21]. The pre-edge peak is generally recognized in the XANES spectra of first-row transition metals in the periodic table, e.g., Ti to Cu [22]. The peak is dipole-forbidden in nature, reflecting the excitation of the electron related to a bound-to-bound 1s-to-3d transition, and becomes a partially allowed transition due to 3d–4p orbital hybridization [23]. In addition, the intensity of the pre-edge peak is correlated with the degree of distortion of the sublattice, i.e., the peak intensity increased with the degree of deviation from the ideal octahedral (centrosymmetry) [24]. Regarding the geometric coordination of Fe ions, the weak intensity of the pre-edge peak was characteristic of a high centrosymmetric sublattice structure of Fe ions surrounded by cyanide groups. The more remarkable pre-edge peak was identified in the V K-edge, presumably due to the local coordination of the V ions which slightly deviated from the ideal octahedral coordination because the ions were bonded with not only the cyanide group but also oxygen atoms with probabilities of 5/6 and 1/6, respectively.

Overall, the systematic shifting of the spectra to higher X-ray energy was observed in both the Fe and V K-edges with increasing electrode potential. The valence states of transition metal ions are linearly dependent on the particular energy point of XANES, e.g., the peak energy position or edge step

of the XANES spectra [22, 25, 26]. The energy positions at a normalized intensity of 0.5 and at the pre-edge were calculated for Fe and V, respectively, and the energy is indicated by triangles in Figures 3B and 3C. Figure 2D depicts the calculated energy as a function of the normalized charge capacity, i.e., the capacity obtained at the potential at which the *ex-situ* XANES analysis was performed, divided by that at the end of charging (1.15 V). The calculated X-ray energies of the Fe and V K-edges from V/Fe PBAs systematically increased with the increase in the depth of charging. Also, from comparison with the energy position of the reference oxides, it is confirmed that charge compensation upon charging/discharging occurred as a result of the changes in the valance state of V and Fe ions with V^{3+}↔ V^{4+}↔ V^{5+} and Fe^{2+}↔ Fe^{3+}, respectively, although the exact formal oxidation states of the ions could not be determined due to the large difference in crystallographic structure between V/Fe PBAs and standard oxides. Based on this result, the Fe and V ions involved in the entire energy storage process of V/Fe PBA cathodes were revealed, although the electrochemical reaction of most of the previously studied PBAs was solely manifested by that of the Fe ions. Therefore, our results indicate that multiple redox reactions occurring at the Fe and V sites contributed to the superior energy storage ability of the V/Fe PBAs.

Long-term cycling performance

Long-term cycling stability is also considered one of the most important factors in determining the performance of batteries. Figure 3 shows the cycling performance of the V/Fe PBA cathodes with high charge/discharge current densities of 880 and 1760 mAg^{-1} for 1000 cycles. The charge/discharge times of the cathode under 880 and 1760 mAg^{-1} were as fast as ~ 5 and 2.5 min, respectively. In both cases, the first two cycles were cycled with 110 mAg^{-1} to activate the electrodes. The cathodes cycled with current densities of 880 and 1760 mAg^{-1} exhibited discharge capacities of 70 and 64 mAhg^{-1} at the third cycle, respectively. After a rapid decay in the discharge capacity during the initial cycle stage, the capacity decreased at a low rate of 0.015 ~ 0.018 % per cycle, and the rate was more than one order of magnitude lower than that observed in the initial cycles. It is interesting that the capacity retention of the V/Fe PBA cathodes improved with the charging/discharging current density; the capacity retention at the 250th cycle was 61, 80, and 79 % for current densities of 110, 880, and 1760 mAg^{-1}, respectively. As mentioned previously, the contribution of the first and third pairs of redox reactions to the total capacity became less noticeable as the charge/discharge current density

Bio / Medical

Materials / Systems

Energy / Environment

Research Highlights

KIST News

VKIST

Up Close

Interview

increased, which means that the capacity reduction of the cathodes cycled with higher current density was almost entirely dependent on the deterioration of the second pair of redox reactions, whereas all redox reactions affected the capacity retention at low current densities. Within the potential range in which the first and third redox reactions occurred, the cathodes cycled under high current density exhibited an electrochemical capacitor-like behavior, which usually exhibited excellent cycling stability. Therefore, more stable cycling performance was achieved at higher charging/discharging current density, although the initial capacity was somewhat sacrificed.

Investigation on microstructural, spectroscopic, and chemical changes during cycling

To identify the origin of capacity fading for the V/Fe PBA cathodes, changes in the microstructural, chemical, and spectroscopic characteristics during cycling were analyzed. The surface morphologies of pristine and cycled electrodes shown in Figure 4A confirmed that the overall surface morphology of all the cycled V/Fe PBA cathodes was almost identical to that of the pristine cathode in that the particulate shape of all of the cathodes was retained as nanoparticle aggregates throughout all of the investigated cycles. Figure 4B shows the XRD patterns of pristine and cycled cathodes at the 50th, 100th, and 250th cycles. There were no noticeable changes in the diffraction peaks upon repeated insertion and extraction of the guest ions, indicating that the overall crystal structure of the cathodes

Figure 4 Changes in the surface morphology (A) and XRD patterns (B) of the cathodes during cycling. Insets of Figure A are high-magnification images. Diffraction peaks from V/Fe PBA and CFP are marked with circles and asterisks, respectively. (C) Nyquist plots evolved during cycling measured at the fully charged state at 1.15 V. The observed data and simulated curves corresponding to the equivalent circuit model (inset) are denoted as open circles and dotted lines, respectively. (D) Changes in resistance (R_e (electrolyte), R_{film} (film), and R_{ct} (charge transfer)) with cycle number calculated from the simulation of the Nyquist plots. The EIS measurement was performed 3 times at each cycle number, and the standard deviation is indicated by the error bars. (E) Concentration of dissolved V and Fe ions as a function of the cycle number measured by ICP-OES. The cathodes were cycled under a charge/discharge current density of 110 mAg^{-1} within a potential range of 0.45 – 1.15 V vs. Ag/AgCl.

was preserved during repeated cycling. Therefore, the V/Fe PBA cathodes were highly resistant to macroscopic damage during cycling, i.e., reduction in the degree of crystallinity or amorphization.

As shown in Figure 1B, the potential gap between the charge and discharge profiles gradually widened, and the boundary between the three potential regions was less distinguishable as the number of cycles increased, indicating that polarization accumulated with cycling. EIS was performed to determine the main factor detrimental to the increase in polarization. Figure 4C presents Nyquist plots of the observed data (open circles) and simulated curves (dotted lines) as a function of the cycle number. The observed result was simulated using the equivalent circuit shown in the inset of Figure 4C. The circuit model was designed to separate each resistance contribution for the overall polarization and was composed of three resistance components (the electrolyte (R_e), film (R_{film}), and charge transfer (R_{ct})), two constant phase elements (CPE), and the Warburg impedance (W). The V/Fe PBA crystalline phase was surrounded by an amorphous-like region. Also, an enhancement in specific capacity (Figure 1A) and reduction in polarization was observed at the higher degree of crystallinity. Based on these results, it can be infered that the surrounding amorphous structure acted as an additional interface hindering a facile electrochemical process. Therefore, the effect of the amorphous region on the polarization accounting for the resistance component of the film (R_{film}) is reasonable. The calculated resistance components as a function of the cycle number are shown in Figure 4D. R_e was independent of the cycle number because the galvanostatic cycling was conducted within a stable potential region of the aqueous electrolyte, which was supported by an absence of the current tail vicinity of the lower and upper potential limits of the CVs. Changes in R_{film} were hardly detectable with increased cycling, indicating that the amorphous region of V/Fe PBA surrounding the crystalline region was retained during the charge/discharge process. The most prominent increase in resistance was observed in the charge-transfer characteristics (R_{ct}). The R_{ct} of the V/Fe PBA cathodes sharply increased during the early cycles and hardly varied over the remainder of the cycles. Interestingly, the variation tendency of R_{ct} was similar to the variation in specific capacity in that most of the changes, i.e., reduction in capacity and increase in the charge transfer resistance, were observed in the early cycles and subsequently saturated.

The dissolution behavior of the transition metal ions during cycling was monitored by inductively coupled plasma optical emission spectrometry (ICP-OES), as shown in Figure

4E. The V and Fe ions gradually dissolved upon cycling, and the mass concentration of the dissolved V ions was more prominent than that of the Fe ions, even considering that the ratio of V to Fe ion concentration in V/Fe PBA is 3/2. Notably, the fractions of dissolved V and Fe ions relative to the total mass of ions present in the electrodes were less than ~ 1.5 and ~ 0.6 % at the end of cycling (250th cycle), respectively; therefore, the dissolution of these ions did not cause the changes in the XRD patterns and SEM images during cycling. The dissolved mass of these ions increased rapidly from the start of cycling, and the increase in these dissolved ions was mitigated or negligible after prolonged cycling. Therefore, the decay of the delivered capacity is closely related to the accumulation of the charge-transfer resistance, and the dissolution of the V and Fe ions, mostly occurring at the vanadium sites, caused the increase in R_{ct}.

Conclusion

V/Fe PBAs were synthesized by a co-precipitation method, and their electrochemical performance as a cathode for ARBs was investigated. Optimizing the acidity and molar ratios of the precursor solutions during synthesis was vital to induce a high degree of crystallinity and good performance. The V/Fe PBAs delivered a high discharge capacity of ~ 90 mAhg^{-1} under a current density of 110 mAg^{-1} (~ 1.2 C) while exhibiting high recycling efficiency, which was greatly enhanced compared to other PBA series, including Cu/Fe and Ni/Fe PBAs. The analysis of the changes in electronic structure during the charge process using *ex-situ* XANES revealed that the improved charge storage capacity of the V/Fe PBAs could be traced to the multiple electron-involved redox reactions occurring with V and Fe ions. Furthermore, due to the three-dimensional network of hydrogen bonding and the large lattice parameter, the V/Fe PBAs exhibited facile diffusion kinetics and low activation energy for the charge-transfer process, leading to a high rate capability.

Monitoring the microstructural and crystallographic changes during cycling confirmed that the integrity and overall morphology of the V/Fe PBA-based electrode were well preserved during repeated insertion/extraction of the guest ions. During cycling, almost all of the decrease in capacity occurred during the early stage of cycling as a result of the dissolution of metal ions (mostly V ions) which led to an increase in the charge-transfer resistance. However, considering the long-term

usage of ARBs, the V/Fe PBAs showed a highly stable cycling performance after saturation of the degree of dissolution and Rct. Suppressing the dissolution and enhancing the reaction kinetics of V ions by introducing a mixed conductor coating layer would appear to be the most effective strategies for further improving the electrochemical performance of V/Fe PBAs, although V ions still contribute to the total energy storage process.
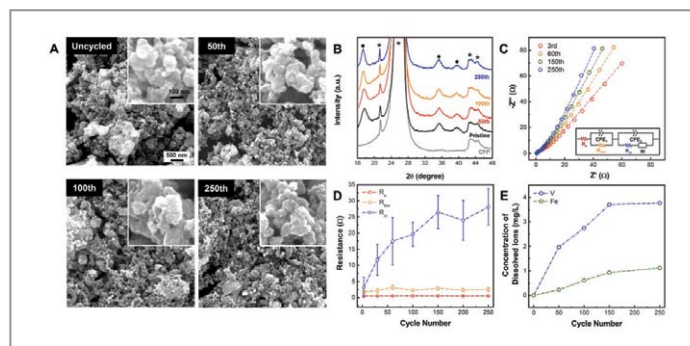
Our investigations confirm that V/Fe PBA is the most attractive candidate cathode material for ARBs because these cathodes can be easily mass produced in a cost effective and simple process, and their electrochemical performance is sufficient to meet the requirements of ARBs for large-scale energy storage systems.

Note

References

[1] Dunn B, Kamath H, Tarascon JM. *Science* 2011; 334: 928.

[2] Tarascon JM, Armand M. *Science* 2001; 414: 359.

[3] Lee KT, Ramesh TN, Nan F, Botton G, Nazar LF. *Chem. Mater.* 2011; 23: 3593.

[4] Kühnel RS, Böckenfeld N, Passerini S, Winter M, Balducci A. *Electrochim. Acta.* 2011; 56: 4092.

[5] Li W, Dahn JR, Wainwright DS. *Science* 1994; 264: 1115.

[6] Tang W, Zhu Y, Hou Y, Liu L, Wu Y, Loh KP, Zhang H, Zhu K. *Energy Environ. Sci.* 2013; 6: 2093.

[7] Kim H, Hong J, Park KY, Kim H, Kim SW, Kang K. *Chem. Rev.* 2014; 114: 11788.

[8] Lu Y, Wang L, Cheng J, Goodenough JB. Chem. *Commun.* 2012; 48: 6544.

[9] You Y, Wu XL, Yin YX, Guo YG. *Energy Environ. Sci.* 2014; 7: 1643.

[10] Pasta M, Wessells CD, Liu N, Nelson J, McDowell MT, Huggins RA, Toney MF, Cui Y. *Nat. Commun.* 2014; 5: 3007.

[11] Wang RY, Wessells CD, Huggins RA, Cui Y. *Nano Lett.* 2013; 13: 5748.

Bio / Medical

Materials / Systems

Energy / Environment

Research Highlights

KIST News

VKIST

Up Close

Interview

[12] Wessells CD, Peddada SV, Huggins RA, Cui Y. *Nano Lett.* 2011; 11: 5421.

[13] Liu S, Pan GL, Li GR, Gao XP. *J. Mater. Chem. A.* 2015; 3: 959.

[14] Wu X, Cao Y, Ai X, Qian J, Yang H. *Electrochem. Commun.* 2013; 31: 145.

[15] Wessells CD, McDowell MT, Peddada SV, Pasta M, Huggins RA, Cui Y. *ACS Nano* 2012; 6: 1688.

[16] Sinha NN, Ragupathy P, Vasan HN, Munichandraiah N. *Int. J. Electrochem. Soc.* 2008; 3: 691.

[17] Liu Y, Qiao Y, Zhang W, Wu H, Li Z, Shen Y, Yuan L, Hu X, Dai X, Huang Y. *Nano Energy* 2014; 5: 97.

[18] Minakshi M, Singh P, Thurgate S, Prince K. *Electrochem. Solid State Lett.* 2006; 9: A471.

[19] Shaojun D, Fengbin L. *J. Electroanal. Chem.* 1986; 210: 31.

[20] Ohkoshi SI, Nakagawa K, Tomono K, Imoto K, Tsunobuchi Y, Tokoro H. *J. Am. Chem. Soc.* 2010; 132: 6620.

[21] Corrias A, Ennas G, Mountjoy G, Paschina G. *Phys. Chem. Chem. Phys.* 2000; 2: 1045.

[22] Westre TE, Kennepohl P, DeWitt JG, Hedman B, Hodgson KO, Solomon EI. *J. Am. Chem. Soc.* 1997; 119: 6297.

[23] Gross S, Bauer M. *Adv. Funct. Mater.* 2010; 20: 4026.

[24] Chen JL, Chang CC, Ho YK, Chen CL, Hsu CC, Jang WL, Wei DH, Dong CL, Pao CW, Lee JF, Chen JM, Guo J, Wu MK. *Phys. Chem. Chem. Phys.* 2015; 17: 3482.

[25] Liu Q, Li ZF, Liu Y, Zhang H, Ren Y, Sun CJ, Lu W, Zhou Y, Stanciu L, Stach EA, Xie J. *Nat. Commun.* 2015; 6: 6127.

[26] Wong J, Lytle FW, Messmer RP, Maylotte DH. *Phys. Rev. B.* 1984; 30: 5596.

Arsenic(V) Removal Using an Amine-Doped Acrylic Ion Exchange Fiber

Sang Hyup LEE

Principal Researcher
Center for Water Resource Cycle Research
Green City Technology Institute

yisanghyup@kist.re.kr

Chang Gu LEE

Rice University

leechanggu@gmail.com

Introduction

Ion exchange fiber is a new type of ion exchange material and has several advantages over conventional ion exchange resins. The fiber has high adsorption/desorption rates and a better uptake capacity than ion exchange resins because of the short transit distance for ions and the number of functional groups present along the fiber. Furthermore, the compact configuration of the treatment module is easy to fabricate and relatively free from head loss [1, 2]. Several studies have reported the synthesis of ion exchange fibers for the removal of arsenic from aqueous solutions using various polymers. However, research on the development of more affordable synthetic methods using cost-effective and easily obtained commercial fibers is still necessary to make water treatment more broadly accessible.

Arsenic (As(V)) is a carcinogen, and chronic exposure to contaminated drinking water increases the occurrences of skin, lung, bladder, and kidney cancers [3]. Because of the high toxicity of arsenic, the United States Environmental Protection Agency (US EPA) and World Health Organization (WHO) recommend a maximum contaminant level of 10 µg/L for arsenic in drinking water. The US EPA has announced several best available technologies (BATs) for arsenic removal: ion exchange, activated alumina, reverse osmosis, modified coagulation/filtration, modified lime softening, electrodialysis reversal, and oxidation/filtration [4]. Among these technologies, the ion exchange process is a particularly advantageous one since it does not generate a large amount of waste and is affordable as the resins can be regenerated.

In this study, we focused on the synthesis of amine-doped acrylic ion exchange fibers and their application to the removal of As(V) from aqueous solutions. The synthesis of the fibers was confirmed using Fourier-transform infrared (FT-IR) spectroscopy. As(V) removal experiments were performed to examine the effects of solution pH, initial arsenic concentration, and regeneration cycles. The adsorption capacity was compared to that of PAN-based commercial anion exchange fiber, Fiban AK-22 (Institute of Physical Organic Chemistry), and titanium- and iron-based adsorbents that are commonly used to remove As(V) from water in
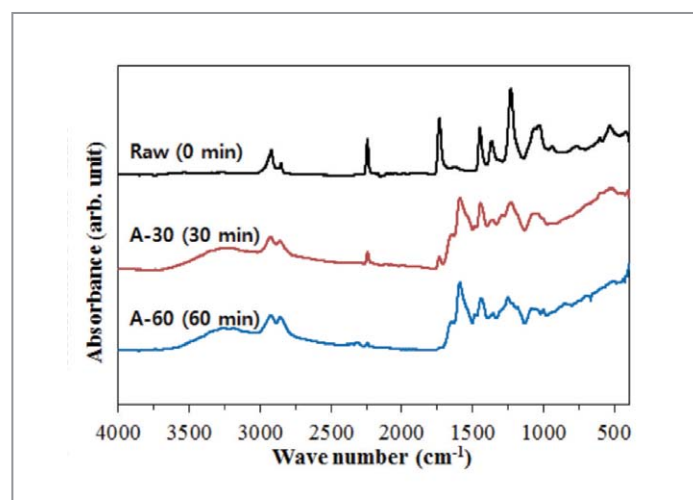
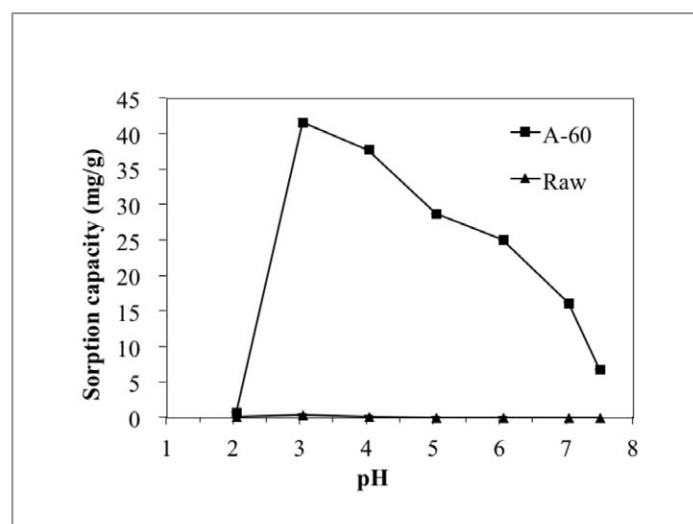order to benchmark the performance of our novel ion exchange fiber.

Synthesis and characterization of amine-doped acrylic ion exchange fiber
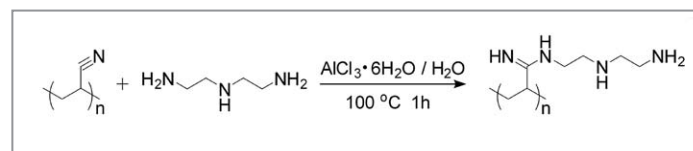
Figure 1 Synthesis procedure for the amine-doped acrylic ion exchange fiber.

Figure 2 FT-IR spectra of the synthesized fibers after different reaction times.

Figure 3 Effect of solution pH on As(V) removal by the synthesized fibers (adsorbent dosage = 0.2 g/L, initial concentration = 10 mg/L, contact time = 2 h, solution pH = 2.05 – 7.51).

Table 1 Physicochemical properties of the fibers used in this study.

Properties	A-60
Physical form	staple
Color	gold yellow
Diameter (μm)	37 - 54
Ion exchange capacity (meq/g)	7.5
Functional groups	=NH, -NH2

A schematic diagram of the synthesis procedure for the amine doped acrylic ion exchange fiber is shown in Figure 1. Acrylic fiber (consisting of about 90% acrylonitrile) was purchased from Taekwang Industrial Co., Ltd., Korea. This fiber was extracted with ethanol to remove impurities and dried at 60º C under vacuum for 18 h. Acrylic fibers (6 g), diethylenetriamine (500 g), and distilled water (50 mL) containing AlCl$_3$·6H$_2$O (10 g) were placed in a three-neck round-bottomed flask and stirred at 100º C for 60 min. The modified fibers were washed with 0.1 M HCl, 0.1 M NaOH, and distilled water in sequence.

The physicochemical properties of the fibers are presented in Table 1. The staple form of the acrylic fiber was used as the raw material, and the color of the fiber changed from white to a gold yellow after reaction with diethylenetriamine for 60 min. The reaction was confirmed by the FT-IR spectra (Figure 2). The absorption peaks of the nitrile group (C≡N, 2242 cm-1) decreased with increasing reaction time and disappeared after 60 min of reaction (A-60). New peaks for amidine (N-C=N, 1640 cm-1) and strong broad bands for the amine groups (NH2, 3500-2000 cm-1) were visible after the reaction [5, 6]. The total ion exchange capacity of A-60 for amine sites, which was calculated using the back titration method, was 7.5 meq/g. This value falls within the range of reported ion exchange capacity for commercial products such as Fiban K-4 ion exchange fiber (4 - 5 meq/g) and poly(acrylo-amidino diethylenediamine) chelating fiber (11.4 meq/g) [5, 7].

Effect of solution pH on As(V) removal

The effects of the solution pH on As(V) removal by raw material and A-60 fibers are shown in Figure 3. As(V) removal by A-60 was clearly affected by the solution pH. These results are related to the speciation of As(V). The chemical speciation of As(V) based on the solution pH was calculated using a computer program for geochemical modeling (arsenic concentration = 10 mg/L, temperature = 25º C, calculation

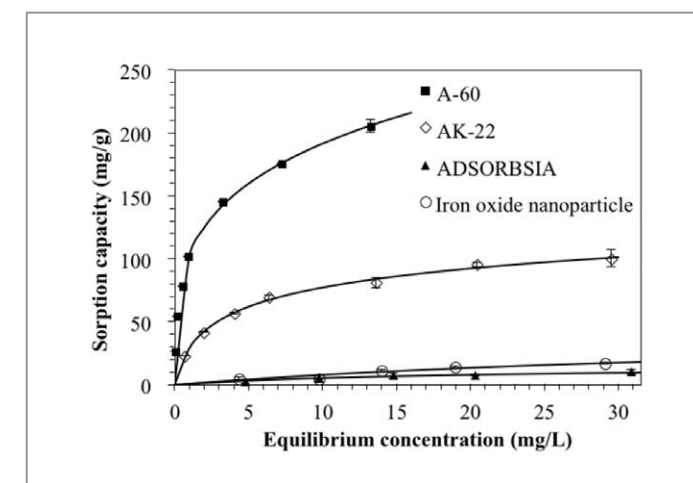performed using the Visual MINTEQ 3.0 code):

(1) $H_3AsO_{4(aq)} \leftrightarrow H_2AsO_4^- + H^+$ $pK_{a1} = 2.28$

(2) $H_2AsO_4^- \leftrightarrow HAsO_4^{2-} + H^+$ $pK_{a2} = 6.97$

At low solution pH, the amine groups on the adsorbent surface are protonated to form –NH^{3+}, and the surface of the adsorbent is more positively charged [8, 9]. Therefore, the maximum sorption capacity of A-60 was at pH 3.04, when anionic species such as H$_2$AsO$_4$. predominate. The sorption of As(V) at pH 2.05 was negligible because the nonionic species are dominant at solution pH values lower than 2.28, as indicated by eq. (1).

Effect of equilibrium concentration on As(V) removal

Equilibrium studies were carried out at various initial arsenic concentrations using fibrous ion exchangers (A-60 and AK-22) and adsorbents (ADSORBSIA™ and iron oxide nanoparticle) that are well known for As(V) removal from water. As shown in Figure 4, the sorption capacity of A-60 increased rapidly compared to AK-22, and the difference in the sorption capacity between the two adsorbents also increased based on the initial concentration. At the highest initial concentration of 50 mg/L, the sorption capacity of A-60 (205.32 ± 3.57 mg/g) was two times larger than that of the AK-22 (100.35 ± 8.80 mg/g), while the sorption capacity of ADSORBSIATM (10.70 ± 0.51 mg/g) and iron oxide nanoparticles (22.91 ± 0.49 mg/g) was about nine times smaller than that of the fibrous ion exchanger

Figure 4 Effect of equilibrium concentration on As(V) removal by fibrous ion exchangers and alternative adsorbents tested in this study (adsorbent dosage = 0.2 g/L, initial concentration = 5 - 50 mg/L, contact time = 2 h, solution pH = 3.04).

at the same initial concentration (50 mg/L) in our experimental conditions. The adsorption capacity of various materials are presented in Table 2 along with the tested conditions. Based on these data, the A-60 synthesized in this study exhibits superior adsorption capacity as compared to the tested commercial materials or values discussed in published literature.

Regeneration studies

Several chemicals and their combinations, such as HCl, NaOH, and NaCl, were tested for the regeneration of fibrous ion exchange materials [7, 10-12]. Acids and bases were used to complete the regeneration of the fiber in this study. The fiber

Table 2 Comparison of the adsorption capacity (qe) of different fibrous ion exchangers and adsorbents for As(V) adsorption.

Adsorbents	Conditions	q$_e$ (mg/g)	Referenc
RPFA-I	Initial concentration = 5 mg/L; pH = 7.00; contact time = 12 h	9.19*	[15]
FIBAN-As	Initial concentration = 500 mg/L; pH = 7.70; contact time = 24 h	75.67*	[16]
QDMAEMA-g-PE/PP	Initial concentration = 500 mg/L; pH = 7.00; contact time = 240 min	82.66	[12]
Cellulose-g-PDMAEMA	Initial concentration = 8.9 mg/L; pH < 10; contact time = 1 min	27.93*	[17]
FIBAN AK-22		100.35 ± 8.80	This study
Poly(acrylo-amidino diethylenediamine) (A-60)	Initial concentration = 50 mg/L;	205.32 ± 3.57	This study
ADSORBSIA™	pH = 3.04; contact time = 120 min	10.70 ± 0.51	This study
Iron oxide nanoparticle		22.91 ± 0.49	This study

Figure 5 Removal efficiency of As(V) onto A-60 during 9 regeneration cycles (adsorbent dosage = 0.2 g/L, initial concentration = 10 mg/L, contact time = 2 h, solution pH = 3.04).

can be effectively regenerated by rinsing the adsorbent with 0.1 N HCl, 0.1 N NaOH, and ultra-pure water in sequence. The removal efficiency of the A-60 fibers remained above 83% of the initial value during nine regeneration cycles (Figure 5). The decrease in removal efficiency was related to fiber degradation via the regeneration chemicals [13,14]. Nonetheless, the results indicate that A-60 fibers have an excellent reusability for As(V) removal, and the fibers can be used as an affordable ion exchange technology with the use of regeneration.

Conclusions

The removal of As(V) from aqueous solutions was investigated using a synthesized ion exchange fiber. The amine doping reaction with an acrylic fiber using DETA was complete within 60 min using a AlCl$_3$·6H$_2$O catalyst at 100º C. The As(V) removal efficiency of the fiber was affected by the solution pH, and the maximum sorption capacity for A-60 was found at pH 3.04. A-60 has a high adsorption capacity compared to reported values for other fibers, and the removal efficiency of the fiber was largely maintained over nine regeneration cycles. These results demonstrate that amine-doped acrylic ion exchange fibers can be used as a BAT for arsenic removal from aqueous solutions.

Note

This article and images are drawn from "Arsenic(V) removal using an amine-doped acrylic ion exchange fiber: Kinetic, equilibrium, and regeneration studies" in *Journal of Hazardous Materials*, 2017, Vol. 325, pp. 223~229.

References

[1] Ko YG, Chun YJ, Kim CH, Choi US. *J. Hazard Mater*. 2011; 194: 92–99.

[2] Dai L, Cui L, Zhou D, Huang J, Yuan S. *J. Taiwan Inst. Chem. Eng*. 2015; 54: 170–177.

[3] An B, Kim H, Park C, Lee SH, Choi JW. *J. Hazard Mater*. 2015; 289: 54-62.

[4] USEPA. Arsenic and clarifications to compliance and new source contaminants monitoring. 2001.

[5] Strickland T, Fisher L, Korleski C. Guidelines for arsenic removal treatment for small public drinking water systems. 2010.

[6] Shin DH, Ko YG, Choi US, Kim WN. *Polym. Adv. Technol*. 2005; 15: 459–466.

[7] Greenleaf JE, Lin J, Sengupta AK. *Environ. Prog. Sustain. Energy* 2006; 25: 300-311.

[8] Yu X, Tong S, Ge M, Wu L, Zuoa J, Cao C. *Carbohydr. Polym*. 2013; 92: 380–387.

[9] Menguc GS. *Tekst Konfeksiyon* 2016; 26: 40–47.

[10] Awual MR, Urata S, Jyo A, Tamada M, Katakai A. *Water Re*s. 2008; 42: 689–696.

[11] Awual MR, Shenashen MA, Yaita T, Shiwaku H, Jyo A. *Water Res*. 2012; 46: 5541–5550.

[12] Kavaklı C, Kavaklı PA, Turan BD, Hamurcu A, Güven O. *Radiat. Phys. Chem*. 2014; 102: 84–95.

[13] Dai L, Cui L, Zhou D, Huang J, Yuan S. *J. Taiwan Inst. Chem. Eng*. 2015; 54: 170–177.

[14] Bhaumik M, Maity A, Srinivasu VV, Onyango MS. *Chem. Eng. J*. 2012; 181-182: 323–333.

[15] Zhang X, Jiang K, Tian Z, Huang W, Zhao L. *J. Appl. Polym. Sci*. 2008; 110: 3934–3940.

[16] Vatutsina OM, Soldatov VS, Sokolova VI, Johann J, Bissen M, Weissenbacher A. *React. Funct. Polym*. 2007; 67: 184–201.

[17] Tian Y, Wu M, Liu R, Wang D, Lin X, Liu W, Ma L, Li Y, Huang Y. *J. Hazard Mater*. 2011; 185: 93–100.

High-force display capability and wide workspace with a novel haptic interface

Yong Hwan OH

Principal Researcher
Center for Robotics Research
Robotics and Media Institute

oyh@kist.re.kr

Abstract

We present a novel haptic interface, named VirtuaPower, having a high-force display capability (FDC) and a wide workspace with a six-degree-of-freedom position measurement and FDC. The overall mechanism of VirtuaPower is designed based on a parallel pair of five-bar mechanisms supporting the end-platform. This novel mechanism enhances the high-FDC and overcomes the problem of small-size workspace, which are the pros and cons of parallel mechanisms, respectively. First, we present the conceptual design and prototype of VirtuaPower. Then, we formulate the forward kinematic and the constraint and space Jacobian. Using these formulations, we analyze two types of workspaces and FDC. In both analyses, VirtuaPower shows remarkable performance, especially in terms of its FDC, compared to other haptic interfaces having an equivalent size. In addition, we validate the static, step, and frequency responses of the force-display performance by performing experiments using the test bench of fixed-end setup with a six-dimensional force/torque sensor. Finally, we evaluate the suitability of VirtuaPower as a haptic interface by realizing two types of virtual sphere walls and a virtual reality environment.
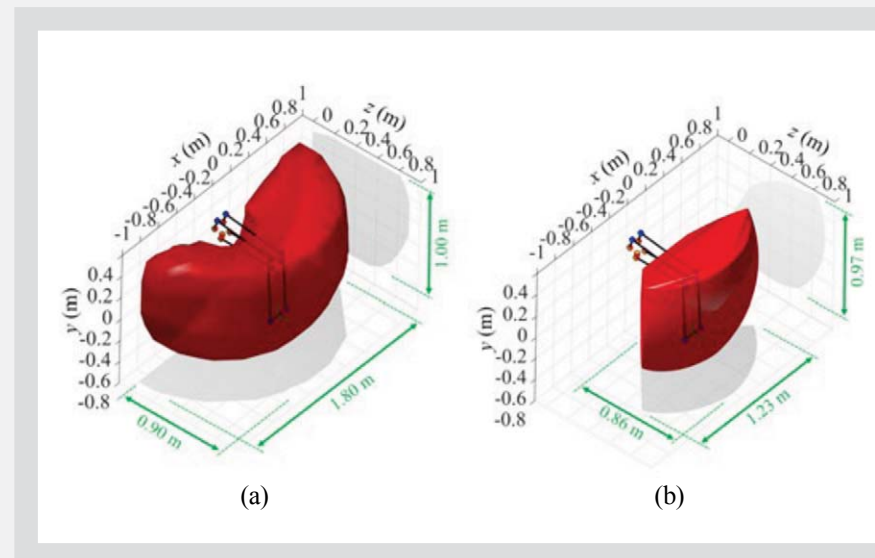
VirtuaPower
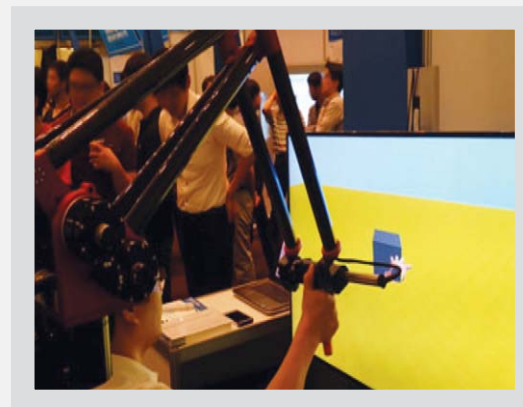
Evaluation of virtual reality environment

High force display capability and wide workspace

The mechanism is designed based on a double support-chain mechanism. A pair of supporting chains is set up in parallel at the base-platform. The supporting chains consist of five-bar mechanisms, which are used in many applications. The overall structure can be rotated on the horizontal plane by rotating the actuator installed at the bottom of the base-platform. VirtuaPower can provide 6-DOF position measurement and force display. In addition, if we set up the two chains to reduce geometric restrictions and collisions, a wide workspace over the entire system size of the mechanism can be expected. As a result, the double-support chain type meets our requirement, which is for a small system size with a high-FDC and wide workspace.

Workspace analysis of VirtuaPower. (a) Reachable workspace. (b) Constant orientation workspace.
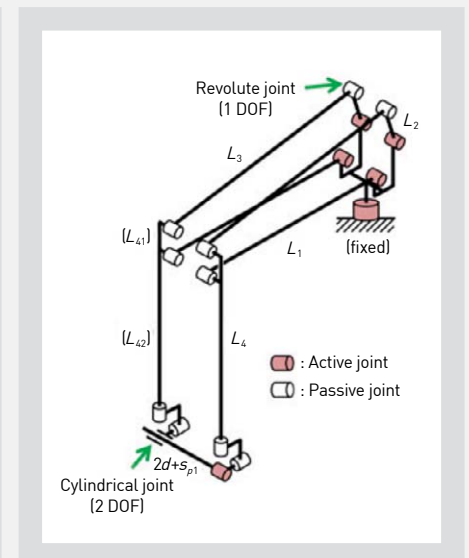
Schematics. The number of linkages and joints is 16 and 17, respectively.

Stellera chamaejasme and its constituents induce cutaneous wound healing and antiinflammatory activities

Myung Suk KIM, Hee Ju LEE, Ahmad RANDY, Ji Ho YUN, Sang Rok OH, Chu Won NHO

cwnho@kist.re.kr

Stellera chamaejasme L. (Thymelaeaceae) is a perennial herb that is widely used in traditional Chinese medicine to treat tumours, tuberculosis and psoriasis. *S. chamaejasme* extract (SCE) possesses anti-inflammatory, analgesic and wound healing activities; however, the effect of *S. chamaejasme* and its active compounds on cutaneous wound healing has not been investigated. We assessed full thickness wounds of Sprague-Dawley (SD) rats and topically applied SCE for 2 weeks. *In vitro* studies were performed using HaCaT keratinocytes, Hs68 dermal fibroblasts and RAW 264.7 macrophages to determine cell viability (MTT assay), cell migration, collagen expression, nitric oxide (NO) production, prostaglandin E2 (PGE2) production, inflammatory cytokine expression and β-catenin activation. *In vivo*, wound size was reduced and epithelisation was improved in SCE-treated SD rats. *In vitro*, SCE and its active compounds induced keratinocyte migration by regulating the β-catenin, extracellular signal-regulated kinase and Akt signalling pathways. Furthermore, SCE and its active compounds increased mRNA expression of type I and III collagen in Hs68 fibroblasts. SCE and chamechromone inhibited NO and PGE2 release and mRNA expression of inflammatory mediators in RAW 264.7 macrophages. SCE enhances the motility of HaCaT keratinocytes and improves cutaneous wound healing in SD rats.

Anisotropically organized three-dimensional culture platform for reconstruction of a hippocampal neural network

So Hyun KIM, Sun Kyoung IM, Soo Jin OH, So Hyeon JEONG, Eui Sung YOON, C. Justin LEE, Nak Won CHOI, Eun Mi HUR

ehur@kist.re.kr

In native tissues, cellular and acellular components are anisotropically organized and often aligned in specific directions, providing structural and mechanical properties for actuating biological functions. Thus, engineering alignment not only allows for emulation of native tissue structures but might also enable implementation of specific functionalities. However, achieving desired alignment is challenging, especially in three-dimensional constructs. By exploiting the elastomeric property of polydimethylsiloxane and fibrillogenesis kinetics of collagen, here we introduce a simple yet effective method to assemble and align fibrous structures in a multi-modular three-dimensional conglomerate. Applying this method, we have reconstructed the CA3–CA1 hippocampal neural circuit three-dimensionally in a monolithic gel, in which CA3 neurons extend parallel axons to and synapse with CA1 neurons. Furthermore, we show that alignment of the fibrous scaffold facilitates the establishment of functional connectivity. This method can be applied for reconstructing other neural circuits.

Transparent high-performance SiOxNy/SiOx barrier films for organic photovoltaic cells with high durability

Ju Won LIM, Chang Kyu JIN, Keun Yong LIM, Yun Jae LEE, Sung Ryong KIM, Byung Il CHOI, Tae Whan KIM, Dong Ha KIM, Do Kyung HWANG, Won Kook CHOI

wkchoi@kist.re.kr

The science and technology of organic electronics have made consistent progress. However, the long-term stability of organic devices is a critical issue that remains to be resolved. Encapsulation is a straightforward and practical means to protect organic materials from oxygen or moisture and thus improve air stability. Here, we report a high-performance flexible inorganic SiN_x/SiO_xN_y hybrid barrier film for application in organic solar cells (OSCs). This hybrid barrier film shows average transmittance of 85.5% and a water-vapor transmission rate of 7.1×10^{-5} g m^{-2} day^{-1}. In OSCs comprising poly[4,8-bis[(2-ethylhexyl)oxy]benzo[1,2-b:4,5-bA]dithiophene-2,6-diyl][3-fluoro-2-[(2-ethylhexyl)carbonyl] thieno[3,4-b]-thiophenediyl] (PTB7) and [6,6]-phenyl-C$_{70}$-butyric acid methyl ester (PC70BM), which were encapsulated by the SiN_x/SiO_xN_y hybrid barrier film, the power-conversion efficiency remained above 86% of the initial value even after 2000 h of storage in air, which is comparable to that obtained for a device encapsulated by a glass lid.

Large spin accumulation and crystallographic dependence of spin transport in single crystal gallium nitride nanowires

Tae Eon PARK, Youn Ho PARK, Jong Min LEE, Sung Wook KIM, Hee Gyum PARK, Byoung Chul MIN, Hyung jun KIM, Hyun Cheol KOO, Heon Jin CHOI, Suk Hee HAN, Mark JOHNSON, Joon Yeon CHANG

presto@kist.re.kr

Semiconductor spintronics is an alternative to conventional electronics that offers devices with high performance, low power and multiple functionality. Although a large number of devices with mesoscopic dimensions have been successfully demonstrated at low temperatures for decades, room-temperature operation still needs to go further. Here we study spin injection in single-crystal gallium nitride nanowires and report robust spin accumulation at room temperature with enhanced spin injection polarization of 9%. A large Overhauser coupling between the electron spin accumulation and the lattice nuclei is observed. Finally, our single-crystal gallium nitride samples have a trigonal cross-section defined by the (001), (11$\bar{2}$) and ($\bar{1}$1$\bar{2}$) planes. Using the Hanle effect, we show that the spin accumulation is significantly different for injection across the (001) and (11$\bar{2}$) (or (11$\bar{2}$)) planes. This provides a technique for increasing room temperature spin injection in mesoscopic systems.

Effect of molecular orientation of donor polymers on charge generation and photovoltaic properties in bulk Heterojunction all-polymer solar cells

Jea Woong JO, Jae Woong JUNG, Hyung Ju AHN, Min Jae KO, Alex K.-Y. JEN, Hae Jung SON

hjson@kist.re.kr

All-polymer solar cells (all-PSCs) utilizing p-type polymers as electron-donors and n-typepolymers as electron-acceptors have attracted a great deal of attention, and their efficiencies have been improved considerably. Here, five polymer donors with different molecular orientations are synthesized by random copolymerization of 5-fluoro-2,1,3-benzothiadiazole with different relative amounts of 2,2′-bithiophene (2T) and dithieno[3,2-b;2′,3′-d]thiophene (DTT). Solar cells are prepared by blending the polymer donors with a naphthalene diimide-based polymer acceptor (PNDI) or a [6,6]-phenyl C71-butyric acid methyl ester (PC71BM) acceptor and their morphologies and crystallinity as well as optoelectronic, charge-transport and photovoltaic properties are studied. Interestingly, charge generation in the solar cells is found to show higher dependence on the crystal orientation of the donor polymer for the PNDI-based all-PSCs than for the conventional PC71BM-based PSCs. As the population of face-on-oriented crystallites of the donor increased in PNDI-based PSC, the short-circuit current density (JSC) and external quantum efficiency of the devices are found to significantly improve. Consequently, device efficiency was enhanced in all-PSC from 3.11% to 6.01%. The study reveals that producing the same crystal orientation between the polymer donor and acceptor (face-on/face-on) is important in all-PSCs because they provide efficient charge transfer at the donor/acceptor interface.

Elimination of microcystin-LR and residual Mn species using permanganate and powdered activated carbon: oxidation products and pathways

Bo Young JEONG, Min Seok OH, Hyun Mee PARK, Chan Hyuk PARK, Eun Ju KIM, Seok Won HONG

swhong@kist.re.kr

The oxidation of microcystin-LR (MC-LR) in deionized water (DI) and river water using potassium permanganate (KMnO$_4$) at a neutral pH and at 23 ± 2 °C was investigated. These two aqueous systems (i.e., DI and river water) gave comparable second-order rate constants (289.9 and 285.5 M^{-1}s^{-1}(r^2 > 0.99), respectively), which confirmed the effectiveness of this oxidation process for the treatment of natural surface water. The presence of either humic or fulvic acid reduced the removal efficiency of MC-LR, with the latter exhibiting a greater inhibitory effect. Monitoring of MC-LR and residual Mn^{2+} levels with adding KMnO$_4$ (1 mg/L) and powdered activated carbon (PAC, 5-20 mg L^{-1}) before and during coagulation, respectively, revealed that 60 min of permanganate pre-oxidation followed by coagulant addition with PAC was the most effective approach for reducing both levels below limits stated by WHO guidelines. The MC-LR degradation products were the result of oxidation occurring at the diene and aromatic moieties of the Adda (3-amino-9-methoxy-2,6,8-trimethyl-10-phenyldeca-4,6-dienoic acid) side-chain, in addition to amine bond hydrolysis of the Mdha (N-methyldehydroalanine) moiety. Several toxic byproducts with an intact Adda chain were observed during the reaction, but completely disappeared after 60 min. This further supports the conclusion that sufficient contact time with permanganate (i.e., > 60 min) is essential to reducing the residual toxicity and maximizing the efficiency of MC-LR oxidation when treating raw water.

Method for differentiation of stem cells into vascular cells and the induction of angiogenesis using the same

Sang Heon KIM

skimbrc@kist.re.kr

A method for differentiating stem cells into vascular cells, including adhering the stem cells to a culture plate with a surface having a hydrophobic property or on which a growth factor is immobilized, and culturing the cells. The cultured stem cells later detach from the culture plate as their density increases to form a three-dimensional cell cluster and differentiate into vascular cells. The cell cluster can be used as a cell therapy agent for angiogenesis.
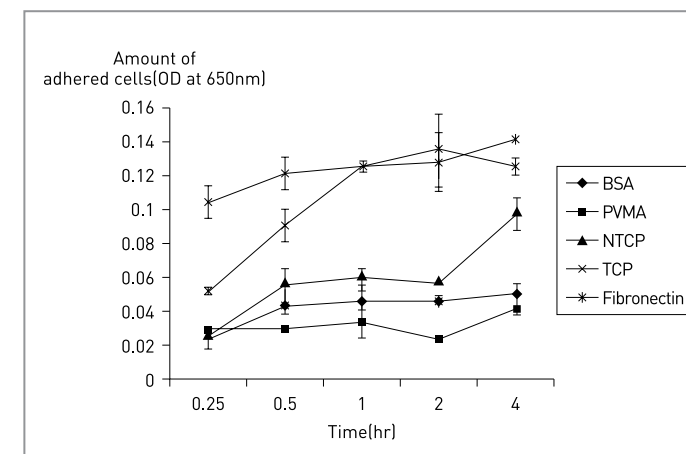
Exoskeleton mechanism for joint movement assistance

Kee Hoon KIM

khk@kist.re.kr

An exoskeleton mechanism according to the present disclosure includes: a fixed frame positioned to correspond to an upper physique; a rotatable frame positioned to correspond to a lower physique and coupled to the fixed frame by a hinge unit to be rotatable in the vertical direction; a support frame for supporting a terminal; a first motor mounted to the fixed frame and connected to the rotatable frame to drive the rotatable frame to rotate in the vertical direction; motors mounted to the rotatable frame and connected to the support frame to drive the support frame to rotate in the vertical direction and in the horizontal direction and rotate around an axis (roll axis) of the lower physique; links for connecting the first motor and the rotatable frame; and links for connecting the motors and the support frame.

Fig.1
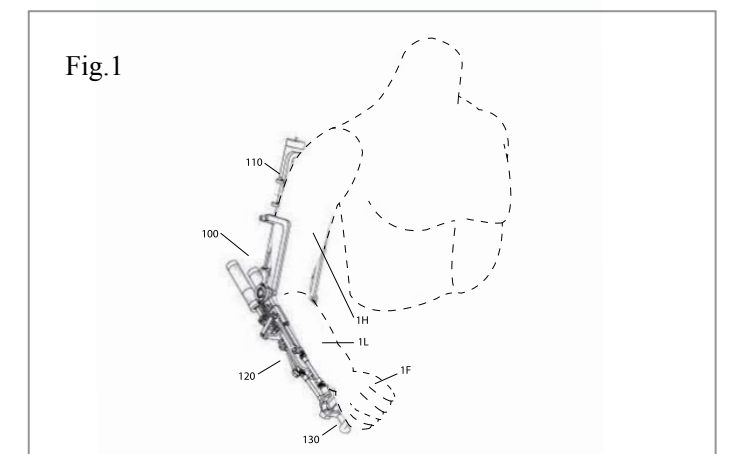
Method for producing hexagonal boron nitride film using borazine oligomer as a precursor

US 9562287 (2017.02.07) KR 1480817 (2015.01.05)

Myung Jong KIM

myung@kist.re.kr

Provided is a method for producing a high-quality boron nitride film grown by using a borazine oligomer as a precursor through a metal catalyst effect. The method solves the problems, such as control of a gaseous precursor and vapor pressure control, occurring in CVD (Chemical vapor deposition) according to the related art, and a high-quality hexagonal boron nitride film is obtained through a simple process at low cost. In addition, the hexagonal boron nitride film may be coated onto various structures and materials. Further, selective coating is allowed so as to carry out coating in a predetermined area and scale-up is also allowed. Therefore, the method may be useful for coating applications of composite materials and various materials.

Fig.2

Ex.1

Borazine oligomer → h-BN(White Graphene)
Nickel foil → Nickel foil

Ex.2

Borazine oligomer → Metal catalyst / Borazine oligomer → Metal catalyst / h-BN(White Graphene) → h-BN(White Graphene)
Silicon → Silicon → Silicon → Silicon

Universal nucleic acid aptamers for commonly binding to various types of microorganisms and method of producing the same

US 9551709 (2017.01.24) KR 1717767 (2017.03.13)

Byoung Chan KIM

bchankim@kist.re.kr

Provided are a single-stranded nucleic acid aptamer simultaneously and specifically binding to various types of microorganisms, and a method of manufacturing the nucleic acid aptamer. For example, provided are a probe that is capable of simultaneously detecting or diagnosing a variety of microorganisms, and a method of manufacturing an aptamer having characteristics of such a probe.

Fig.1

Cloning & Sequencing
RDL
Multiple Cell SELEX
Amplificaiton of DNA extracted
Repeat 3 round
E. coli
K. pneumoniae
S. epidermidis
B. subtilis
E. aerogenes
C. freundii
Extract bound DNA after 3round
Remove unbound DNA

Compound, preparing method thereof, and use thereof as inhibitors of histone demethylase

9650325 (2017.05.16) KR 1568724 (2015.11.06)

Hak Cheol KWON

hkwon@kist.re.kr

Provided are a novel compound, preparing method thereof, and use thereof as inhibitor of histone demethylase. The compound represented by Chemical Formula 1 has activity which inhibits histone demethylase and thus is capable of specifically and effectively inhibit activity of histone demethylase.
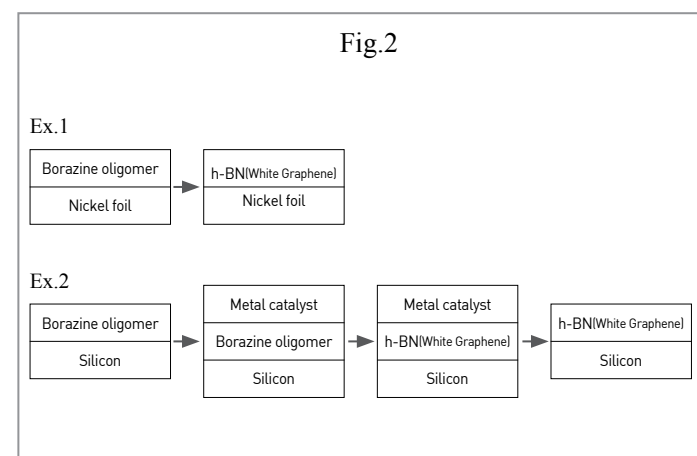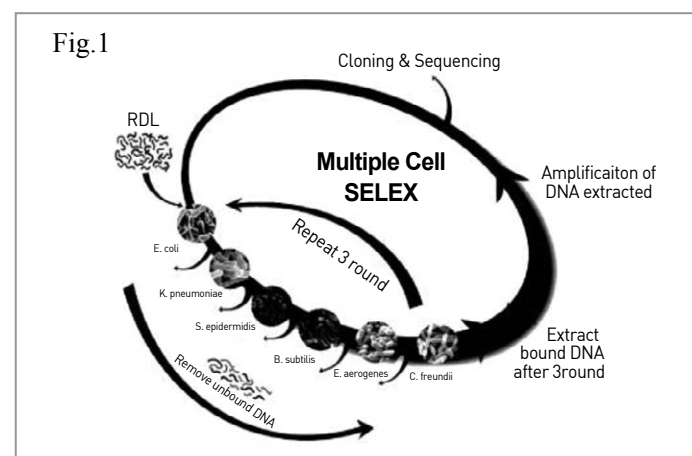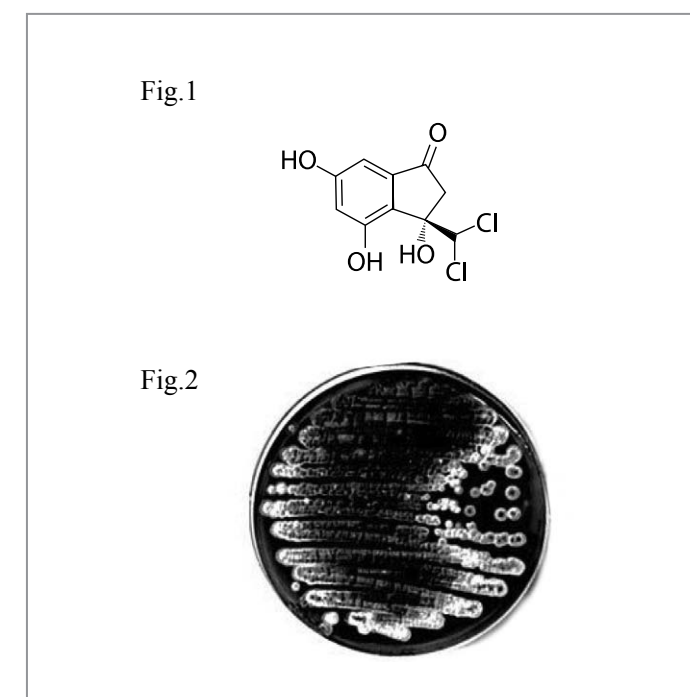

Fig.1

Fig.2

Exoskeleton mechanism for joint movement assistance

9644275 (2017.05.09)KR 1563585 (2015.10.21)

Chong Min KOO

koo@kist.re.kr

The present invention relates to a method for preparing graphene using a spontaneous process, and particularly, to a method for mass-producing high-quality graphene composed of a single layer or several layers by using lithium intercalation of a graphite electrode occurring during the process of charging a lithium ion battery and a lithium ion capacitor in the preparation of graphene to form a graphite intercalation compound, and performing exfoliation through a reaction with water (or alcohol).

Fig.5

e^-

e^-
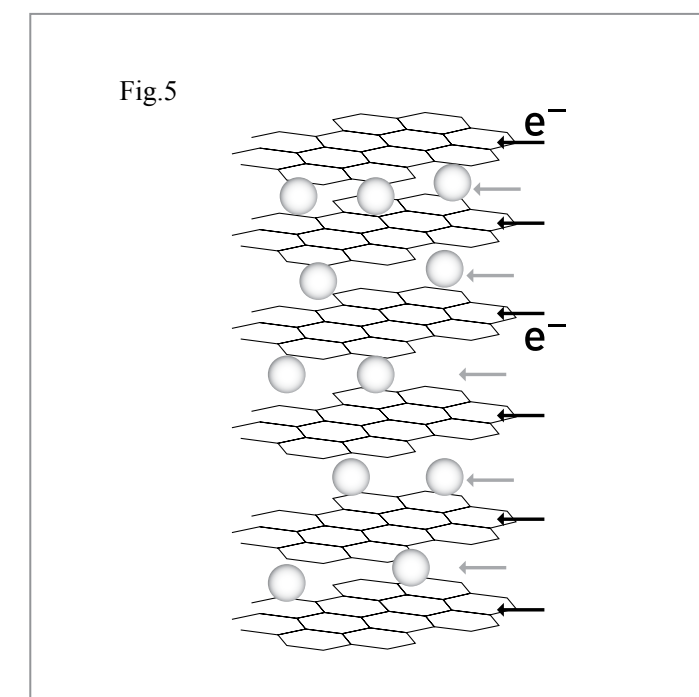
Electrochemical detoxification method of wood-based hydrolysate for producing biochemicals or biofuels

Young Soon UM

yum@kist.re.kr

Provided is a method for preparing a lignocellulosic biomass hydrolysate having toxicity reduced or removed and being used for fermentation by microorganisms, comprising the steps of: pretreating, hydrolyzing, and using an electrochemical detoxification method.

Fig.1

Carbazole derivatives acting on 5-HT7 receptor

Hyun Ah CHOO

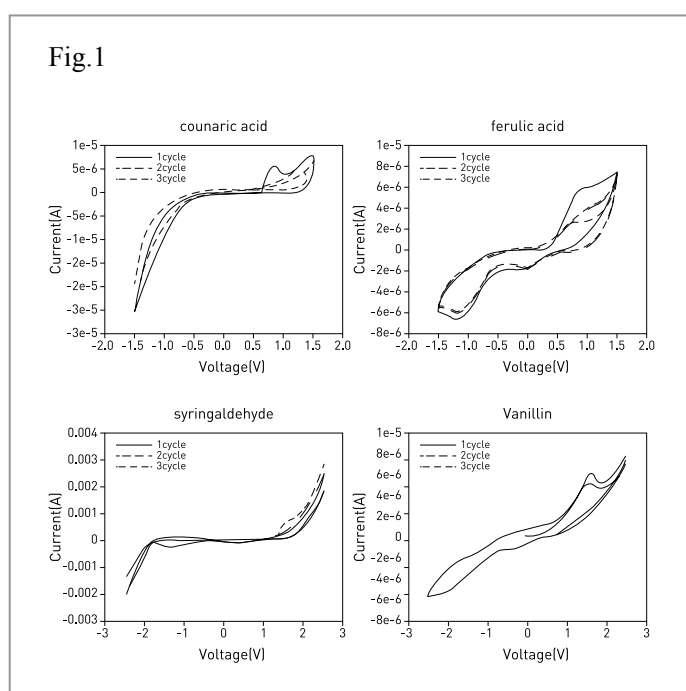hchoo@kist.re.kr

The present invention provides a carbazole derivative represented by Formula 1: wherein X is CH_2 or $C(O)$, Y is selected from $NR1R2$, piperidinyl groups in which two of the carbon atoms are substituted with R3 and R4, piperazinyl groups in which the nitrogen atom is substituted with R5, and morpholinyl groups, n is an integer from 2 to 5, R1 and R2, which may be identical or different, are each independently selected from C1-C6 alkyl, phenyl, and benzyl, with the proviso that R1 and R2 may be bonded together to form a ring, R3 and R4, which may be identical or different, are each independently selected from hydrogen, C1-C6 alkyl, phenyl, and benzyl, and R5 is selected from C1-C6 alkyl, C1-C4 alkylcarbonyl, phenyl substituted with C1-C4 alkyloxy, hydroxyphenyl, benzyl, and benzoisoxazol-3-yl; or a pharmaceutically acceptable salt thereof.
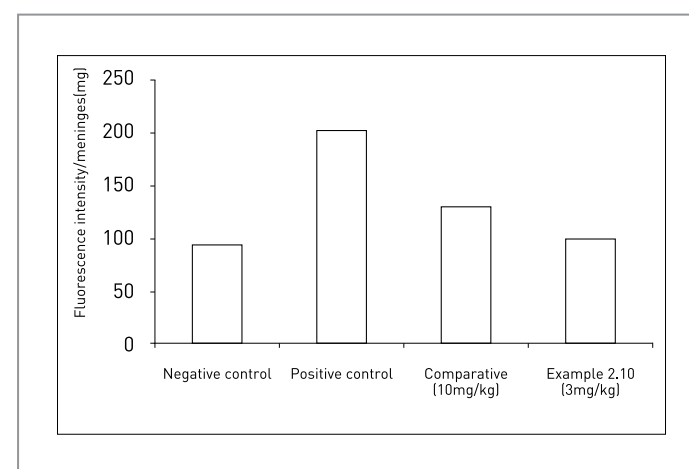
Peptide selectively binding to volatile organic compounds

Hyun Jung YI

hjungyi@kist.re.kr

Provided is a peptide selectively binding to a volatile organic compound, in which the peptide has excellent selectivity for the volatile organic compound and has stability at room temperature so as to effectively collect and detect or eliminate the volatile organic compound.

Fig.1
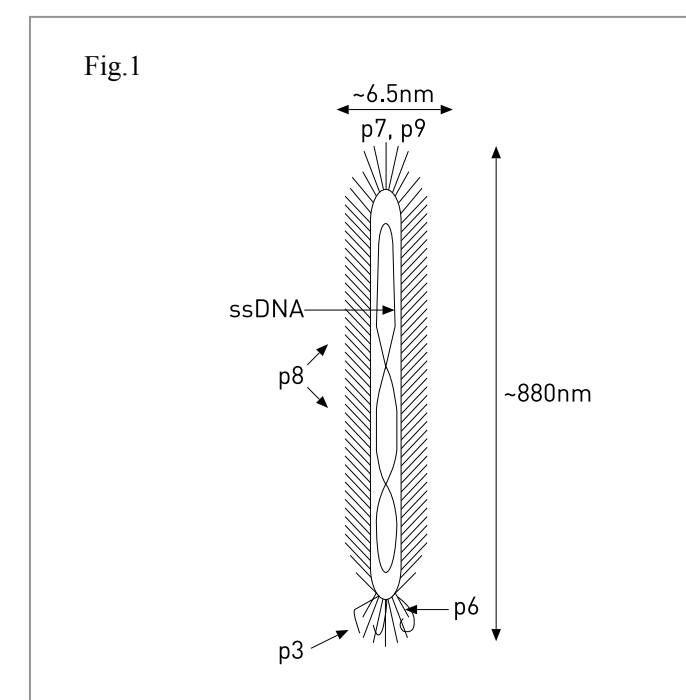
Science News

Detlef Zuehlke, the brains behind Industry 4.0, visits Korea to participate in the Global Innovation Forum

Boundaries in world markets are gradually collapsing. In an open market, it will no longer be possible to move forward by closely guarding innovative developments. The only way to succeed will be to pursue open collaboration and then implement results to make products available faster than competitors.

This is the advice of Dr. Detlef Zuehlke, the German originator of the "smart factory" concept and advocate of Industry 4.0, which refers to the fourth major transition to occur in modern manufacturing following downsizing in the 1970s, outsourcing in the 1990s, and the spread of automation in the 2000s. This fourth transition is occurring as a result of big data, more sophisticated analytics, more extensive human/machine interfaces and digital to physical transfer technologies (e.g., 3-D printing).

Dr. Zuehlke is leading efforts to shape the future of industry in Germany through his responsibilities as a director of the German Research Center for Artificial Intelligence (DFKI) GmbH and as executive chairman of the German SmartFactoryKL technology initiative. He visited Korea in September to participate in the Global Innovation Forum. We caught up with Dr. Zuehlke before the opening of the forum and asked him for his thoughts on various issues related to Industry 4.0.

The Fourth Industrial Revolution has recently emerged as a major issue in Korea. It has been significantly influenced by the concept of Industry 4.0. How do you think Korea is positioned?

In fact, Industry 4.0 is a game changer. The term appeared suddenly as a buzzword in 2011, but now is becoming a widely recognized reference to the future of global manufacturing. With the rapid development of relevant technologies, we will be better able to provide mass-produced goods of the type required by customers in a timely manner.

Korea has been a front-runner in adopting Industry 4.0. In 2010 and 2011, the SmartFactory research center and POSTECH conducted a joint project to develop technology related to smart production. That was a year before the term Industry 4.0 was even created. Ever since 2002 when efforts to prove the efficiency of smart production as a new paradigm started in Germany, I have been invited to Korea. This is a clear reflection of the high level of interest here in modernizing manufacturing.

How about recent trends in German industry? What measures and strategies are Germany finding helpful to ensure competitiveness in rapidly changing industries?

We need to first understand the industrial landscape in Germany. I can say that small and medium enterprises are the pillar of the German economy. When formulating policy, the government is careful to consider the needs of these enterprises, referred to as "hidden champions", as well as large enterprises. Programs for developing and supporting Industry 4.0 have been undertaken for years and are part of the federal government's national platform. Industry-driven activities are carried out through the "SmartFactory of Kaiserslautern" led by member companies and supported by activities of the government. We established the SmartFactory Initiative in Kaiserslautern in 2005 and have operated it since then with the participation of seven local partner companies and 49 members around the world, including companies such as IBM, Cisco, Siemens and Huawei. We set up networks, cooperate with each other and learn together. Our goal is to convert the Industry 4.0 paradigm into real working systems. While Germany is taking the lead, other nations, including Korea, have been quick to follow our example.

As an expert on smart factory technologies and artificial intelligence, what role do you think they'll play in the Fourth Industrial Revolution and how will they influence the future?

Smart factories in the future will depend heavily on internet technology and data. We have to find ways to convert enormous amounts of complex data into serviceable information. That is where artificial intelligence can help. Technology to analyze data, perform pattern recognition, and acquire deep learning-based knowledge will be important for unlocking the power of artificial intelligence.

You were invited to deliver the keynote address at the Global Innovation Forum held in Daejeon. What motivated you to accept, and what issues will you stress?

Whenever I visit Korea, it is wonderful to see evidence of the innovation that has led to Korea's economic success. It is always a pleasure to share in this spirit.

At the forum, I will be talking about the dramatic changes driven by digitalization in entire areas of industry as well as our routine lives. Today, customers can choose products on a computer screen and place orders instantly with one mouse-click. They want their purchases delivered in a few hours or a week at the latest. As a result, producers must consider new consumer expectations when setting up the production process. Responding to buying patterns subject to rapid shifts can only be realized when production equipment is highly automated and adaptable to sudden order changes. This is what we mean by Industry 4.0. All industrialized nations are faced with this challenge. Market shifts are occurring so fast that only those manufacturers who are sensitive to these shifts will come out ahead. I think Korea has figured this out and is making the effort to secure future competitiveness in rapidly changing markets.

The key topic to be discussed in the forum is collaborative innovation. During the 20th century, "cities" of science and technology played an important role in developing knowledge-based industries. Do you think these S&T centers will continue to play a leading role? How important will regional innovation, information and expertise be in the future?

Innovation is the key to success in the long term. All nations are building innovation centers. Daejeon is a good case in point. However, as we look back at development over the past decades, successful innovation is attributable to multidisciplinary collaboration. For example, in the case of cars, change started as mechanical innovation. Later, electronics greatly influenced the industry. Recently, software emerged as the primary source of innovation. In the future, automotive features will totally change with the adoption of autonomous vehicles and electrical operation. The same pattern can be seen in 3D printing technology which is already evolving as the result of new software development.

- Based on an interview first published in HelloDD, September 7, 2017

KIST News

KIST's Jeonbuk campus leads the nation in composite material research
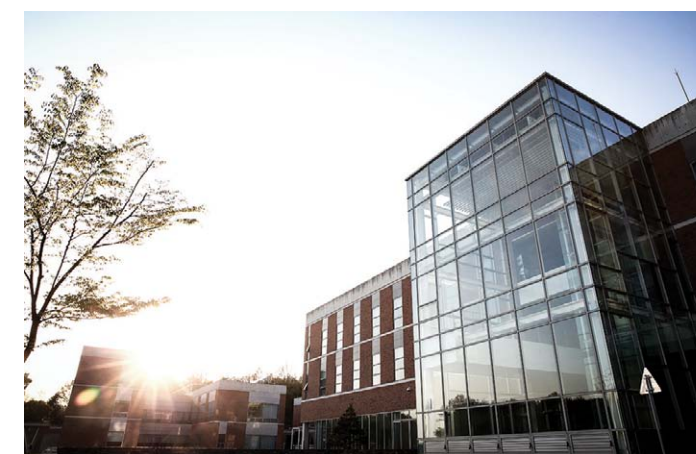
Since its establishment in 2008, the Composite Material Research Center of KIST, located in Jeonbuk, has been taking a leading role in the field of composite materials in Korea. KIST-Jeonbuk has equipment and facilities worth 70 billion won and makes 90% of these resources available to guest users. It is
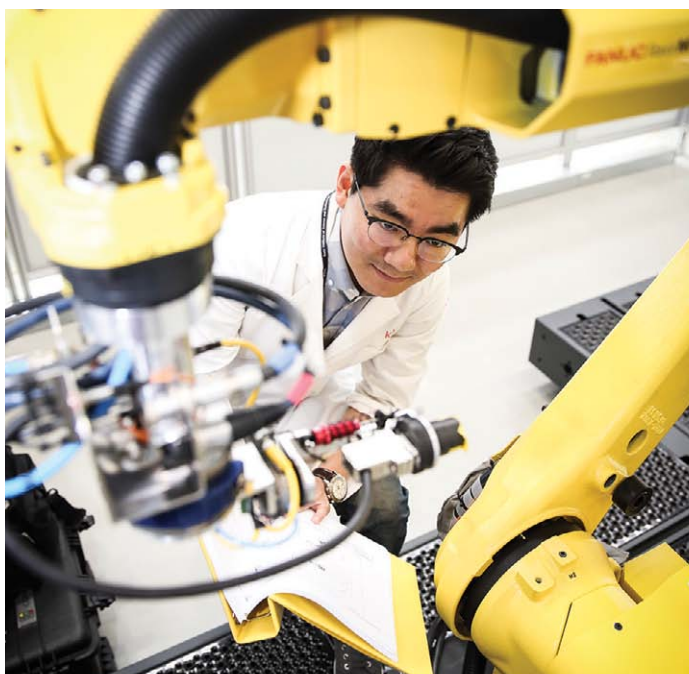
Analytical Capability	Equipment Available for Joint Use
structure-image analysis	SEM, TEM, FIB, etc.
surface characteristics analysis	AFM, STM, etc.
durability-fatigue test	biaxial tensile tester
precision machining analysis	large-area graphene synthesizer, etc.
cell-chemical and spectrum characteristics analysis	Raman, XPS, etc.
thermal dynamics-fluid mechanics analysis	TGA, etc.
composite material (moulding/processing, designing/analysis) equipment	RoboMAG-T standard system etc.

possible to conduct research on all types of materials with the equipment found at the center. It provides a kind of "one-stop service" in the analysis and evaluation of materials, starting at the raw material stage, through intermediate development stages, and on to the production of finished goods. It has partnered with 80 companies as part of an effort to support national science and technology goals and position Korean industry for the future.

Its work is enhanced by having cutting-edge research equipment that allows a full range of research from analysis to the final production of parts. This equipment includes machines for the analysis of structure and chemical characteristics as well as processing equipment for producing and forming composite material compounds. 60 kinds of analysis equipment are housed in a specially-designed vibration-proof lab. The lab is home to an electron microscope for viewing atomic structure and a transmission electron microscope that can analyze the internal structure of material in 3D on a nanometer scale (1nm is $1/10^9$ meter). One of the more interesting pieces of equipment is a hybrid integrated analyzer, the only one of its kind in the world, developed by KIST-Jeonbuk researchers. It can analyze material samples down to the atomic level by running various analyses simultaneously, such as raman scattering, atomic force microscopy, cathodoluminescence, etc., by using a scanning electron microscopy chamber with multiple ports.

Specialized equipment is consolidated according to function in three separate rooms, one for large equipment, the second for processing equipment and a third for equipment to test nano and carbon materials destined for commercialization. An example of the later type is a 2D·3D automatic laminating machine that can make a robot arm or a carbon fiber car-body, such as that found in BMW models i3 and i8. This truly represents the most modern equipment available anywhere in the world.

KIST-Jeonbuk is well positioned to maintain and even expand its role at the head of high-tech industrial development in Korea and will continue to use its cutting-edge equipment for this purpose.

Senior research engineer at KIST is put in charge of national effort to curb fine dust pollution

Gui Nam BAE, a senior research engineer at KIST, was recently appointed as the director of the national project to curb fine dust pollution, a growing environmental problem for Korea and elsewhere in the world. The Ministry of Science and ICT announced several appointments in May of this year related to national strategic projects. These included the naming of directors for artifical intelligence, fine dust pollution and carbon upcycling, issues associated with future economic growth and its social and environmental impact.

Dr. BAE and his group will work to identify the causes of fine dust in the atmosphere, provide precise measurement and forecasting, develop effective collection methods and, ultimately, recommend measures for the reduction of this pollutant. Based on a careful evaluation of fine dust's influence on health, a comprehensive solution is sought that will protect the Korean people. According to Dr. BAE, "Although various impacts from fine dust on human health have been identified, answers for why such highly concentrated fine dust occurs remain unsubstantiated, thereby raising considerable concern." He added, "Based on scientific and carefully researched cause analysis, the fine dust project group will commit itself to the well-being of the Korean people by developing field-ready technology to measure, control and protect from fine dust."

Culture-based traditional technologies to be a new research focus at KIST

KIST recently launched the Traditional Culture Convergent Research Project whose mission is to investigate ways in which modern technologies can be used to help traditional industries create a vigorous and viable market sector. Dr. Ho Gyu HAN will lead the new group. At the launching ceremony, the project group presented their vision for the project and introduced three R&D tasks. KIST has also organized the

Traditional Renaissance Support Group, directed by Dr. Gyoung Tae HONG, to facilitate and support the commercialization of traditional goods. This group will help businesses which produce products associated with traditional Korean culture use modern methods in a way that maintains self-reliance but ensures a profitable market for their goods.

As described by one of the project's researchers, "The project will examine ways to expand the existing market for products of traditional culture such as foods, living tools, architecture and materials by increasing consumer awareness. We will also examine strategies for creating new markets." The project group will identify appropriate topics for R&D, help businesses troubleshoot issues that arise, develop training and personnel management strategies and provide support for selling and advertising products. Support group director Dr. HONG said, "The project will highlight the strengths of traditional culture, elevate the industrial value of traditional culture resources through converging it with modern science and technology, and lay the groundwork for collaboration through a network of industrial, academic· and administrative participants in order to encourage innovation in traditional materials and processes."

KIST to support Vietnam's scientific heart beat

Construction is in full swing at an industrial complex 30 kilometers northwest of Hanoi, the capital of Vietnam. There is activity everywhere, from the entrance where cars constantly come and go to the site itself, where people and equipment are busy tamping down the land prior to pouring the foundations for future buildings. Signs marking the designated lots for buildings have been erected in many places. Along the main road within the complex, a few buildings of unique design are already standing. This is what Hoa Lac Hi-Tech Park currently looks like, the site for developing Vietnam's future economy.

Hoa Lac Hi-Tech Park is being built as the future science capital of Vietnam. On land of 917,355 m² (3 million pyong), labs for applied research and university-based facilities will be built. The Vietnamese government is moving ahead with the park and encouraging participation by highly respected universities and research centers around the world. Corporations involved in applied research are also being invited to locate at the site.

The Vietnamese government has asked KIST to serve as a model center for applied research. KIST was selected because its history and operations mirror what is sought in Vietnam: economic growth and security based on science and technology.

The Korean and Vietnamese governments signed an MOU for cooperation related to the foundation of VKIST in October 2012. The VKIST project is intended to share KIST's experience in operating and developing a research center built with the help of foreign aid, as was the case in the 1960s when the U.S. supported KIST's establishment and early development. Among Official Development Assistance projects undertaken by the Korean government, VKIST represents the largest in scale for a single project.

At the center of it all

The Vietnamese government has set aside 231,404 m² (70,000 pyong) at the center of the park for VKIST. It will be built alongside a lake which stretches through the complex. The VKIST facility will be completed at the end of 2020 after groundbreaking in April 2018. Behind the research center, plans have been finalized for the location of a French university while nearby, facilities associated with American and German universities will be built. When completed, the park will act as a cutting-edge research environment with the resources to attract exceptional personnel.

The VKIST project is being promoted mainly by KIST and KOICA (the Korea International Cooperation Agency). KOICA will invest 39.2 billion won for the project and KIST will establish the infrastructure, including research equipment and IT systems, provide expertise and training, organize joint research, make arrangements for consulting and conventions, and run overall operations.

Vietnam represents an attractive investment opportunity for advanced nations. It is a young country of 95 million where the average age is 28. Despite sluggish global markets, Vietnam is developing at the fastest rate in the world, showing its potential as a future market. For this reason, many international corporations as well as Korean companies are scrambling to break into Vietnam.

Experienced leadership at the helm

The former president of KIST, Dong Hwa KEUM, has been appointed by the Vietnamese government to be the first president of VKIST. President KEUM took office in mid-April and will serve for five years. His office and VKIST's operations are temporarily housed at the Ministry of Science and Technology in Hanoi until the permanent facilities are completed.

KIST and Vietnam are working together to develop appropriate policies and regulations for VKIST. Although Vietnam has invested on a small scale in basic research, it has not invested in applied research which the Vietnamese government now feels is necessary for industrial

development. That is why it requested help from Korea in setting up the many facets of a modern research facility. President KEUM explained that, "Vietnam has requested assistance centering on hardware before, but now it needs growth know-how and technology transfer for software. Since Korea can provide a complete range of support, unlike many other nations, Korea is seen in a favorable light. Vietnam prefers Korea over other nations, such as Japan." Looking ahead, he further suggested that, "At the outset of VKIST, we expect manpower support from KIST. After that, the institute will generate a synergistic effect with Korean corporations through establishing steady networks with them."

A project of this scope is not without difficulties. As President KEUM described it, "We are in a situation where change to the original schedule is unavoidable since the project depends on different acts, systems and administrative procedures unique to Vietnam. It will not be easy to persuade Vietnamese civil servants and scientists to adopt different systems and to promote different policies." Nonetheless, having anticipated these issues, President KEUM is taking various steps to smooth over such difficulties.

The Vietnamese government has determined that wage rates for VKIST researchers will be twice the existing wage scale for Vietnamese engineers, a policy taken in order to attract experienced researchers from overseas. According to a source at KIST, such an offer by the Vietnamese government is unprecedented and very generous, although opposition is anticipated from in-country engineers and other scientists. This policy is a clear indication of the risks the Vietnamese government is willing to take in its push to create economic growth through science and technology.

Taking steps to ensure a PyeongChang Olympics free of doping

Doping refers to using prohibited means to temporarily raise athletic performance. This can include taking certain drugs as well as blood or gene manipulation. Antidoping measures aim to guarantee fair competition by ensuring a level playing field where performance is determined on principles of good sportsmanship. The code of the World Anti-Doping Agency (WADA) and its programs are based on the following goals:

PyeongChang 2018

PyeongChang 2018 PARALYMPIC GAMES

- to protect the athletes' fundamental right to participate in doping-free sport and thus promote health, fairness and equality for athletes worldwide.

- to ensure harmonized, coordinated and effective anti-doping programs at the international and national level with regard to detection, deterrence and prevention of doping.

So far, thanks to methods developed for detecting prohibited pharmacological substances, improved education on antidoping, and heightened recognition of doping issues, the number of athletes testing positive has been gradually declining. On the other hand, while doping test technology has improved, the technology for avoiding detection has also become more sophisticated.

Several major scandals illustrate just how big the temptation is to dope and how serious the consequences can be. Everyone is familiar with the cases of global sports star Lance Armstrong, sometimes referred to as "the emperor of cycling", and Tyson Gay, a top U.S. track and field star. Both athletes saw their fortunes and reputations plummet because of drug abuse. Sports fans and sponsors were quick to withdraw their support, an experience shared by others who have also committed doping offences. In addition to these high profile cases, there have been many

other instances of doping, most notably, the scandal that grew out of the Russian government's manipulation at the Sochi Olympics.

Such scandals are serious enough to remind people of the importance of monitoring prohibited pharmacological substances, and they also provide momentum for the International Olympic Committee (IOC) and WADA to ramp up education related to antidoping and strengthen the monitoring and supervision of authorized labs. The Russian doping scandal prompted WADA to expand its role beyond that of simply monitoring antidoping measures to include investigation as well. Management of doping is becoming more rigorous and sophisticated. Measures announced at the WADA Symposium held in April 2017 in Lausanne, Switzerland, include an enhanced whistlblower system and the launch and operation of an independent investigation team in conjunction with Interpol.

Soohorang 수호랑

Bandabi 반다비
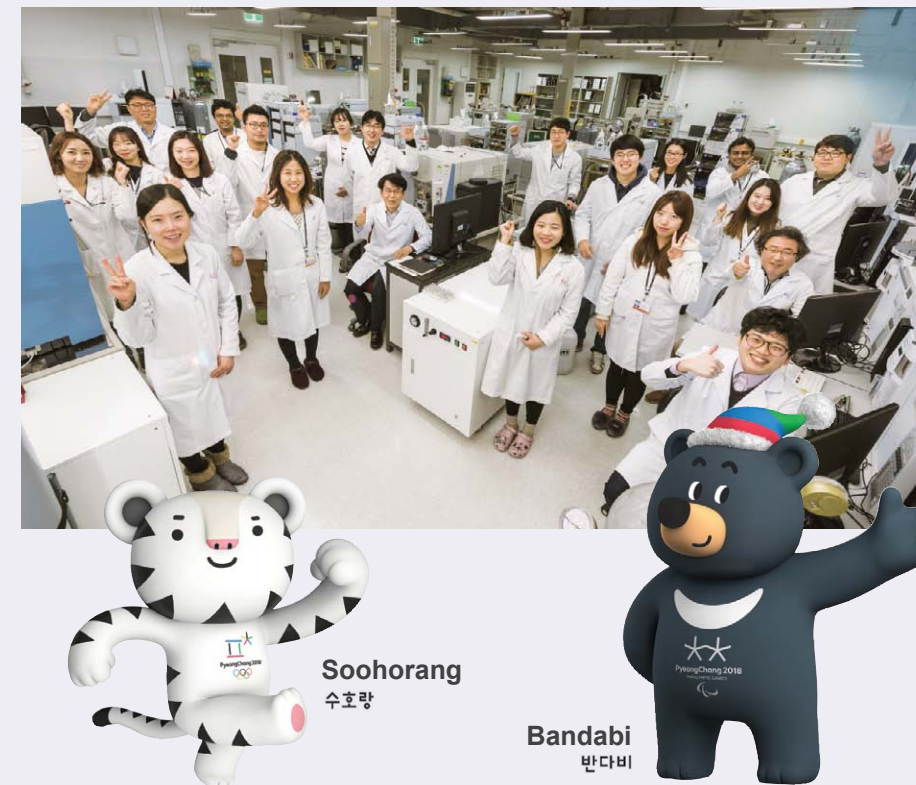
Recently, new terms expanding the scope of doping have appeared: brain doping and mechanical doping. Experiments conducted by the U.S. Ski and Snowboard Association applying targeted electrical stimulation to the brains of an experimental group and measuring their snowboard jumping performance compared to an unstimulated control group resulted in a 70~80% improvement in the experimental group's jump performance and balancing ability. Although more research is needed, it is significant that the game performance of athletes was improved with a simple system of two electrodes connected to a 9V battery. Mechanical doping emerged as an issue after cycling athletes were found to have improved their performance not by means of their muscles and aerobic fitness, but by installing a mechanical system on their bicycles in secret.

These newly identified forms of doping seem particularly shocking since they are such blatant examples of poor sportsmanship. Furthermore, as doping evolves past the exclusive realm of drug use, existing analysis methods will fall short, necessitating new tools to detect a wider range of doping infractions.

In Korea, the entity responsible for detecting doping through scientific analysis is KIST's doping control center in Hongneung. The center was founded in 1984 and by 1987 had become the 15th lab to be authorized by WADA internationally. It gained international recognition by detecting the use of Stanozolol, a steroid drug, in the urine of Canadian Ben Johnson at the Seoul Olympics in 1988. Significantly, despite a reduction in the number of authorized labs certified by WADA, down from 35 in 2016 to 27 as of April 2017, the integrity and quality of KIST's doping control center allowed it to retain its WADA certification. It is the only globally authorized center for doping control in Korea. The center moved to a new building and invested in cutting-edge systems in preparation for several major athletic competitions, including the 2014 Incheon Asian Games. Now it is preparing for the 2018 PyeongChang Winter Olympics which will require even greater manpower and more sophisticated facilities.

The 2018 PyeongChang Winter Olympics is a significant event for Korea. It is only the fifth nation to hold four of the world's most important athletic events: the summer and winter Olympics, the Worldcup football championship and the IAAF World Championships. Prior to the opening of the 2018 Olympics, the doping control center is strengthening its credentials even further by seeking additional certification on insulin and luteinizing hormone analysis and methods to analyze growth hormones. All aspects of a successful doping center, including facilities, security, analysis technology and manpower, must be synchronized to maintain WADA certification and ensure that the Olympic games are fair, safe and live up to the expectations of the Korean people and the world.

The youth of a creative scientist takes one of Korea's largest companies by surprise

Developing innovative concepts for next-generation memory chips with support from Samsung

"When I was named as a winning recipient of a research grant offered through Samsung's future technology facilitation project, I was just a postdoctoral associate at KIST. Samsung's staff repeatedly asked whether I was indeed the person who proposed the project. I had to describe myself over and over again each time they called."

The ideas of a young scientist caught the attention of a major Korean corporation, Samsung Electronics. That young engineer was Dr. Seong Hoon WOO of KIST's Center for Spintronics. Still in his twenties, Dr. Woo was chosen over more experienced scientists for Samsung's future technology facilitation project thanks to his research proposal to develop semiconductor chips that have unprecedented energy efficiency. Unable to believe that such a young person could come up with such a creative proposal, Samsung called Dr. Woo several times to confirm that he was indeed the same person who had submitted the winning proposal.

Although he has less experience than other seasoned engineers, Dr. Woo is already attracting great attention for his research into a new type of memory chip that consumes negligible power by using electron spins instead of electron charges. He has published groundbreaking work in which magnetic domain wall motion driven by spin waves was confirmed for the first time.

The ultimate goal of Dr. Woo is to develop a spin-based next-generation memory chip, which overcomes the current limitation of Si-based devices. Such technology is considered crucial for the advancement of semiconductor technology.

According to Dr. Woo, "When this project goes successful, spin-based memory devices will change the paradigm of current electronics, including laptops, smart phones, and all future devices." He added, "We will actively share findings with other experts in many relevant areas to really make commercialization possible."

Alternative military service leads to investigation of future memory chip technology

Following his doctoral work at MIT, Dr. Woo established ties with KIST through the alternative military service program. To fulfill his military obligations, he was required to work in research on a 3-year contract basis at KIST. Both at MIT and later at KIST, he worked on developing a new concept for semiconductor chips.

Early this year, joint research conducted with his academic adviser, Geoffrey Beach, an associate professor in the material science and engineering department at MIT, successfully demonstrated that memory chips can be operated with almost zero power consumption by using the spin characteristic of a device. By addressing a number of problems plaguing semiconductors in current use, this spin based technology is well positioned to become a core technology, its unique attributes including reduction of heat gain with a smaller chip size and occurrence of a new quantum effect. This discovery is particularly promising for the new high-end technologies such as AI, which consumes tremendous amounts of power and big data. This finding was published in *Nature Physics* in January of this year.

A particular focus of Dr. Woo's R&D efforts is a distinct spin structure called *domain wall*, which refers to the boundaries of magnetic areas exhibiting different magnetism. Research into domain wall structure and its application to memory chips has been conducted worldwide because this approach promises high mobility and great reliability in addition to an inexpensive production process. However, the threshold power to mobilize domain wall structure has remained unacceptably high, offering no advantage compared to existing electronic devices. Despite ongoing worldwide effort to reduce critical current value, no definitive solution has yet been identified.

In contrast to the electric current-based domain wall mobilization method, Dr. Woo approached with a different concept. In particular, he discovered that strong spin wave bursts, generated by the collision of two domain walls, could push domain walls in a magnetic device very efficiently. Using this approach, he was able to successfully operate the magnetic domain wall-based memory device at a significantly reduced power threshold.

Highlighting the importance of reduced power consumption, Dr. Woo explained, "Currently, it is very critical to efficiently cool down the semiconductor chips in electronic devices. However, our 'zero power' (ultra low power) technology will not generate such a large amount of heat."

As to the future, he suggests, "Zero power memory chips require additional R&D to develop readable and writeable devices.

The technology remains at a basic level for the moment, but new approaches using spin devices will contribute significantly to the entire industry involved in next-generation memories."

"The power to operate AlphaGo is equal to all the power required to run one research complex at KIST. However, if it were possible to operate memory chips using electron spins, not charges, power consumption could be significantly reduced by a factor of hundreds, or even thousands. I expect that such advancement could also be exploited for cutting-edge technologies such as AI and supercomputers, which are key to the so called Fourth Industrial Revolution."
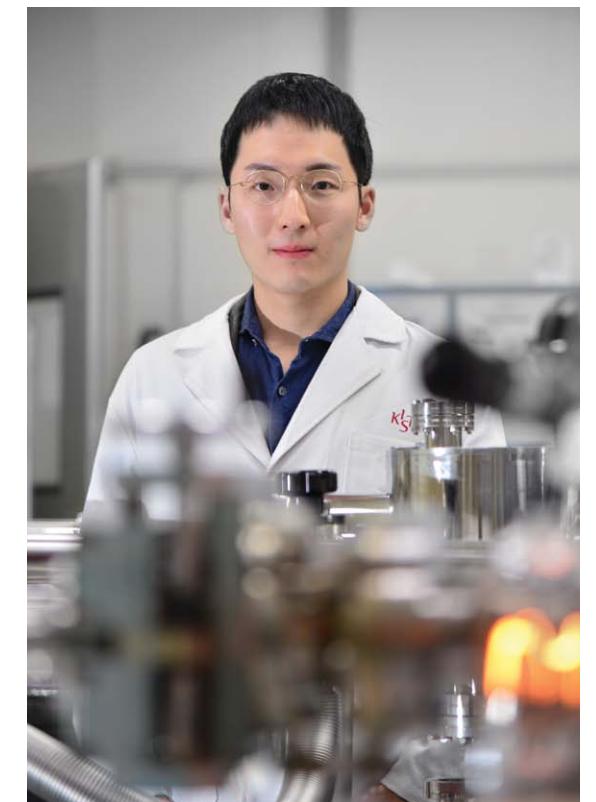
New approaches for improving electronic devices

In addition to his work with domain walls, Dr. Woo has teamed with a group at Daegu Gyeongbuk Institute of Science and Technology led by Jung Il HONG, a professor in the department of emerging materials, to develop technology for next-generation ultra-low power high frequency communication devices. This technology is based on a unique spin structure known as a skyrmion. Dr. Woo's team published their latest research in the online edition of *Nature Communications* in May of this year. Their work involved the electrical generation of magnetic skyrmions in the absence of magnetic field by using bipolar pulses. Moreover, they were able to demonstrate "skyrmion breathing" for the first time, a unique dynamic of magnetism which generates high frequency electronic signals by the repeated expansion and shrinking of the spin structure.

Dr. Woo commented on the implications of this research by saying, "The study's results show that high-efficiency next-generation telecom devices based on skyrmion, previously only a theoretical concept, can actually be realized. This work opens the way for earlier development of high-performance electric devices."

The value of team support

With many years ahead of him, Dr. Woo plans to concentrate on his research with support from both junior and senior colleagues. He considers the success of his zero power memory chip research due in large part to the passion of KIST's spintronics researchers who convinced him that the idea was worth pursuing. He is grateful for the help he received from senior researchers since he lacked experience in verifying and translating spin wave. He adds, "I was given a rare chance. Chance may only appear once in every hundred experiments. I listened to the stories and advice of senior researchers and colleagues whenever I faced failure. Thinking hard about how other scientists overcame difficulties gave me a better understanding of research. I intend to devote myself to work with the mindset of making the best possible effort every day."

Science Cartoon

Newton, do you understand me?
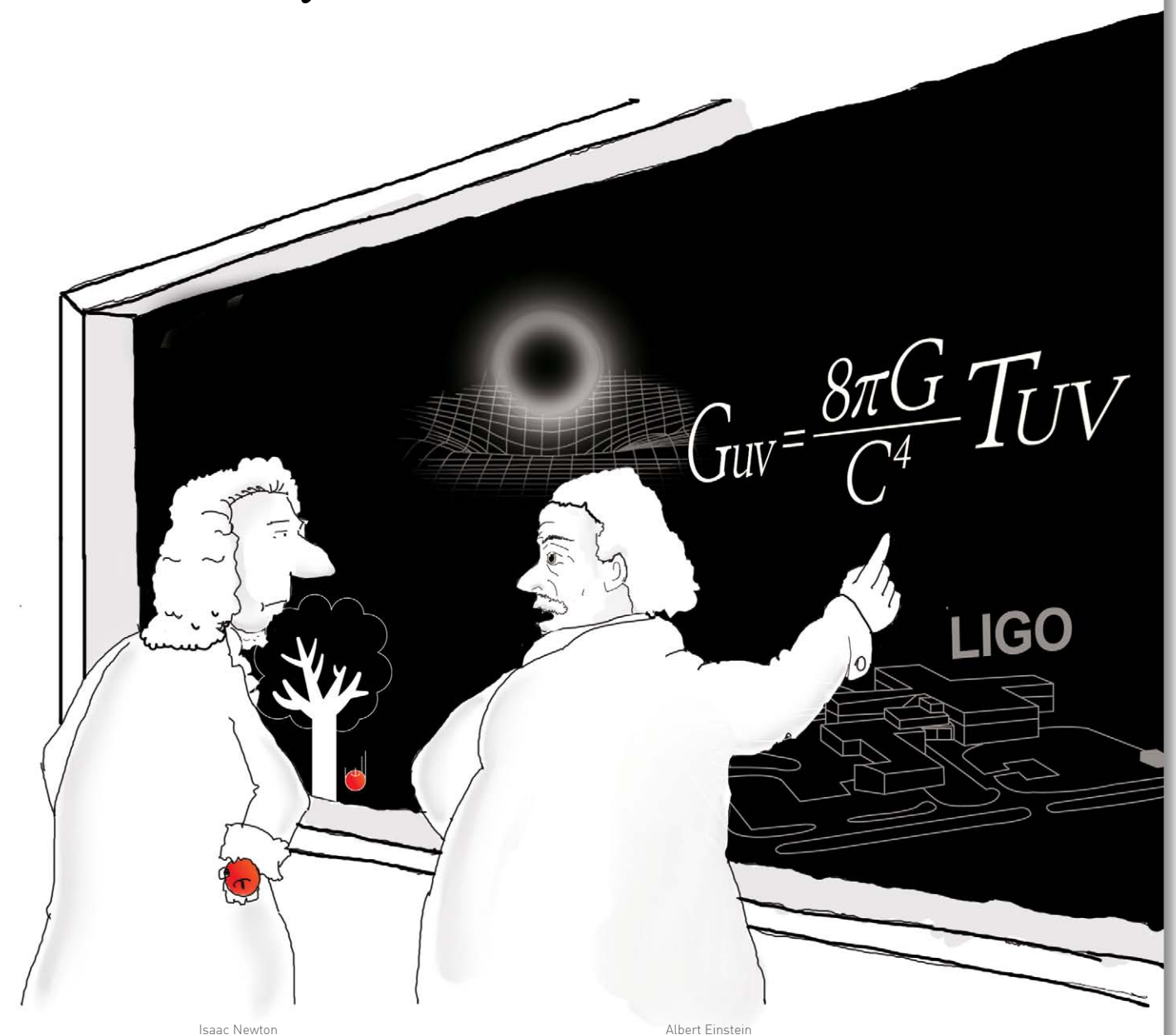
Isaac Newton Albert Einstein

$$G_{uv} = \frac{8\pi G}{C^4} T_{UV}$$

LIGO

KIST Jeonbuk Institute of Advanced Composite Materials

Leading World-Class Composite Material Technology

KIST Jeonbuk is leading the development of composite materials in Korea under the regional strategic industrial growth initiatives.
The institute researches and develops new source materials and trains professionals in the field of composite materials.

Composite materials are lightweight, elastic, wear resistant, and extremely versatile due to their unique electronic properties.
As such, they are often considered a crowning technology for the 21st century.

KIST Jeonbuk is pushing ahead to develop innovative, dynamic composite materials, including carbon composites, and to position itself as an R&D hub for advanced industries.

Focus areas of development

- Carbon fiber
- Novel functional materials
- Manufacturing process technology for structuring composite material

KIST
Korea Institute of
Science and Technology